

Aus dem Bereich Theoretische Medizin
und Biowissenschaften der Medizinischen Fakultät
der Universität des Saarlandes, Homburg/Saar

**Simultaneous capacitance and TIRF measurements from lytic granule fusion in
primary human cytotoxic T lymphocytes**

Dissertation
zur Erlangung des Grades
eines Doktors der Naturwissenschaften
der Medizinischen Fakultät
der Universität des Saarlandes
2013

vorgelegt von
Min Ming
aus Wuhan

Homburg 2013

Acknowledgements

My deepest gratitude goes first and foremost to Prof. Dr. Jens Rettig, my supervisor, for his constant support and enlightening guidance. Without his valuable advice, impressive patience and understanding, I could not have completed my thesis. I would like to particularly mention how much I admire him. I am delighted that I got such a wonderful PhD supervisor who not only taught me about science but also served as a role model in life and career.

I would also like to express my appreciation to Dr. David Stevens for his generous help with my two projects and thesis through all the stages of my PhD work.

I would like to sincerely thank Prof. Dieter Bruns for valuable suggestions and support for my first project. I also acknowledge the help of Antonio Yarzagaray provided chromaffin cells from synaptobrevin knock-out mice.

I am also greatly indebted to Dr. Ute Becherer, who taught me the imaging experiments and analysis with great patience and helped me throughout my work. My deep gratitude also goes to Dr. Elmar Krause for his generous help.

I would like to express my deep appreciation to Dr. Ulf Matti, Dr. Claudia Schirra, Dr. Mathias Pasche who have kindly helped and guided me especially in the beginning. I would like to thank Dr. Detlef Hof for his excellent technical support and patient discussion for optimizing the program for TIRM data analysis.

In these three years, I not only received scientific training but also evolved and was influenced by a group of nice people. I would like to give my genuine and heartfelt thanks to: Dr. Monika Maier-Peuschel, Sandra Hugo, Anneka Bost, Niklas Schütter, Nguyen Truong Cuc Quynh, Mahantappa Halimani, Dr. Varsha Pattu, Dr. Misty Marshall, Monica Dudenhöfer-Pfeifer and Silke, Dr. Ulrike Hahn.

I am also grateful to Prof. Dr. Markus Hoth and Carmen Hässig for their generosity in providing human peripheral blood lymphocytes.

I would like to thank Katrin Sandmeier, Manuela Schneider, Anja Ludes, Anne Weinland, Margarete Klose, Nathalie Höfs, Carolin Bick and Reiko Trautmann, for excellent technical support.

I would like to thank Bernadette Schwarz who was so kind and patient in helping me solve many problems in my life from beginning till the end of my Ph.D. study and make my life in Germany much easier.

I also owe my deep and sincere gratitude to my friends Dr. Bin Qu, Ting-Jiun Chen, Carsten Kummerow, who provided me great help, support, consistent

encouragement and understanding especially during my difficult times. I would like to show my appreciation to all the people who helped or tried to help me!
Thanks also to Dr. Manfred Lindau for his helpful suggestions!
Last my thanks would go to my beloved family for their long-lasting love.

LIST OF CONTENTS

LIST OF CONTENTS	1
Zusammenfassung	3
Abstract	5
Abbreviations	7
1. Introduction	10
1.1 Chromaffin cells	10
1.2 Exocytosis	10
1.3 Vesicle pools in chromaffin cells	11
1.4 Docking in electron microscopy	12
1.5 Fusion and electrophysiology	12
1.6 Priming and TIRF microscopy	14
1.7 Proteins involved in exocytosis	15
1.7.1 SNAREs: The “Zippering” model and the binding partners	16
1.7.2 Ca ²⁺ and depolarization	22
1.7.3 Transmembrane domain of Syb2	23
1.8 Goal of the project	25
2. Materials and Methods	26
2.1 Materials	26
2.1.1 Reagents	26
2.1.2 Enzymes	27
2.1.3 Solutions	27
2.1.3.1 Solutions for mouse chromaffin cell preparation	27
2.1.3.2 Solutions for virus activation	28
2.1.3.3 Solutions for measurements	28
2.2 Methods	30
2.2.1 DNA constructs and semiliki forest virus	30
2.2.2 Knockout mice and mouse chromaffin cell culture	32
2.2.3 Setup and protocols	33
2.2.4 Time window and analysis for TIRF Microscopy	35
2.2.4.1 Time window for TIRF	35
2.2.4.2 Single granule trajectory analysis	36
3. Results and discussion	39
3.1 Results	39

3.2 Discussion.....	44
4. Introduction.....	48
4.1 Lytic granules in Lymphocytes.....	48
4.2 CD8+ T-cells	48
4.3 T-Cell mediated killing.....	50
4.4 Ca ²⁺ and CRAC channels.....	51
4.5 The aim of my work.....	53
5. Materials and Methods.....	55
5.1 Materials.....	55
5.1.1 Reagents	55
5.1.2 Solution.....	56
5.1.3 Human GranzymeB-mCherry cDNA construct	57
5.1.4 Isolation human CD8+ from PBL	57
5.1.5 Eletroporate bead-stimulated human CD8+ cells.	58
5.2 Methods	60
5.2.1 TIRF images.....	60
5.2.2 Membrane Capacitance Recordings.....	60
5.2.3 The description of the combination experiments	60
5.2.4 Capacitance increment analysis	61
5.2.5 Single lytic granule trajectory analysis	64
5.2.6 Mean squared displacement detection by TIRF setup	65
6. Results and discussion	69
6.1 Results	69
6.2 Discussion.....	78
Reference	81
Curriculum Vitae	91

Zusammenfassung

Kultivierte Chromaffinzellen werden häufig als Model zur Untersuchung der Exozytose einzelner Vesikel genutzt. Grosse elektronendichte Vesikel (large dense core vesicles; LDCVs) lagern sich erst transient an die Zytoplasmamembran an (Docking) und werden dann auf die Membranfusion vorbereitet (Priming). Die Exozytose der LDCVs ist Ca^{2+} -abhängig und wird durch den sogenannten SNARE-Komplex (soluble N-ethylmaleimide-sensitive-factor attachment receptor) eingeleitet. Er besteht aus SNAP-25, Syntaxin und Synaptobrevin 2 (Syb2) und katalysiert die Fusion von Vesikeln an der Plasmamembran. Obwohl sich bereits viele Studien auf die Rolle der SNAREs und deren Interaktionspartner fokussieren, ist die Rolle der Transmembran-domäne (TMD) von syb2 während der Exozytose immer noch unklar. Aus diesem Grund ist das Ziel des ersten Teils dieser Arbeit die funktionelle Rolle der TMD von Syb2 während der Ca^{2+} -abhängigen Exozytose in murinen Chromaffinzellen zu untersuchen. Hierzu wurden Chromaffinzellen von Syb2/Cellubrevin Doppel-Knockout-Mäusen verwandt, da diese einen geeigneten genetischen Nullhintergrund aufwiesen. In diesen wurden dann Syb2 Varianten mit verschiedenen Mutationen in der TMD Region exprimiert. Um die Vesikelmobilität kurz vor der Membranfusion in bovinen Chromaffinzellen untersuchen zu können hat sich die Kombination aus der Internen Totalreflexionsfluoreszenzmikroskopie (total internal reflection fluorescence microscopy, TIRFM) und dem Semliki-Forest-Virus (SFV) Expressionssystem bewährt. In dieser Arbeit wurde die Methode erstmalig an murinen Chromaffinzellen etabliert. Dadurch konnte gezeigt werden, dass die Deletion von Syb2 in Knockout-Mäusen das Docking der Vesikel in isolierten Chromaffinzellen nicht beeinflusst. Die Rolle von Syb2 beim Priming der Vesikel in der Ca^{2+} -abhängigen Exozytose wurde durch Patch-Clamp-Messungen in der Whole-Cell-Konfiguration untersucht. Über die Patch-Pipette wurden Intrazellulärlösungen mit verschiedenen Ca^{2+} -Konzentrationen appliziert, um den Priming-Prozess zu induzieren und dann durch Depolarisation die Sekretion der Vesikel auszulösen. Die Ergebnisse von Syb2/Cellubrevin Knockout-Experimenten und Cellubrevin Knockout-Experimenten unterschieden sich jedoch nicht signifikant bei den verwendeten Ca^{2+} -Konzentrationen. Die Analyse der Experimente mit Virus-infizierten Zellen zeigte jeweils eine Entleerung des primed pools durch spontane Ausschüttung, was in unbehandelten Zellen aber nicht zu beobachten war. Diese Entleerung ist

höchstwahrscheinlich auf cytotoxische Effekte des durch die Virus-Infektion exprimierten Fluoreszenzprotein-gekoppeltem Neuropeptids Y zurückzuführen.

Im zweiten Teil dieser Arbeit wurde die Größe von lytischen Granulen in humanen cytotoxischen T-Lymphocyten (CTLs) bestimmt.

CTLs zerstören mittels Exozytose zytotoxischer Substanzen Antigen präsentierende Zellen (APCs), welche von Viren infizierte Zellen oder Tumor-zellen sein können. Die Ausschüttung toxischer Substanzen erfolgt über die Fusion lytischer Granulen an der für die Interaktion von T-Lymphocyten und APCs spezialisierten Immunologischen Synapse (IS), die eine enge Verbindung zur Zielzelle darstellt. In dieser Arbeit wurden CTLs zur Ausbildung einer artifiziellen IS an Deckgläsern angeregt. Zur Visualisierung lytischer Granulen wurden die CTLs mit fluoreszierendem Granzyme B-mCherry Fusionsprotein transfiziert. Durch die Kombination von TIRF Mikroskopie und Membran-kapazitätsmessungen mittels der Patch-Clamp Technik konnten so erstmalig Kapazitätssprünge identifiziert werden, die auf die Sekretion einzelner lytischer Granulen zurückzuführen sind. Die Anpassung einer Gaußfunktion an die Häufigkeitsverteilung ergab diskrete Maxima bei 2.23 fF, 3.94 fF und 8.17 fF, was auf die Existenz von bis zu drei unterschiedlichen Populationen lytischer Granula schließen lässt. Mittels Applikation von 2 μM intrazellulärem freiem Ca^{2+} durch die Patch-Pipette wurde die Exozytose von GranzymeB-mCherry markierten Granulen ausgelöst. Es wurde auch die Exozytose anderer Organellen gemessen, ihre Größenverteilung und die Latenzzeit der Fusion entsprachen jedoch denen lytischer Granulen.

Die Analyse der Bewegung lytischer Granulen ergab keinen signifikanten Unterschied zwischen den Geschwindigkeiten fusionskompetenter und nicht kompetenter Granulen. In den letzten 5 Sekunden ihrer Bewegung wiesen aber insbesondere kompetente Granulen eine Lokalisierung an der IS in einem zitternden Zustand auf.

Abstract

Chromaffin cells have been widely used as a model for single-vesicle exocytosis in culture. Large dense core vesicles (LDCVs) in chromaffin cells dock and prime at their target membranes in preparation for fusion. Exocytosis in LDCVs is Ca^{2+} -dependent and is driven by the Soluble NSF Attachment Protein Receptor (SNARE) complex. SNARE complexes consist of SNAP-25, syntaxin and synaptobrevin 2 (syb2). Intensive studies have focussed on the role of SNAREs and their interaction partners. In spite of this attention, the role of the transmembrane domain (TMD) of syb2 during exocytosis remains unclear. The goal of my first project was to study the function of the TMD of syb2 in Ca^{2+} -dependent exocytosis in mouse chromaffin cells. We have used syb2/ cellubrevin double knockout mice as a genetic null background, and expressed syb2 mutants carrying specific mutations in the TMD into this genetic null background to study how the TMD of syb2 functions during exocytosis. Total internal reflection fluorescence (TIRF) microscopy together with Semliki Forest virus (SFV) mediated protein expression in bovine chromaffin cells has proved to be an effective tool to observe vesicle mobility prior to fusion. I have established the method of TIRF in mouse chromaffin cells rather than bovine cells to take advantage of syb2/ cellubrevin knockout mouse models to study whether the TMD controls steps prior to fusion in mouse chromaffin cells. I found that deletion of syb2 does not change docking in mouse chromaffin cells. To test whether syb2 affects priming in Ca^{2+} -evoked secretion, we patch-clamped mouse chromaffin cells and applied known concentrations of intracellular Ca^{2+} solution via the patch pipette to drive the priming process, and then depolarized the cells to induce release. However, the responses from control experiments and syb2/ cellubrevin knockout experiments were not significantly different at the different Ca^{2+} concentrations applied. I found that the primed pool was depleted by spontaneous release in virus treated cells but not in cells free from virus infection. Depletion was likely caused by toxic effects of the fluorescently tagged neuropeptide Y- protein on the mouse chromaffin cells.

In a second project I characterized lytic granule size in human cytotoxic T lymphocytes (CTLs). CTLs kill antigen-presenting cells (APCs), which may be a virus infected cell or a tumor cell) via the exocytosis of toxic substances from lytic granules. Release of toxic substances occurs at a specialized junction between the CTL and an APC. This junction has been named the immunological synapse (IS) and consists of

an area specialized for lytic granules release in close proximity to target cells, to which lytic granules are transported and exocytose. We used an artificial system in which CTLs are induced to form an IS on a glass coverslip. A new method was established to detect human Granzyme B-mCherry labeled lytic granules using TIRF microscopy and simultaneously measure membrane capacitance. In this way, we could identify capacitance jumps associated with the secretion of single identified lytic granules. Gaussian fits of histograms of the magnitude of the capacitance jumps associated with granule release, indicate three peaks with populations at 2.2334 fF, 3.9398 fF and 8.1697 fF, indicating lytic granules are not monotonic but rather occur in two or three different populations. Application of 2 μM intracellular free Ca^{2+} via the patch-pipette was used to trigger granzyme-B-mCherry granule exocytosis. Lytic granules were not the only exocytotic organelles present in activated CTLs. Other organelles are also secreted, but the distribution of sizes was similar as were the latency to fusion. For the entire movements, the velocity of fusion competent granules and granules lack of competence was almost identical, and in the last five seconds fusion competent granules preferentially localized at the IS with jittering state and turn primed in short time.

Abbreviations

a.k.a also known as

ATP Adenosine-5'-triphosphate

APCs antigen-presenting cells

BSA albumin, from Bovine serum

$[Ca^{2+}]_i$ Intracellular calcium concentration

Ca^{2+} Calcium

$CaCl_2$ Calcium chloride

CD caging diameter

CD2AP CD2-associated protein

C_m Membrane capacitance

CO_2 Carbon dioxide

CRAC Ca^{2+} release-activated Ca^{2+} channel

CsOH Caesium hydroxide

cSMAC Central superamolecular activation clusters

CTL cytotoxic T lymphocytes (a.k.a $CD8^+$)

DAG diacylglycerol

DNA Deoxyribonucleotide

DKO double knock-out

DP depot pool

DPBS Dulbecco's Phosphate Buffer Saline 1X

e.g for example

EGTA Ethylene bis-(oxyethylenenitrilo)-tetraacetic acid

ER the endoplasmic reticulum ()

FCS Fetal calf serum

fF Femtofarad

g Gram

GTP Guanosine-5'-triphosphate

G_m membrane conductance

G_s access conductance

Fig Figure

HEPES 4-(2-hydroxyethyl)-1-piperazineethanesulfonic acid

H_2O Water

HPLC H_2O High Performance Liquid Chromatography water

IP3 inositol-1,4,5-trisphosphate
IRES Internal Ribosome Entry Site
IS immunological synapse or immune synapse)
ITS-X Insulin Transferrin Selenium Ethanolamine Solution
 KH_2PO_4 potassium dihydrogen phosphate
KCl Potassium chloride
KDa Kilo dalton
KO knock-out
LAT linker for activation of T cells
LFA-1lymphocyte function-associated antigen-1
LDCV Large dense core vesicles
mg milligrams
Mg Magnesium
 MgCl_2 Magnesium chloride
MHC major histocompatibility complex
Mi Million
min minute
ml milliliter
mOsm milliosmole
mRFP monomeric red fluorescent protein
ms millisecond
MSD mean squared displacement
MTOC microtubule-organizing center
Na Sodium
NaCl Sodium chloride
 NaHCO_3 sodium hydrogen carbonate
 Na_2HPO_4 Disodium hydrogen phosphate
nM nanomolar
no. number
NP-EGTA Nitrophenyl EGTA
NPY Neuropeptide Y
pF picofarad
PBL Peripheral blood lymphocytes
pH Potential hydrogen

PLC γ phospholipase γ
PO Poly-L-ornithine
pSMAC peripheral SMAC
R $_m$ membrane resistance
ROI region of interest
RRP readily releasable pool
RT Room Temperature
s second
SEM Standard Error of Mean
SFV Semliki Forest Virus
SLP76 Src homology 2 domain-containing leukocyte phosphoprotein of 76 kDa
SNAP-25 Synaptosome Associated Protein of 25 kD
SNARE Soluble NSF Attachment Protein Receptor
SRP slowly releaseable pool
SV small clear-core vesicles
Syb2 Synaptobrevin2 (a.k.a VAMP2)
Syt Synaptotagmin
TCR T-cell receptor
TFP teal fluorescent protein
TIRF Total internal reflection fluorescence
TMD transmembrane domain
ul microlitre
uM micromolar
UPP unprimed pool
UV ultraviolet
VAMP Vesicle Associated Membrane Protein
WT Wildtype
ZAP-70 ζ -chain-associated protein of 70 kDa
 ΔC_m capacitance increment

1. Introduction

1.1 Chromaffin cells

Chromaffin cells have been widely used as a model for studying exocytosis. Chromaffin cells come from the adrenal glands which sit at the top of the kidneys in mammals. Adrenal glands are endocrine glands and consist of the outer adrenal cortex and inner core, the medulla. Though both structures are devoted to hormone release, the cells of the cortex produce the steroid hormones cortisol, androgens, and aldosterone while the adrenal medulla produces and releases adrenalin and noradrenalin, which are involved in responses to stress. A significant advantage of chromaffin cells as a model for exocytosis is that they can be readily harvested from mouse adrenal glands, allowing use of gene manipulation and knockout strategies. They are also small, electrically compact cells which are very well suited for electrophysiological measurement of exocytosis.

1.2 Exocytosis

Exocytosis is the process by which membrane bound organelles merge with the cell membrane, allowing delivery of lipid and proteins to the cell membrane or release of membrane impermeant products into the extracellular space. Two pathways are present in exocytosis: a constitutive pathway and a regulated pathway, which is triggered by various events and is usually associated with an increase in intracellular calcium. Constitutive exocytosis (Palade 1975) is essential for maintaining homeostasis by supplying cell nutrients and supplying newly synthesized lipid and membrane-bound proteins to the cell membrane.

Regulated exocytosis (Palade 1975) is readily observed in nervous and endocrine tissue as well as in blood cells. Neural and neuroendocrine cells possess two distinct types of secretory vesicles that undergo Ca^{2+} -dependent exocytosis: large dense-core vesicles (LDCV) and small clear-core vesicles (SV) (Kasai 1999). These vesicles differ in size and in their appearance in electron-micrographs, with the larger LDCVs having a proteinaceous electron dense core rendering them dark (Hammarlund, Watanabe et al. 2008).

In neurons, Ca^{2+} -dependent exocytosis is temporally and spatially exquisitely controlled. In the mammalian brain, postsynaptic responses commence as little as 150 μs after the start of the presynaptic action potential (Sabatini and Regehr 1996).

This high speed is possible due to a highly organized active zone, where synaptic vesicles go through docking, priming and finally fusion with the plasma membrane. In chromaffin cells, although a number of the key molecules are the same, the Ca^{2+} -dependent exocytosis is slower (Moser and Neher 1997).

1.3 Vesicle pools in chromaffin cells

In chromaffin cells, secretory vesicles reside in one of several pools. These include a depot pool (DP), an unprimed pool (UPP), a slowly releasable pool (SRP) and a readily releasable pool (RRP) (Rettig and Neher 2002). Vesicles from the DP are docked and enter the UPP, where they undergo priming to enter the releasable pool. After priming, vesicles are fusion competent and will be released when the intracellular calcium increases after a stimulus (Fig. 1.1). Typically, the increase in calcium is the result of depolarization of the chromaffin cell which results from the action of acetylcholine on nicotinic receptors on the chromaffin cell surface. This depolarization activates calcium channels and calcium flows into the cell. Calcium can be experimentally elevated using photolysis of caged Ca^{2+} (calcium bound to a photolabile calcium chelator) by applying ultraviolet (UV) light. As a consequence, unbound $[\text{Ca}^{2+}]$ increases rapidly from the low nanomolar range to around 20 μM very rapidly. For this purpose, chromaffin cells are perfused with the calcium chelator

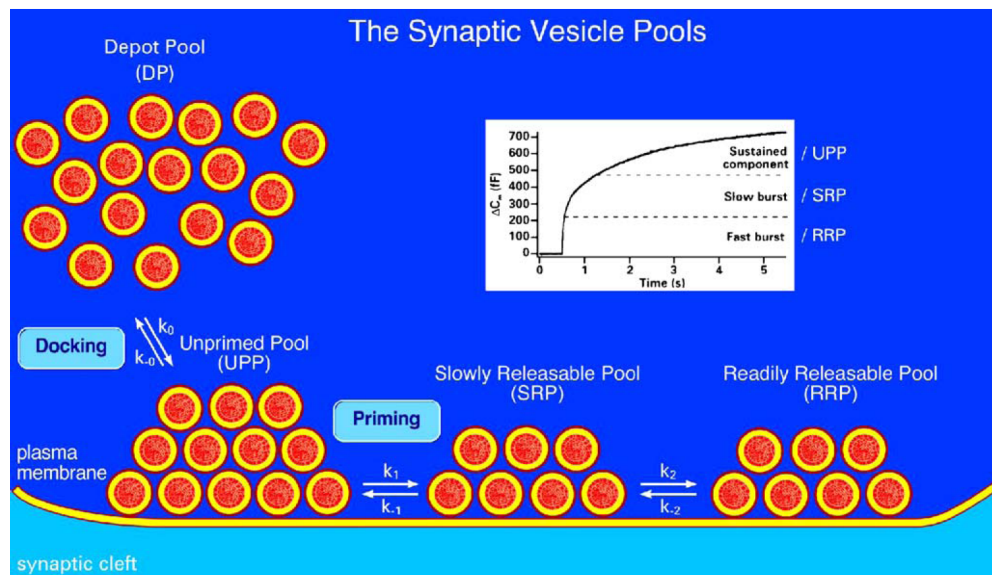


Fig. 1.1 Synaptic vesicle pools. Secretory vesicles reside in four pools: DP, UPP, SRP, RRP which can be distinguished by their release kinetics and their spatial distribution. A typical membrane capacitance response upon flash experiment from chromaffin cell was shown as inset graph. It reveals three phases: a fast burst, a slow burst and a sustained component, which correspond to the RRP, SRP and UPP, respectively (Becherer and Rettig 2006).

through the patch-pipette in a whole cell recording configuration. For chromaffin cells, one common calcium chelator is nitrophenyl EGTA (NP-EGTA) which dramatically decreases (12,500-fold) its affinity for Ca^{2+} upon UV illumination. Flash photolysis of NP-EGTA raises the intracellular Ca^{2+} homogeneously to known levels and when combined with capacitance measurement (Voets, Neher et al. 1999) reveals three phases of secretion: a fast burst (the RRP), a slow burst (the SRP) and a sustained component (shown in inset Fig.1.1).

1.4 Docking in electron microscopy

In electron micrographs, a vesicle is considered morphologically docked when it is adjacent to the plasma membrane (Fig1.2). Some authors have defined docked vesicles as those within limited distance (e.g. a vesicle radius) to the plasma membrane while others use the more stringent requirement that the vesicle must contact the plasma membrane.

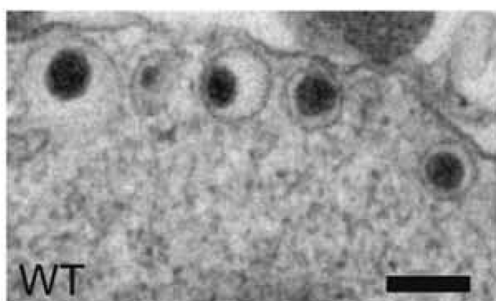


Fig1.2 The distribution of LDCVs in wild-type chromaffin cell. Electron micrographs shows morphological docking LDCVs in wild-type chromaffin cell. Scale bars, 200 nm (Liu, Schirra et al. 2008).

1.5 Fusion and electrophysiology

The micrograph in Fig.1.3 shows three synaptic vesicles which have fused with cell membrane (arrows) form so-called omega bodies. Fusion adds the vesicle membrane to the cell surface and thus increases the membrane area. Since capacitance is proportional to membrane area, fusion increases the surface area of



Fig.1.3 Micrographs of synaptic vesicles fused with cell membrane in frog nerve-muscle cross-section. Vesicles in the act of fusing with the membrane result in forms prior to being integrated into the membrane. (Torri-Tarelli, Grohovaz et al. 1985)

the cell, increasing its capacitance. For this reason, electrophysiological measurement of cell capacity allows us to monitor exocytosis.

Whole Cell Recording in Patch Clamp

There are four electrophysiological recording configurations, which are depicted in Fig.1.4: cell-attached, whole-cell recording, outside-out patch, and inside-out patch. For my measurements, I used whole-cell mode (shown in Fig.1.4) with the cell voltage clamped to -70 mV. A clean pipette with a slight positive pressure (around 20cm H₂O) is pressed against a mouse chromaffin cell. When the pressure is released, the

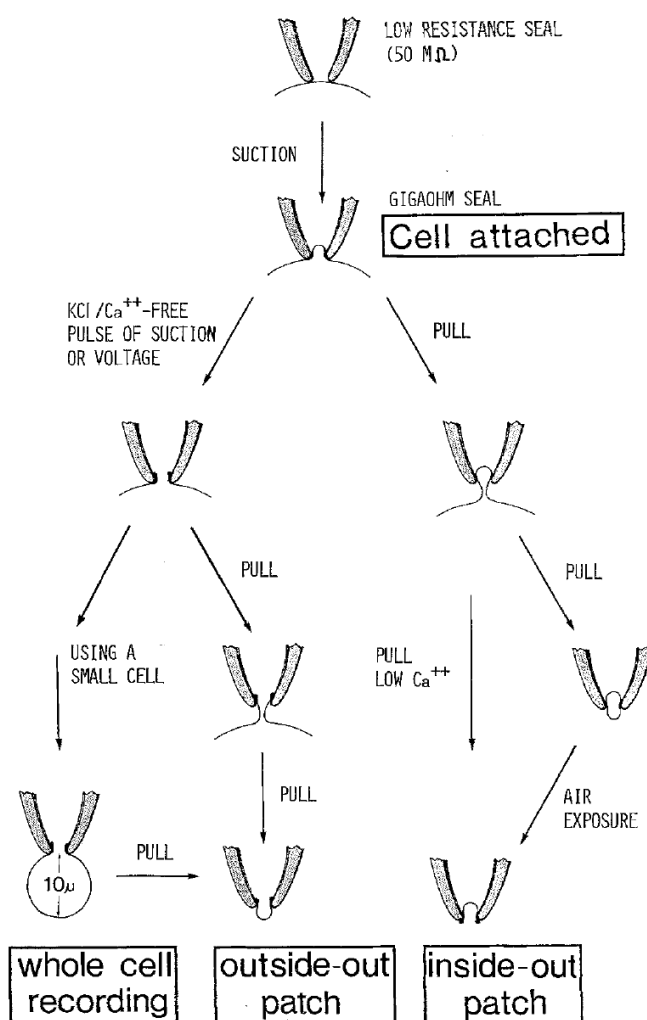


Fig.1.4 Four recording configurations. A pipette contacts with a cell and forms low resistance seal between membrane and pipette. Upon slight suction the seal increases in resistance and forms cell-attached configuration. This stage is the starting point for isolating whole cell recording or two membrane patches: the outside-out and inside-out. The manipulations include withdrawal of the pipette from the cell (pull), the pipette tip exposure to air and short pulses of suction or voltage applied to the pipette interior while cell-attached (Hamill, Marty et al. 1981)

pipette resistance increases indicating that the cell membrane partially occludes the pipette tip. Upon slight negative pressure, the membrane is drawn to the pipette tip facilitating formation of a very high resistance between the pipette and the cell

membrane which may exceed 1000 megohms, the “gigaohm” seal. After formation of a gigaseal the contact between cell membrane and glass pipette is not only electrically tight but also mechanically stable. Applying short and gentle suction can disrupt membrane occluding the pipette tip without damaging the gigaseal between the pipette rim and the cell membrane, producing a low resistance contact between the pipette and the cell interior. Since there is exchange between the pipette solution and the cell interior, the pipette is filled with a solution mimicking, to some degree, the ionic environment of the cell interior. The typical intracellular solution contains the divalent cations Mg^{2+} and Ca^{2+} , calcium buffer, monovalent cation Na^+ , anion Cl^- , small amount of ATP and GTP. The pH of the solution should be in the physiological range of 7.2-7.4, osmolality is maintained near 300 mOsm to prevent swelling or shrinkage.

1.6 Priming and TIRF microscopy

Membrane capacitance measurements after stepwise increases in intracellular free calcium have been used to estimate the amount of fusion of releasable pools with high time resolution, and changes in these pools allow inferences concerning priming. Electron microscopy yields docking information consisting of a description of the accumulation and distribution of vesicles at the plasma membrane. However, micrographs are static and do not provide information about kinetics of docking. TIRF microscopy has the potential to describe the docking process since it can selectively visualize vesicles labeled by fluorescent cargo or load with small fluorescent molecules and observe their movement at the plasma membrane in real time. Thus, TIRF microscopy is an ideal tool to track single granules and gather dynamic information about the behavior of vesicles in the cell.

The principle of TIRF microscopy is shown in Fig 1.5 A. When light travels from a medium with a higher- refractive-index (n_1) to a medium with lower-refractive-index (n_2), the light beam will split into two parts: some light is refracted with angle r and the rest will reflect with incident angle i . They obey the Snell's law: $\sin(i)/\sin(r)=n_2/n_1$. If the incident angle i exceeds a certain critical angle, light cannot pass into the lower-refractive-index medium n_2 , and is completely reflected into the denser optical medium n_1 . At the interface between n_1 and n_2 there will be a thin (usually less than 200 nm) electromagnetic field called the evanescent field. The evanescent field is often ignored since it can not be detected on the micrometer-length scales typically relevant in far-field light microscopy. In the mid-1980s Daniel Axelrod and his

colleagues pioneered TIRF microscopy for biological applications. Since the evanescent field is parallel to the interface and its energy intensity decays exponentially with distance from the interface, the evanescent wave can only excite fluorophores which are very near the interface. In cells grown on coverslips, only those fluorophores which are near the cell membrane where it is in contact with the coverslip are illuminated. This illuminated area corresponds to the cell's footprint (shown in Fig 1.5 B).

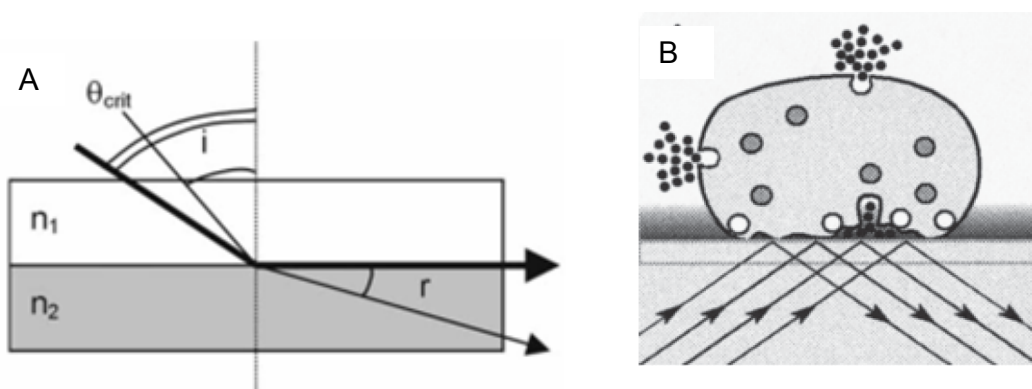


Fig.1.5 (A) The principle of total internal reflection. The light beam travels from n_1 to n_2 and is split into a refracted beam with r and a reflected beam with i . If i exceeds θ , light cannot then pass into the second medium n_2 . n : refractive index, $n_1 > n_2$, i : incident angle, θ : critical angle, r : refracted angle. See text for more details. (Mashanov, Tacon et al. 2003) **(B) Principle of evanescent wave excitation.** A light beam is directed to a dielectric interface. Total internal reflection sets up evanescent field (grey shading; drawing not to scale) that excites fluorophores in chromaffin granules which are close to the interface and those granules located deeper in the cytoplasm shown can not be excited by the evanescent field. (Oheim 2001)

1.7 Proteins involved in exocytosis

Synaptic vesicles are filled with neurotransmitter. After genesis and filling, they are transported to the active zone, where multiple proteins provide a scaffold for vesicle docking and priming (Fig.1.6). After fusion, vesicle proteins are retrieved by a clathrin-mediated endocytosis. During the last two decades, intense research has focused on the proteins participating in exocytosis. To fuse, two opposing membranes must overcome large energy barriers. Soluble NSF Attachment Protein Receptors (SNAREs) are the engines for membrane fusion (Jahn and Scheller 2006). . SNARE protein is ternary complex, consisted of syntaxin and Synaptosome Associated Protein of 25 kD (SNAP-25) or in some cell types like T cells its homologue, SNAP23 and synaptobrevin2 (syb2, a.k.a. VAMP2) or in some cells its

homologue, cellubrevin (a.k.a. VAMP3) (Chen and Scheller 2001). Syb2 located on vesicle membrane is a so called “V-SNARE” whereas SNAP-25 and syntaxin reside on target membrane and are referred to as “t-SNAREs”.

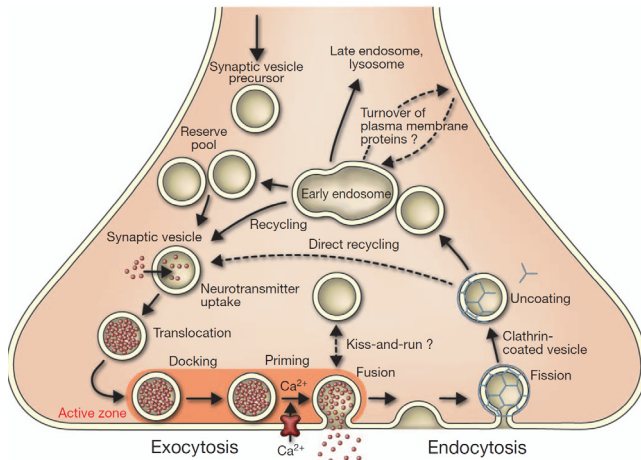


Fig.1.6 Trafficking pathways of synaptic vesicle in the nerve terminal. Synaptic vesicles are filled with neurotransmitter and translocated to active zone where they go through docking and priming. When an action potential arrives, calcium influx and stimulated exocytosis. After exocytosis, the vesicle proteins are retrieved by clathrin-mediated endocytosis. The clathrin-coated vesicles go through uncoating state and passage through an endosomal intermediate. Recycling vesicles are in slow exchange with the reserve pool. (Jahn and Fasshauer)

1.7.1 SNAREs: The “Zippering” model and the binding partners

In 1998, Sutton et al (Sutton, Fasshauer et al. 1998) reported the X-ray crystal structure at 2.4Å resolution of a SNARE complex containing syntaxin-1A, syb2 and SNAP-25B (shown in Fig1.7). These proteins form twisted and parallel four α-helical bundles, two from SNAP-25, and one each from syntaxin-1A and syb2 (Sutton, Fasshauer et al. 1998). The amino acids were divided into five classes, hydrophobic (Ala, Val, Phe, Ile, Leu, Pro, Met), positively charged (Lys, Arg), negatively charged (Asp, Glu), hydrophilic (Ser, Thr, Tyr, Cys, Asn, Gln, His, Trp), and glycine. The four-helix bundles consist of 16 sets of four amino acids orienting to the interface of the four helices, referred to as layers. At the center of the sequence is the so-called ionic layer consisting of glutamine and arginine, also called the zero layer. A sequence alignment restricted to these 16 layers for a representative subset of the entire SNARE family is shown in Fig.1.8. The conserved glutamine and arginine residues forming the ionic 0 layer are indicated in red and green, respectively. SNARE proteins have been reclassified into Q-SNAREs and R-SNAREs based on the amino acid of the zero layer (Fasshauer, Sutton et al. 1998).

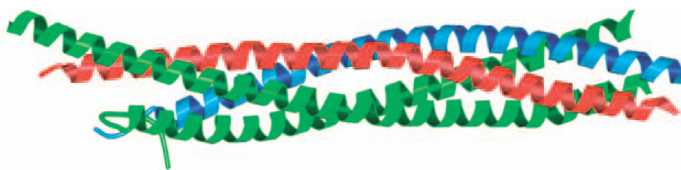


Fig.1.7 Ribbon diagrams of the structure of the SNARE core complex. Red: syntaxin-1; green: SNAP-25; blue: synaptobrevin. The C-terminal ends of the helices, which all point towards the membrane, are orientated to the right (Jahn and Scheller 2006).

Ternary SNARE complexes exhibit a dramatically increased in thermal stability and are also resistant to treatment with SDS (Fasshauer, Otto et al. 1997) when compared to the individual SNARE proteins(Hanson, Heuser et al. 1997). The

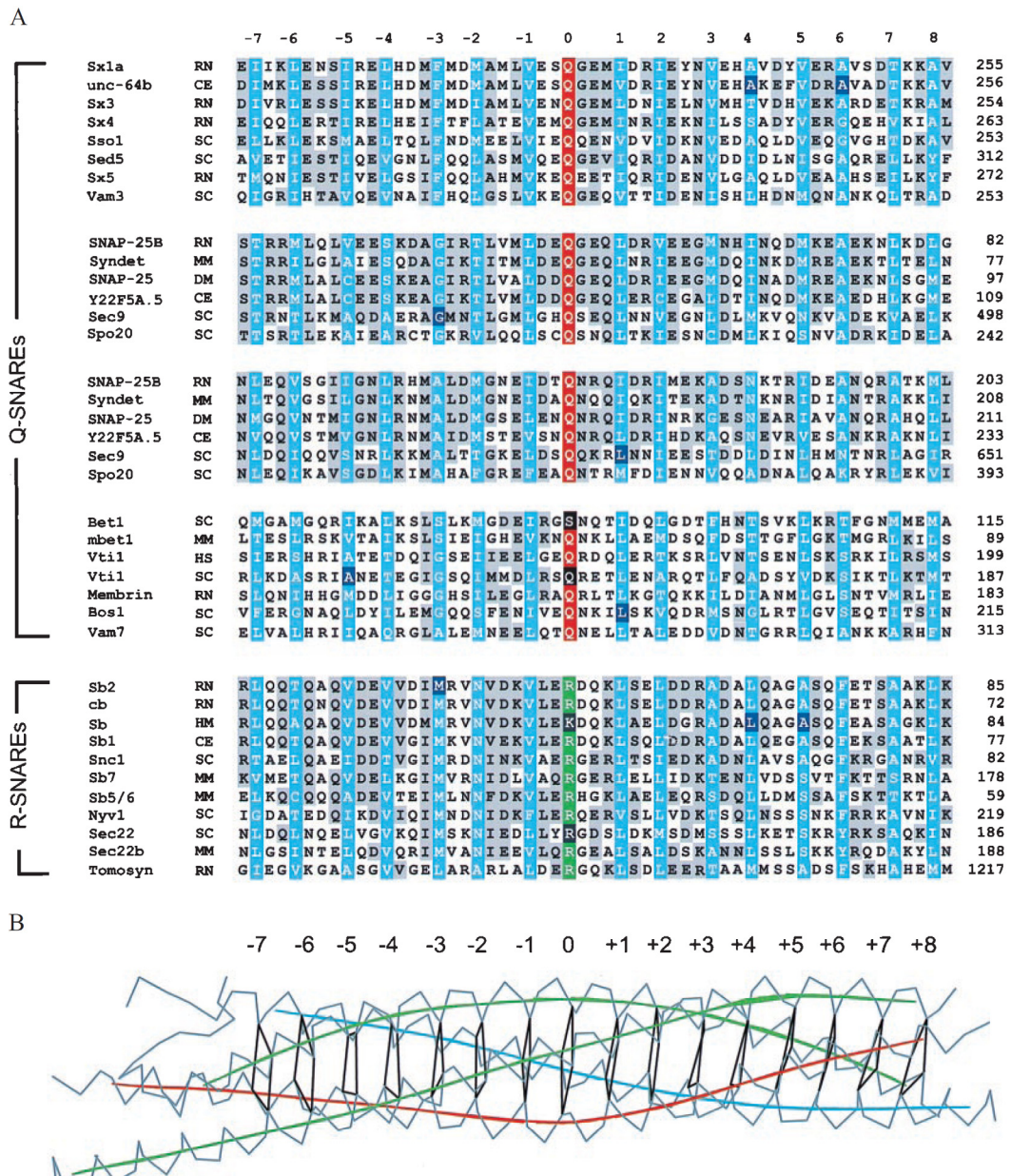


Fig.1.8 (A) **Sequence alignment of the four-helix bundle region of the synaptic fusion complex for a representative subset of the entire SNARE family.** Conserved residues in 16 layers (blue) are shown in gray. Glutamine (Q) and and arginine (R) in layer zero are marked in red and green, respectively. (B) Layers of the synaptic fusion complex crystal structure. Ca traces is shown in gray. Local helical axes of blue, red, and green are for syb2, syntaxin-1A, and SNAP-25b, respectively, and layers in black are by virtual bonds between corresponding Ca positions.(Fasshauer, Sutton et al. 1998)

presence of the coiled coil composed of four helices contributed by the three SNARE proteins was consistent with the idea that the SNARE complex assembled between two opposing membranes and as the apposed coils “zippered up” the opposing membrane were brought into close proximity and eventually were forced to fuse, using energy generated by the zippering of the SNARE complex. The released energy would be used to overcome the energy barriers for membrane fusion. The zippering model proposes (shown in Fig.1.9) that trans-SNARE complex (a.k.a SNAREpins) assemble progressively from the membrane-distal N termini toward the membrane-proximal C termini and this generates force that pulls the opposing bilayers together until fusion occurs. The SNAREs then transform to the low-energy -- cis-SNARE complex conformation (Sudhof and Rothman 2009). Several proteins are involved in this procedure. A crucial step in SNARE complex formation is rapid binding of vesicular synaptobrevin to the preformed syntaxin 1·SNAP-25 dimers. The coiled-coil layers on synaptobrevin between layer -4 and layer -2, termed the trigger site, is important for productive SNARE zippering (Wiederhold, Kloepper et al.)

N-terminal mutations of the coiled-coil layers in synaptobrevin inhibit binding of synaptobrevin to syntaxin 1·SNAP-25 dimers in vitro and vesicle priming in vivo, without detectable changes in triggering speed or fusion pore properties. In contrast,

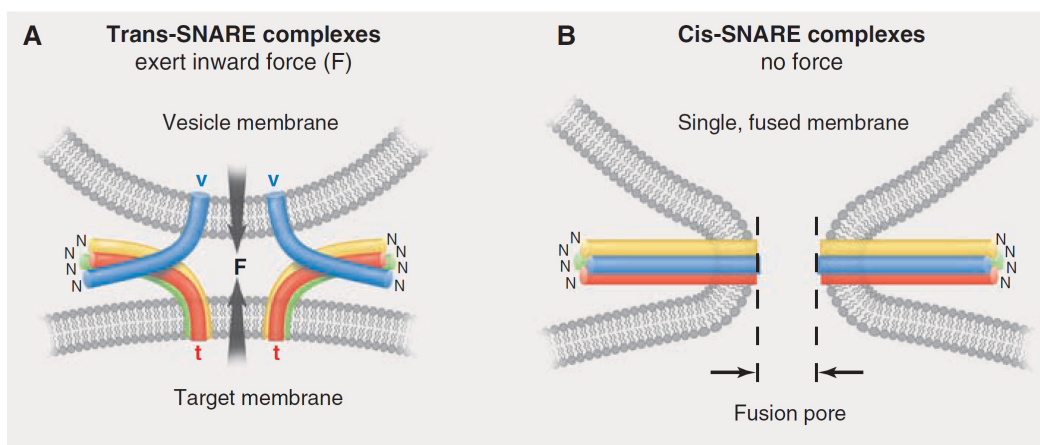


Fig.1.9 The zippering model for SNARE-catalyzed membrane fusion. SNARE complexes assemble at the N-terminal end (N) and progressively proceed to C-terminal. At fusion, the zippering providing the force (F) which leads to fusion of the two membranes. (B) Therefore, when fusion pore has formed, the force vanishes and the SNAREs are in cis-SNARE complex (Sudhof and Rothman 2009).

mutations in the last C-terminal layer decrease triggering speed and fusion pore duration (Walter, Wiederhold et al.).

Syb2 is an integral membrane protein of 18000 Daltons (Baumert, Maycox et al. 1989). It is conserved throughout the animal kingdom, and contains around 116 amino acids (shown in Fig.1.10). Cellubrevin, shares a high degree of similarity with syb2 (shown in Fig.1.11) and in mouse chromaffin cells efficiently substitutes for Ca²⁺-dependent exocytosis (Borisovska, Zhao et al. 2005). Syb2 contains two amphipathic α helices: helix 1(residue 39-53), is hydrophobic and may interact with lipids during the process of membrane fusion; Helix 2(residue 60-88) may interact with a similar amphipathic helix on another protein in a coiled-coil structure. Amino acids throughout helix 1 are essential for targeting to synaptic vesicles. (Grote, Hao et al. 1995)

The structure of SNAP-25 is shown in Fig.1.12. It was reported that mutation

```

1
Met Ser Ala Thr Ala Ala Thr Val Pro Pro Ala Ala Pro Ala Gly Glu Gly Gly Pro Pro Ala Pro Pro Pro Asn Leu Thr Ser Asn Arg
ATG TCG GCT ACC GCT GCC ACC CTC CCG CCT GCC GCC CCG GCC GGC GAG GGT GGC CCC CCT GCA CCT CCT CCA AAT CTT ACC AGT AAC AGG
102
31
Arg Leu Gln Gln Thr Gln Ala Gln Val Asp Glu Val Val Asp Ile Met Arg Val Asn Val Asp Lys Val Leu Glu Arg Asp Gln Lys Leu
AGA CTG CAG CAG ACC CAG GCC CAG GTG GAT GAG CTG GTG GAC ATC ATG AGG GTG AAT GTG GAC AAG CTC CTG GAG CCG GAC CAG AAG CTA
192
61
Ser Glu Leu Asp Asp Arg Ala Asp Ala Leu Gln Ala Gly Ala Ser Gln Phe Glu Thr Ser Ala Ala Lys Leu Lys Arg Lys Tyr Trp Trp
TCG GAA CTG GAT CAT CCG GCA GAT GCC CTC CAG GCA GGG GCC TCC CAG TTT CAA ACA AGT GCA GCC AAG CTC AAG CGC AAA TAC TGG TGG
282
91
Lys Asn Leu Lys Met Met Ile Ile Leu Gly Val Ile Cys Ala Ile Ile Leu Ile Ile Ile Ile Val Tyr Phe Ser Thr ***
AAA AAC CTC AAG ATG ATG ATC ATC TTG GGA GTG ATT TGC GCC ATC ATC CTC ATC ATC ATC ATC GTT TAC TTC AGC ACT TAA GTCCCTGAGGA
374
GTCTGCCCTCCTAAGAAGGGCCTCTCCCCACCCCTCAGCCCGTCTCTCCACCTCTCAGCCATATCTTTGAGCCCCCTCCCTTGGATCCGTGTGTGTGTGTCCGGTGTGTGCACCCCT
493
GTAATAGCCAGCTGTTATTATACATATATAATATTATATATATTTGGCTGTTTGTAGTTTTATTACTAGAAGATTTT
573

```

Fig.1.10 Nucleotide sequences of the rat syb2 cDNA clones. The amino acid sequence is numbered on the left and the nucleotide sequence on the right.(Elferink, Trimble et al. 1989)

b

Rat Ceb	MSMGVPSGSSAATGSNRRLQQTQNVQVDEVDIMRVNVDKV	53
Rat Syb II	MSATAATVPPAAPAGE.G.PAPPPNLT.....A.....	53
Bovine Syb II	MSATAATAPPAAPAGE.G.PAPPPNLT.....A.....	53
Human Syb II	MSATAATAPPAAPAGE.G.PAPPPNLT.....A.....	53
Rat Syb I	MSAPAQPPAEGTEGAAPG.G.P.PPPN.T.....A..E.....I.....	55
Human Syb I	MSAPAQPPAEGTEGAPG.G.P.PPPNMT.....A..E.....I.....	55
Torpedo Syb I	MSAPPSGPAPDAQGAPGQPTG.P.APPN.T.....A..E.....I.....	57
Drosophila	MENNEAPSPSGSNNNDFPILPPPPNANDNYNQFGHQIRNNNAQKK.....AK.....G.....E..	69
	LERDQKLSLDDRADALQAGASQFETSAAKLKRKYWWKNCKMWAIGISVLVIVIIIVWCVS*	103
L..MI..LGVICA..L.....YFST*	116
L..MI..LGVICA..L.....YFS.*	116
L..MI..LGVICA..L.....YFS.*	116
V..S.....MIMLGAICA..VV.VIYIFT*	118
S.....MIMLGAICA..VV.VIYFFT*	118
S.....MIMLGGIGA..V..IYFFT*	120
GE...Q.EQ.....QQ.G.....Q..A.M..MI..LGVIA.VLL..VL.SVWPSSSDSGGGGNKAITQAPP*	152

Fig.1.11 Amino acid alignments of cellubrevin with synaptobrevins for maximum homology. Period refers to residues in synaptobrevins identical to those in cellubrevin. Synaptobrevins from different species share 59% sequence identity. Ceb: cellubrevin (McMahon, Ushkaryov et al. 1993)

of conserved Q residues in SNAP-25 or the yeast homologue Sec9 reduces the affinity of SNARE-SNARE interactions and reduces the thermal stability of the

SNARE complex assembled *in vitro*, however, disruptive mutations in the 0 layer that impair SNARE-SNARE interactions and SNARE complex stability do not prevent exocytosis (Graham, Washbourne et al. 2001). The four-helix bundles form in the N- to C-terminal direction. In order to destabilize complex, alanine substitutions were introduced to different places in SNAP-25. The mutation in C-terminal end of the bundles can still assemble/disassemble independently of N-terminal of the bundles but exocytosis was affected by these mutations, whereas mutations in N-terminal of the bundles have no effects on mouse chromaffin cell exocytosis. Mutations in the middle of bundles selectively interfered with priming of new vesicles for release, but did not alter the kinetics of fusion of those vesicles that were already primed (Sorensen, Wiederhold et al. 2006). Alanine substitutions in SNAP-25 were also tested on cultured autaptic hippocampal neurons. Substitutions in C-terminus of the bundles abolishes spontaneous neurotransmitter release and reduces evoked release probability in cultured autaptic hippocampal neurons, however, substitutions in N-terminal end or middle of the bundles increases both spontaneous and evoked release probabilities (Weber, Reim et al.). The coiled-coil bundle is held together by layers of hydrophobic interaction, with the exception of the zero layer which is formed by an arginine and three glutamines (Sutton, Fasshauer et al. 1998). Palmitoyl side chains of SNAP-25 termed the SNAP-25 linker run back along the complex from the C-terminal end of the first (Qb) SNARE-domain and connects to the N-terminal end of the second SNARE-domain (Qc). It has been suggested that the SNAP-25 linker therefore served as an adaptation allowing calcium triggering as well as rapid fusion. (Nagy, Milosevic et al. 2008)

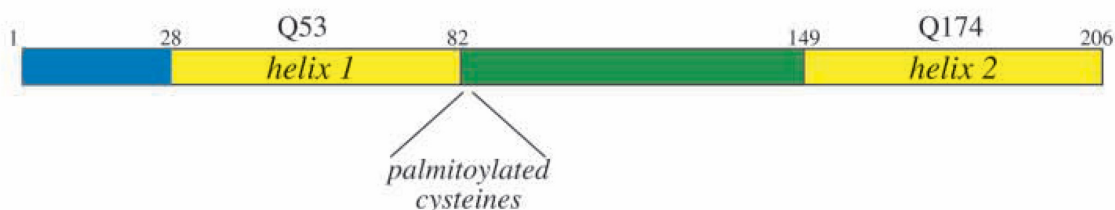


Fig.1.12 Domain structure of SNAP-25. The number of residues is shown above the diagram. (Graham, Washbourne et al. 2001).

Syntaxins possess an N-terminal Habc domain (Ha, Hb, Hc in Fig.1.13), a SNARE motif (known as H3), and a single C-terminal transmembrane domain (Fig.1.13). The Habc domain contains three long alpha helices that form a folded bundle with a left-handed twist and is very stable, with a denaturation temperature of more than 80°C (Fernandez, Ubach et al. 1998). Sec1/Munc18 (SM) proteins are

required for every step of intracellular membrane fusion (Shen, Tareste et al. 2007). Munc18-1 binds to syntaxin-1 folded into a closed conformation and to SNARE complexes containing open syntaxin-1; in addition, Munc18-1 and complexin-1 bind simultaneously to SNARE complexes (Deak, Xu et al. 2009). Munc13-1 (Fig. 1.13) plays a central role in vesicle priming by accelerating the rate constant of vesicle transfer from a pool of docked but unprimed vesicles to a pool of release competent, primed vesicles (Ashery, Varoqueaux et al. 2000). Its MUN domain markedly accelerates the transition from the syntaxin-1–Munc18-1 complex to the SNARE complex. This activity depends on weak interactions of the MUN domain with the syntaxin-1 SNARE motif, and probably with Munc18-1 (Ma, Li et al.)

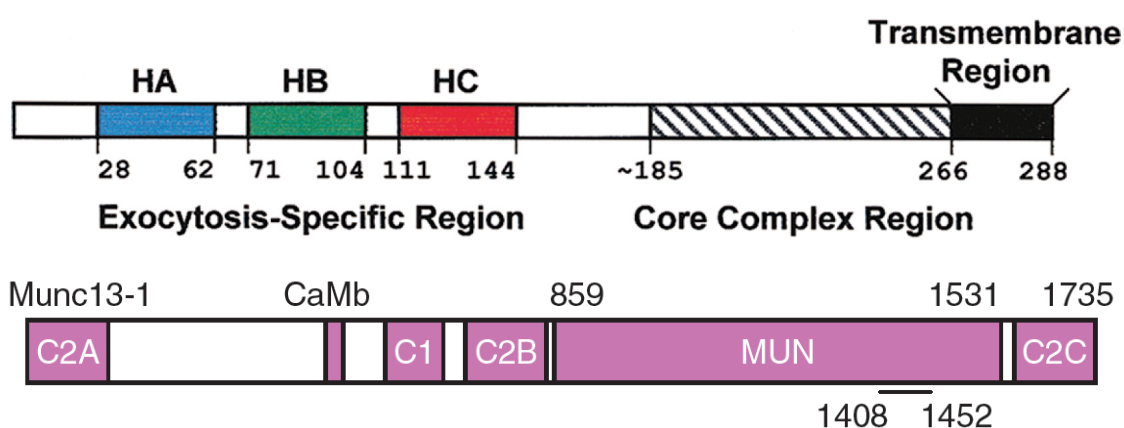


Fig.1.13 Domain diagrams of Syntaxin-1(Fernandez, Ubach et al. 1998) **and Munc13-1**(Ma, Li et al.) . The number of residues of each protein is indicated below each diagram.

Synaptotagmin, a 65-kDa protein, was identified in 1981 and was reported to localize to vesicles in neurons and neuroendocrine cells. It contains a single membrane spanning domain, a short intraluminal domain, and a large cytoplasmic domain consisting of tandem C2 domains, C2A and C2B, connected by a linker (Chapman 2008). Synaptotagmin, binding to plasma membrane bound SNAP-25 can dock vesicles (Schiavo, Stenbeck et al. 1997). Moreover, Synaptotagmin I functions as a Ca^{2+} -regulator of release probability (Fernandez-Chacon, Konigstorfer et al. 2001) via its C2 domains.

Synaptotagmins do not act alone. The complexins, small proteins that bind in an antiparallel alpha-helical conformation to the groove between the synaptobrevin and syntaxin helices (Chen, Tomchick et al. 2002), simultaneously clasping the SNAREpin, that results in blocking fusion, (Giraudo, Eng et al. 2006) and positioning the SNARE complexes for a rapid response to calcium bound synaptotagmin (Sudhof 2012).

In summary, shown in Fig.1.14, Q-SNAREs assemble into acceptor complexes which require SM proteins. Acceptor complexes interact with the vesicular R-SNAREs through the N-terminal end of the SNARE motifs, and form a four-helical trans complex. Trans complexes zipper from the N-terminal portion of the SNARE motifs to a tight cis-conformation. This procedure is controlled by auxiliary proteins such as the docking factor munc-18, priming factor munc-13, the Ca^{2+} sensor synaptotagmin and the modulatory protein complexins. In concert these molecules allow fusion and eventual recycling of used SNARE complexes (Jahn and Scheller 2006).

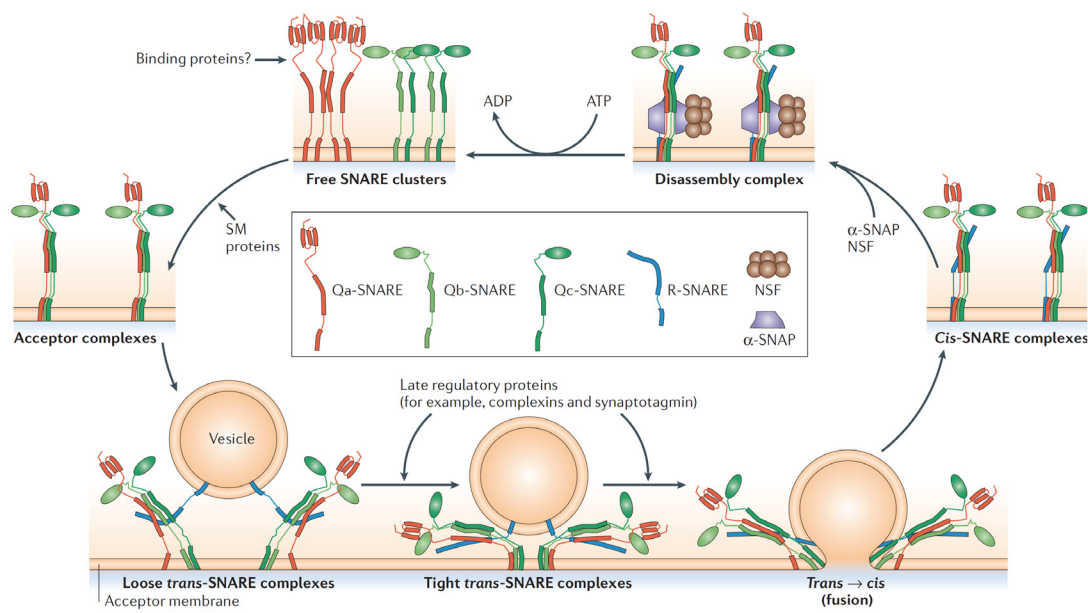


Fig.1.14 The SNARE conformational cycle during vesicle docking and fusion. Q-SNAREs reside on acceptor membrane and R-SNARE attach to the vesicle. With the aid of SM protein, Q-SNAREs assemble into acceptor complexes. Acceptor complexes then interact with R-SNAREs through the N-terminal end of the SNARE motifs, and this nucleates the formation of a four-helical trans complex which are regulated by late regulatory proteins. Trans-complexes zipper from N-terminal end towards C-terminal and generate force which causes the formation of the fusion pore. During fusion, the strained trans-complex relaxes into a cis-configuration. Cis-complexes are disassembled by protein NSF (N-ethylmaleimide-sensitive factor) and its cofactor α -SNAPs. After that the R- and Q-SNAREs are retrieved by endocytosis. (Jahn and Scheller 2006).

1.7.2 Ca^{2+} and depolarization

Stimulation-secretion coupling in chromaffin cells occurs in the following order: (i) stimulation of the acetylcholine receptor opens the pore of the receptor allowing entry of Na^+ and Ca^{2+} ; (ii) which causes a depolarization that in turn induces the opening of voltage-dependent Na^+ channels; (iii) the resulting large depolarization

opens voltage-sensitive Ca^{2+} channels; (iv) which leads to a rise in intracellular calcium and triggers fusion of primed granules with the plasma membrane (Aunis and Langley 1999). When we patch chromaffin cells in voltage-clamp mode, depolarizing pulse can be used to open voltage-sensitive Ca^{2+} channels directly, which results in calcium influx through these channels. Steep spatial calcium gradients are formed, and sum to microdomains where the Ca^{2+} concentration reaches tens of micromoles/liter near the Ca^{2+} channels. This increase in calcium concentration rapidly releases fusion-competent vesicles in close proximity to the Ca^{2+} channels. This pool is called immediately releasable pool (IRP). The IRP is a subpool of the RRP, which is not more release-ready than the rest of RRP (Voets, Neher et al. 1999). The IRP can be activated by a train of four 10 ms depolarizing pulses, whereas trains of longer (100 ms) depolarizations are required to release the RRP (Stevens, Schirra et al.). However, even long depolarizing pulses are not sufficient to release the SRP which can, however, be triggered by flash measurement (Voets, Neher et al. 1999).

Increases in intracellular calcium not only trigger release, they also promote vesicle maturation (refer to priming in Fig.1.1). In a series of experiments using flash photolysis of caged calcium as a trigger for exocytosis it was shown that the preflash intracellular Ca^{2+} concentration (basal $[\text{Ca}^{2+}]_i$) regulates the size of both the SRP and the RRP (Voets 2000) At basal $[\text{Ca}^{2+}]_i$ levels below ~600 nM, both the SRP and the RRP increase in size with increasing $[\text{Ca}^{2+}]_i$. At basal $[\text{Ca}^{2+}]_i$ above ~600 nM the size of the RRP declines more rapidly than the SRP. The maximum RRP was observed at an intracellular free Ca^{2+} concentration of ~600 nM.

However, $[\text{Ca}^{2+}]_i$ has no major effect on LDCV docking phenomenon as judged by electron micrographs of bovine chromaffin cells (Plattner, Artalejo et al. 1997).

1.7.3 Transmembrane domain of Syb2

During the past two decades, much has been learned about the mechanism of SNARE-mediated membrane fusion and its interaction proteins, however, the interplay between SNARE proteins and membrane lipid is still poorly understood. Syb2 localizes to the vesicle membrane and its transmembrane domain (TMD) consists of about 23 amino acids. This domain is highly conserved suggesting that it is very important in fusion (Fig.1.15).

Syb2 molecules were found to form dimers via their TMDs in intact cells. Residue 100, a glycine, which is located in the TMD and is crucial for this dimerization and the mutants replacing this glycine is exchanged with amino acid tyrosine, valine or arginine are still fully competent in bringing membrane-fusion events. Mutantations in sequence 110-116 aa induced deficits in fusion, whereas deletions or insertion in sequence 96-99aa did not display severe secretory deficits (Fdez, Martinez-Salvador et al.).

The TMD of syb2 first inserts into the ER membrane independently of the SRP/Sec61p pathway and is then transported to synaptic vesicles. Ideal hydrophobic segments are composed of 11-17 leucines and 1 valine and function as insertion sequences and form transmembrane anchors in vitro whereas shorter segments do not (Whitley, Grahn et al. 1996). Another function of TMD of syb2 is to promote lipid mixing independently of SNARE complex formation. The conformation study revealed that the TMD has an α -helical structure and adopts a 36° angle with respect to the outer surface of the membrane, similar to viral fusion peptides (Bowen and Brunger 2006). During facilitation of liposome fusion by the TMD, the TMD was observed to exist in an α -helical and a β -sheet conformation which coexisted in membranes (Langosch, Crane et al. 2001). Wissam Yassine et al. pointed out that the TMD of syb2 adopts an α -helical or β -sheet conformation depending on the concentration of surrounding lipid. The switch between these two conformations was reversible and dynamic (Yassine, Taib et al. 2009).

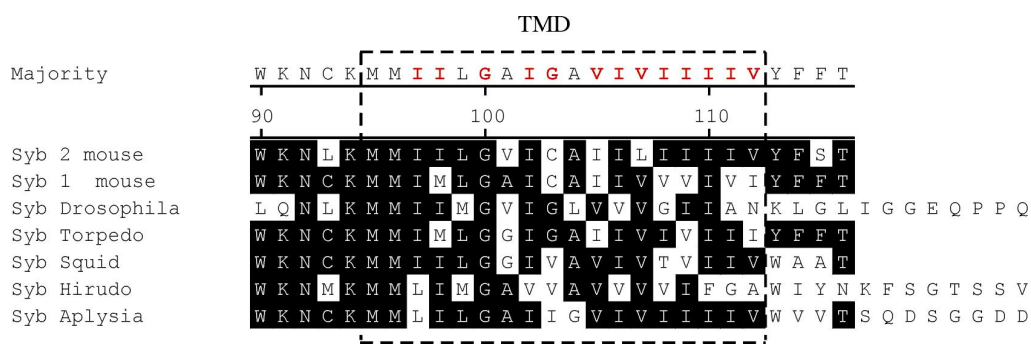


Fig.1.15 Sequence comparison within TMD synaptobrevins. There is a high content of helix-destabilizing amino acids (isoleucine and valine) within the transmembrane domain. More than 50 percent of the amino acids of the TMD are helix-destabilizing (red). Numbers refer to amino acid position of mouse syb2. (figure provided by Prof. Dieter Bruns).

1.8 Goal of the project

Syb2, as a component of the SNARE complex, plays an important role in exocytosis. It is largely unknown whether TMD on syb2, which anchors it in the vesicle membrane, also functions directly in exocytosis. As described above, syb2 TMD-peptide can drive liposome-liposome fusion. In addition, the conformation switch between α -helix and β -sheet was observed in in vitro experiments. Correlating the function of full-length syb2 in vivo with that of the TMD will further clarify its role at different stages of membrane fusion.

The goal of this project was to investigate the importance of the TMD of syb2 in Ca^{2+} -dependent exocytosis in chromaffin cells. As described above, mouse chromaffin cells express syb2 and its homologue cellubrevin. We have used syb2/cellubrevin double knockout (DKO) mice as a genetic null background, and have expressed syb2 carrying specific mutations within TMD into this genetic null background and studied how exocytosis is affected, to examine the role of the TMD of syb2 in exocytosis.

I first established the method of TIRF microscopy on mouse chromaffin cells and then examined whether the TMD controls steps prior to fusion in mouse chromaffin cells. In the next set of experiments, I have replaced TMD with a polyleucine stretch of equivalent length or shorter length, to examine how this linker, which tends to adopt an α -helical conformation, influences exocytosis. It has been reported that when valine and isoleucine which tend to form β -sheet, were overrepresented in the TMD without changing overall length, (Fig1.15) (Langosch, Crane et al. 2001) function was not affected. Our results will extend these findings and add to our understanding of how TMD of syb2 functions during Ca^{2+} -dependent exocytosis.

2. Materials and Methods

2.1 Materials

2.1.1 Reagents

Name of product	Company provider
Albumin	Sigma
Aprotinin	Sigma
ATP(-Mg)	Sigma
Bovine serum albumin (BSA)	Sigma
CaCl ₂ (1M standard solution)	BDH
CaCl ₂ × 2 H ₂ O	Merck
Caesium hydroxide (CsOH)	Sigma
Chymotrypsin	Sigma
DMEM	Invitrogen
EDTA	Sigma
Ethanol	Roth
Fetal calf serum (FCS)	Invitrogen
GTP(-Na)	Sigma
Glucose.H ₂ O	Merck
HEPES	Sigma
HPLC-H ₂ O	Merck
Insulin Transferrin Selenium	Invitrogen
Ethanolamine Solution (ITS-X)	
KCl	Merck
KH ₂ PO ₄	Merck
L-Cysteine	Sigma
L-Aspartic Acid	Sigma
L-Glutamic Acid	Sigma
MgCl ₂ × 6H ₂ O	Merck
NaCl	Merck
NaHCO ₃	Merck
Na ₂ HPO ₄	Merck
OptiMEM	Invitrogen

Papain	Roche Worthington
Penicillin-Streptomycin (Pen / Strep)	Invitrogen
Trpsin inhibitor	Sigma
Tryptose phosphat	Invitrogen

2.1.2 Enzymes

Chymotrypsin	Sigma
Papain	Worthington
Trypsin	Invitrogen

2.1.3 Solutions

2.1.3.1 Solutions for mouse chromaffin cell preparation

Locke´s solution

154 mM	NaCl
5.6 mM	KCl
0.85 mM	Na ₂ HPO ₄
2.15 mM	KH ₂ PO ₄
10 mM	Glucose

pH 7.4, ~ 312 mOsm, store 4°C

Papain solution

50 ml	DMEM
10 mg	L-Cysteine (activates the papain)
0.5 ml	100 mM CaCl ₂
0.5 ml	50 mM EDTA (activates the papain)

in 2 ml aliquots, store -20°C

Inactivation solution

50 ml	DMEM
5 ml	FCS
125 mg	albumin
125 mg	trypsin inhibitor

sterile filtered

in 2 ml aliquots , store -20°C

Medium

40 ml	DMEM
400 µl	ITS-X
160 µl	Pen / Strep (1 ml aliquots store -20°C)

20 min before cell preparation, we need to thaw the aliquots, and add 15 to 20 units papain per 1 ml enzyme solution. Then bubble the mixture with carbogen for 20 minutes, and filtered under sterile bench.

after thawing incubate at 37°C , 9% CO₂ incubator

2.1.3.2 Solutions for virus activation

HBS

140 mM	NaCl
10 mM	HEPES
5 mM	KCL
10 mM	MgCl ₂ × 6 H ₂ O
20 mM	CaCl ₂ × 2 H ₂ O

pH 7.2, ~ 359 mOsm

OptiMEM without FCS + 0.2% BSA

44 ml	OptiMEM
5 ml	Tryptose phosphate
1 ml	1 M HEPES
50 µl	Pen / Strep
0.1 g	BSA

sterile filtered, store at 4°C

Aprotinin

6 mg / ml in HBS

110 µl aliquots store at -20 °C

Chymotypsin

2 mg / ml in HBS

100 µl aliquots store at -20 °C

2.1.3.3 Solutions for measurements

Normal Extracellular solution

144.5 mM	NaCl
2.4 mM	KCl

10 mM	HEPES
4 mM	MgCl ₂
1 mM	CaCl ₂
10 mM	Glucose

pH 7.2, ~310 mOsm

Extracellular solution for depolarization experiment

147 mM	NaCl
2.4 mM	KCl
10 mM	HEPES
1.2 mM	MgCl ₂
2.5 mM	CaCl ₂
10 mM	Glucose

pH 7.2, ~310 mOsm

Intracellular solution 502 for depolarization experiment

2 mM	CsEGTA
10 mM	HEPES
140 mM	CsAspAcid
1.46 mM	CaCl ₂
1 mM	MgCl ₂
0.3 mM	Na ₂ GTP
2 mM	MgATP
8 mM	NaCl

pH 7.2, ~305 mOsm

Free Ca²⁺ 502 nM

Intracellular solution 404 for depolarization experiment

10 mM	HEPES
140 mM	CsAspAcid
1.37 mM	CaCl ₂
1 mM	MgCl ₂
0.3 mM	Na ₂ GTP
2 mM	MgATP
8 mM	NaCl
2 mM	CsEGTA

pH 7.2, ~300 mOsm

Free Ca²⁺ 404 nM

2.2 Methods

2.2.1 DNA constructs and semliki forest virus

The Semliki Forest virus (SFV) replicon was developed as a novel DNA expression system. DNA of interest is cloned into SFV plasmid vectors that serve as templates for in vitro synthesis of recombinant RNA. Within the cell, the recombinant RNA drives its own replication and capping and leads to massive production of the heterologous protein, effectively competing with the host's protein synthesis (Liljestrom and Garoff 1991). However, the system was hampered by special requirements for RNA handling and stringent biosafety procedures until the introduction of helper construction. A helper variant was developed with a mutation in the gene encoding the viral spike protein through which its product cannot undergo normal proteolytic processing to activate viral entry functions. Hence, the recombinant stock is noninfectious, but may be activated by cleavage with chymotrypsin (Berglund, Sjoberg et al. 1993). As an alphavirus, SFV possess several important features: first, SFV has a wide host range and can infect almost any mammalian cell; second, the virus can be produced and harvested in 2 days; third, the output of target protein can reach up to 25% of total cellular protein; finally, the virus can only infect after activation by chymotrypsin, greatly reducing the danger associated with its application (DiCiommo and Bremner 1998). In 1999, the SFV gene expression system was successfully used to introduce munc13-1 into cultured bovine chromaffin cells. Within 12-48 hours, up to 40% of cells expressed the protein of interest. Thus the suitability of the method for expression studies in bovine chromaffin cells was established (Ashery, Betz et al. 1999). These authors demonstrated that the cells remained viable long enough to express moderately large proteins and that overexpression led to the expected changes in function. Infected cells remained viable up to 36 hours.

In 1982, Neuropeptide Y (NPY) was isolated from porcine brain (Tatemoto 1982). This 36-amino acid peptide was also present in adrenal glands of several species, including cat, mouse, rat, horse, and guinea pig (Allen, Adrian et al. 1983), and sorted into LDCVs. Bovine chromaffin cells are a rich source of NPY with 430 equivalents per single granule being expressed (Winkler 1993). For this reason NPY

conjugated with or coexpressed with a fluorescent dye or protein is an excellent tool for labeling LDCVs in chromaffin cells.

For overexpression of syb2 or introduction of mutations, cDNAs were introduced into modified pSFV1 vector followed by an internal ribosome entry site (IRES) from poliovirus with NPY-mCherry. Picornavirus IRES elements direct cap-independent internal initiation of protein synthesis within mammalian cells (Robertson, Seamons et al. 1999) and allows for translation initiation in the middle of a messenger RNA sequence. Vector pSFV1-IRES-NPY-mCherry was obtained by replacement mRFP from pSFV1-Nur I-IRES-NPY-mRFP (from Dr.Ulf Matti) with mCherry from pSFV1-NPY- mCherry (from Dr.Ulf Matti). The mCherry fragment in pSFV1-NPY-mCherry was cut by Age1/ Spe I restriction sites. The vector pSFV1-Nur I-IRES-NPY-mRFP was cut by Cla I/Age I and Age1/ Spe I restriction sites resulting in pSFV1-Nur I-IRES, and NPY- mRFP respectively. Parts of pSFV1-Nur I-IRES, NPY and mCherry were linked. The full-length syb2 and mutations were provided by Prof.Dieter Bruns and inserted upstream of the IRES by using BamHI and BssHII restriction sites (Fig.2.1). The 5' overhang was filled in by Klenow Fill-In, which can perform a complete fill-in to generate blunt end for direct ligation. The mutated nucleotide sequence of all constructs was verified by DNA sequencing.

```

WT      K M M I I L G V I C A I I L I I I I V Y F S T
polyL   K M M L L L L L L L L L L L L L L L L L L Y F S T
polyV   K M M V V V V V V V V V V V V V V V V V Y F S T
polyI   K M M I I I I I I I I I I I I I I I I I Y F S T
WTΔ4I  K M M I I L G V I C A I I L           V Y F S T

```

Fig.2.1 Sequences (95-112 aa) of syb2 and mutations for my measurements. Amino acids within TMD are depicted in red. Abbreviations of wild type syb2 (WT), TMD in syb2 replace by polyLeucine (polyL), polyValine (polyV) polyIsoleucine (polyI), and type syb2 deletion of four isoleucine within TMD (WTΔ4I).

Virus activation

Virus was activated on the day that measurements were performed. The procedure was: thaw 450 µl virus aliquot. Under sterile conditions, mix 450 µl OptiMEM without FCS + 0.2% BSA with the aliquot and then place 100 µl Chymotrypsin to the mixture and mix again. After waiting 40 minutes at room temperature, add 110 µl Aprotinin was added to terminate activation.

2.2.2 Knockout mice and mouse chromaffin cell culture

Mice with deletions of syb2 and cellubrevin protein were kindly provided by Prof. Dieter Bruns. The syb2 and cellubrevin double knock-out mice die shortly after birth, so their embryos [embryonic day 18.5 (E18.5) and E19] were prepared after cervical dislocation and delivery by caesarean section. Appearance of DKO mouse embryos was different from littermate cellubrevin knock-out mice (Fig.2.2). Mice genomic DNA was verified by Prof. Dieter Bruns' lab.

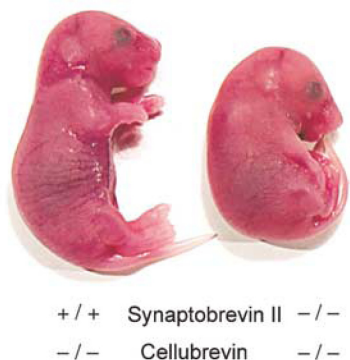


Fig.2.2 Appearance of syb2/cellubrevin double knock-out mice(right) at stage E18.5 compared with littermates cellubrevin knock-out(left).(Borisovska, Zhao et al. 2005).

Pregnant mice at stage E18.5 or E19 were asphyxiated by carbon dioxide and decapitated. The embryos were removed by caesarean section. Embryos were decapitated and both adrenal glands were rapidly removed by blunt dissection using forceps and scissors and then placed into a drop of cold Locke's solution. Fat, blood and other tissues connected to adrenal glands were carefully removed with fine forceps under visual control using a dissecting microscope, avoiding damage to the glands. Cleaned glands were transferred into another clean drop of Locke's solution and then put into a 15 ml Falcon tube containing 400 μ l of the digestion enzyme treatment solution. The glands were digested for 20 minutes in a shaking water bath at 37°C. The enzyme solution was then replaced by 400 μ l of inactivating solution and incubated 4 minutes in the shaking water bath at 37°C. The inactivating solution was removed and 900 μ l of prewarmed culture medium was added to the glands. The glands were then carefully triturated with a 200 μ l pipetter until the tissue was dissociated. 100 μ l volumes of the resulting cell suspensions were plated to 9 ultraviolet (UV) sterilized coverslips (25 nm No.1001/0025, Assistant, Germany) in six-well plates and were kept in the incubator (37°C, 9% CO₂) for half an hour, after which 3 ml of prewarmed culture medium was added to each well. The cells were kept in culture for 2 days before use.

2.2.3 Setup and protocols

TIRF microscopy

The TIRF workstation consists of an inverted Zeiss (Göttingen, Germany) Axiovert 200 microscope equipped with a Zeiss TIRF-slider and a solid-state laser system (85YCA010; Melles Griot, Carlsbad, CA) emitting at 561 nm. To observe mCherry (excitation maximum about 590nm (Shaner, Steinbach et al. 2005)), a filter set containing an UV-reflecting dual-band dichroic mirror (catalog #F53–563; AHF Analysentechnik, Tübingen, Germany) and an emitter (catalog #F72–419) were introduced. We used the 100×/1.45 NA Fluar (Zeiss) objective for all measurements. The digital images were acquired using an EMCCD camera (Andor iXon^{EM}, Belfast, Northern Ireland) and controlled by software written in house in the LabView programming environment (National Instruments, München, Germany). Pixels were 160 nm x 160 nm. Images were acquired every 100 ms with an exposure time of 75 ms.

Membrane Capacitance Recordings

The capacitance measurements were performed using an EPC-9 patch-clamp amplifier controlled with the “lock-in” extension of PULSE software. The plasma membrane combined with the ions dissolved in the intra- and extracellular solutions behave like a capacitor, with charged particles collecting on the inner and outer surfaces of the cell. This membrane capacitance allows storage of charge that is proportional to the surface area of the cell. The capacitance can be calculated from the currents measured under voltage clamp as follows: a sine wave command potential is applied to the cell. Charge is related to membrane capacitance and potential. The lock-in extension relies on two orthogonal sinusoidal functions and DC current. The magnitude of sinusoidal command voltage applied to the cell is so small that the cell's properties are essentially linear. The responses of these two orthogonal frequencies are a function of the access resistance (R_{access}), the

membrane resistance (R_m) and the cell capacitance (C_m).

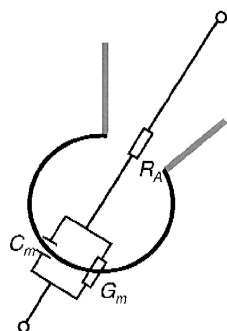


Fig.2.3 Schematic configuration of whole-cell measurement and the equivalent circuit. Black line: cell membrane; gray lines: patch pipette; R_A : access resistance; G_m : membrane conductance; C_m membrane capacitance (Lollike and Lindau 1999).

Assuming that the reversal potential of the DC currents is known and the DC current is known, the unknown parameters can be calculated.

Traditional Whole-cell recordings (Fig.2.3) were carried out with polished, wax-coated pipettes (GB150F-8P, Science products, Germany) with an input resistance of 4– 6 M Ω . An EPC-9 patch-clamp amplifier was used and was controlled by PULSE software (Heka Elektronik, Lambrecht, Germany). Capacitance measurements were performed using the Lindau-Neher technique implemented as the “sine + dc” mode of the “software lock-in” extension of the PULSE software. A 1 kHz, 35 mV amplitude sinusoidal stimulus was superimposed onto a DC holding potential of -70 mV. Data were acquired through a combination of the high time resolution PULSE software (10 kHz, filtered at 2 kHz). Derived capacitance traces were also recorded by “chart recorder” at 1 Hz. After achieving TIRF, Chromaffin cells were stimulated with a train of ten depolarizations to 0 mV, of 100 ms duration at 5 Hz.

Image Recording Protocol 1

After chromaffin cells were cultured for two days, SFV virus was added to cells. Within four hours of SFV virus infection, chromaffin cells were taken out from six-well plate, and placed on the TIRF work station, then slowly perfused with normal extracellular solution. Search NPY-mCherry expression cell under epifluorescence mode, and after finding the target, the laser angle was adjusted manually to TIRF mode. The fluorescent cells were taken 2 min time-elapse TIRF movie. The acquisition speed was 10 Hz and the exposure time was 75 ms.

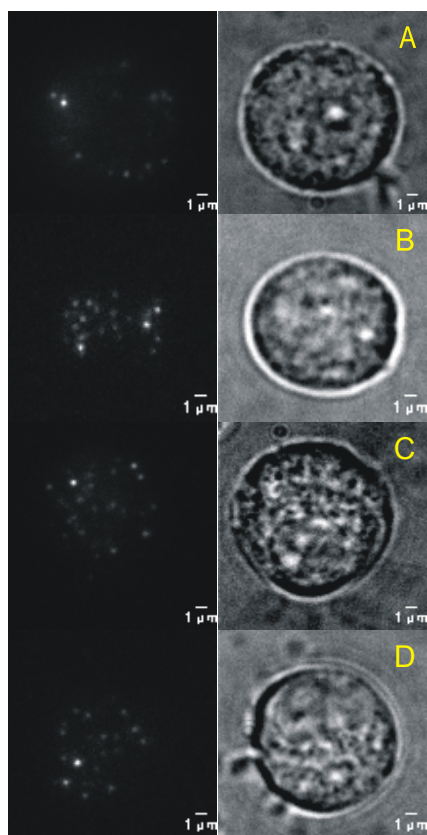
Image Recording Protocol 2

Chromaffin cells were cultured for two days before measurements and then add SFV virus to infect cells. After limited time of infection, cells were removed from six-well plate and settled down on the TIRF setup and then gradually replaced cultured medium with extracellular solution for depolarization experiment. As NPY-mCherry fluorescent cell was observed under epifluorescence mode, manually shift to TIRF mode by changing laser angle. Put polished patch pipette into extracellular solution and until cell and pipette GigaOhm sealing was formed, 2min time-elapse TIRF movie was started at 10 Hz with the exposure time of 75 ms. In order achieve in whole-cell configuration, a gentle suction was applied to cell and following that capacitance recording was started. After the TIRF measurement was done, the priming pool size in cell was tested by a train of depolarizations mentioned above. The TIRF movie contains phases of on-cell /whole-cell configurations.

2.2.4 Time window and analysis for TIRF Microscopy

2.2.4.1 Time window for TIRF

cNNA NPY-mCherry was subcloned into a Semliki Forest virus vector and was used for LDCV labeling in mouse chromaffin cells. However, NPY-mCherry overexpression by viral system resulted in such high numbers of fluorescent granules that tracking was difficult. Vesicle tracking in TIRF is only successful at a low density of fluorescent vesicles, since at high density the tracks may cross and identity of individual vesicles is not clear. In order to achieve a low density of stained vesicles, the cells must be used at a time when few vesicles are fluorescent. The longer the cells are transfected, the more fluorescent vesicles are present. We first determined the optimal time window for the TIRF experiments. mCherry fluorescence after pSFV1-polyL-IRES-NPY-mCherry infection in WT cells was visible under TIRF after 3.5 hours. 120 cells (N=10 pups) were tested from 3.5 to 5 hours at intervals of 0.5 hour (shown in Fig.2.4). A reasonable amount of vesicle staining was observed between 3.5 and 4.5



hours. After 3.5 hours of infection, fewer than 6% of DKO or control cells and among these fluorescent cells, less than 1% still adhered tightly to the coverslip. Adherence is a requirement of TIRF since the evanescent field is very shallow. At 4 hours after infection 14% efficiency was near 14% and an acceptable number of vesicles were stained. This incubation time was optimal for our purpose. Cells were placed on the microscope stage and images were acquired for 2 minutes.

Fig.2.4 Samples of NPY-mCherry-labeled vesicles in the submembrane region with different infection time. Left panel: appearance of footprints acquired in TIRF with NPY-mCherry-labeled granules in wild type cells with infection time of A) 3.5hours B) 4 hours C) 4.5 hours D) 5hours. In the right panel the observed cells are shown with bright field illumination.

2.2.4.2 Single granule trajectory analysis

The algorithm used for single vesicle-tracking was as follows. A raw stack of TIRF images was converted into a set of trajectories as a function of time. The analysis typically starts with noise removal and is followed by vesicle segmentation. The process of segmentation is to partition a digital biological image into a set of pixels (as foreground and a background), with the purpose of identification of the foreground as vesicles and to plot their locations. Trajectories normally can be acquired using a nearest-neighbor algorithm, which assigns a granule from any frame to spatially nearest vesicle in the next frame. The calculated trajectories reveal mobility patterns of vesicles and the dwell time of vesicle in evanescent field can also be derived from this data.

In practice, stacks of acquired images were analyzed using a program written in house (Easy Track-by Dr. Detlef Hof) in LabView (National Instruments, München, Germany). Vesicle tracking was preceded by background subtraction. To segment vesicles, an adaptive threshold was obtained, by comparing fluorescence intensities of three contiguous pixels with pre-defined values.

LDCVs in mouse chromaffin cells are small, normally having an area of 3X3 pixels, with low intensities only 1.1 to 1.2 times above the background noise. The small size and low intensity lead to such small differences in intensity that neighboring objects cannot be reliably distinguished (shown in Fig.2.5). In addition, due to severe halos, the background varies in intensity. For this reason, the threshold method causes errors in vesicle segmentation process. To overcome this problem, the images were 10% high-pass filtered with a fast Fourier transform method and the vesicle segmentation was repeated. Errors were corrected manually by setting the intensities of adjacent object boundaries to zero.

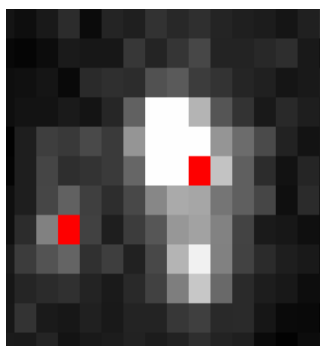


Fig.2.5 Single vesicle identification after background subtraction. The red dots represent the calculated coarse center of the mass. One square represent one pixel. The size of one pixel is 160 nm X 160 nm.

After segmentation, the next step in achieving vesicle tracking is granule association. The coarse centers of vesicles which had moved less than 2 pixels laterally between adjacent frames were linked. Objects which resided in less than three consecutive

frames were excluded, as most of these represented random noise(Lin, Ming et al.; Toonen, Kochubey et al. 2006). The problem of association of vesicles in adjacent frames is further complicated by the fact that the total number of vesicles is not constant, but varies over time due to merging signals, granules leaving the evanescent field and new-comers entering field of view. In addition individual particles cannot be distinguished based on shape or texture since they are smaller than a single pixel.

Use of a nearest-neighbor algorithm of two pixels caused many mismatches, while use of 1 pixel allowed association of granules with fewer errors but caused more fragmentation of the trajectories. The only solution is to merge intermittent trajectories with spatial and temporal tolerances, starting from small gaps of two pixels with three frames, and gradually increasing to five, seven, and ten frames, and then to three pixels starting with three frames and then to five, seven, and ten frames. And all the trajectories were checked manually and saved. Centroid position was refined by calculating 1X1 pixels around a coarse center. To avoid error from artificial boundaries, this process was carried out on raw images after background subtraction.

Vesicle trajectory (Fig.2.6) was analyzed using caging diameter (CD) analysis (Nofal, Becherer et al. 2007). Caging diameter is the maximal distance travelled by the vesicle within a predetermined time window. This window was then shifted one frame at a time until the entire track was analyzed. In my measurements, TIRF stacks were acquired at 10Hz, thus each granule XY position was measured every 100 ms. Within a 1s window, every position was followed by nine continuous positions. The distances covered were measured from the starting position to all the other nine positions, with the highest distance assigned as the CD of that position. The time window was shifted to the next position and the process was repeated. In contrast to 1s time window, A shorter duration sliding window generated a noisy signal with little information, whereas longer windows smoothed the time course of the CD (shown in Fig.3.1). Nofal et al. reported that the CD allowed distinction of three different types of lateral mobility: nearly immobile vesicles, a caged motion, and directed motion. They also found that in bovine chromaffin cells, both docked and primed vesicles display restricted mobility patterns, but the mean CD of primed vesicles is approximately half as large as the mean CD of docked vesicles. Therefore they suggested that primed vesicles can be distinguished from docked vesicles by the CD (Nofal, Becherer et al. 2007). CD was analyzed with IGOR Pro (Wavemetrics, Lake Oswego, OR)

extensions by Dr.Detlef Hof. Data were shown as Mean \pm SEM (Standard Error of Mean).

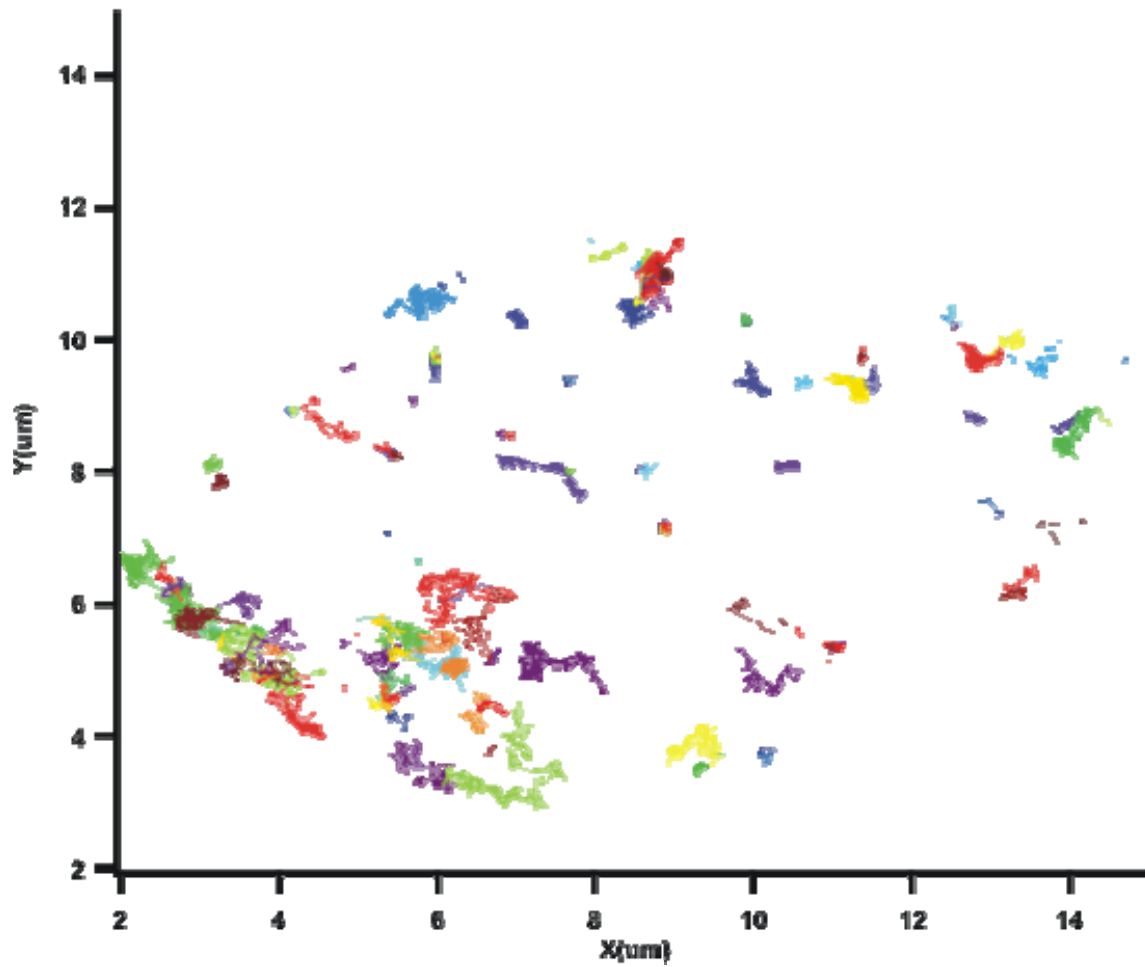


Fig.2.6 Analysis of vesicle trajectory within one syb 2/ cellubrevin null cells labeled by NPY-mCherry. Different trajectory was depicted with different colors.

3. Results and discussion

3.1 Results

Deletion of syb2 does not change docking.

In order to determine if deletion of Syb2 alters docking of LDCVs we examined vesicle mobility prior to fusion, within living cells. To determine mobility we used TIRF images of secretory vesicles labeled with NYP-mCherry in cultured embryonic

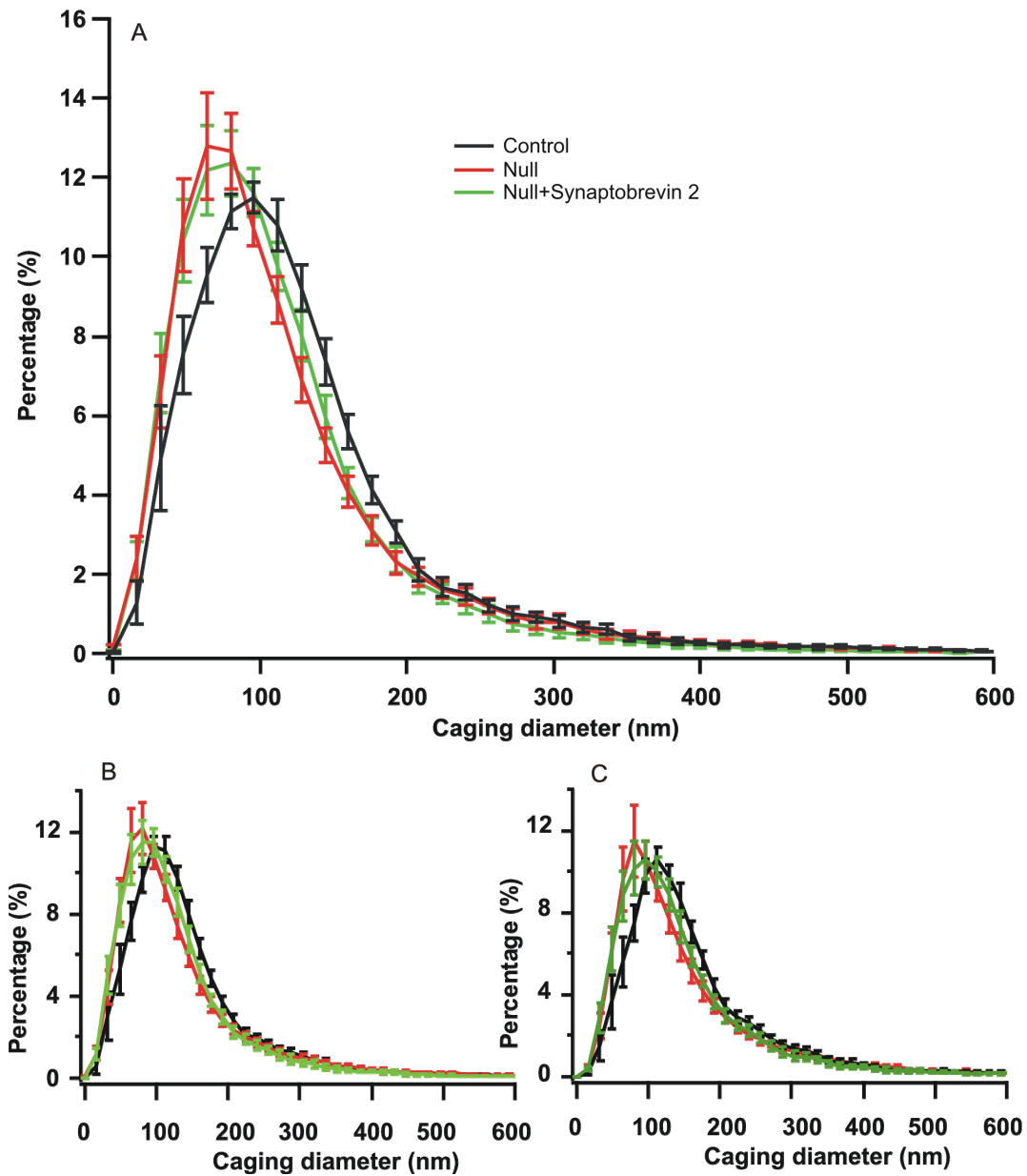


Fig.3.1 Caging diameter histogram with different time windows. Total number of trajectories is n=973 (N=6 cells), n=1068 (N=9 cells), n=1225 (N=10 cells) for control, null, null+syb2 cells. (A)Time window is 1s. (B)Time window is 1.5s. (C)Time window is 2.5s.

chromaffin cells from syb 2/ cellubrevin double knockout (referred to as null cells). Virus infected littermate cellubrevin knock-out cells were used as controls. Null cells also were labeled by overexpression of pSFV1-syb2-IRES-NPY-mCherry. Four hours after infection, cells were perfused with normal extracellular solution and recorded for two min at 10 Hz. We analyzed the movements of LDCVs using caging diameter analysis (see above) which represents a quantitative measure of vesicle mobility. In order to show all analyzed vesicles in one figure, a histogram of normalized CDs with standard error versus time of trajectories is plotted (Fig.3.1).

Surprisingly, there were no observable differences in the CDs for null (DKOs) and in null cells overexpressing syb2. In contrast, the CD histogram was shifted to larger CDs. The distributions of normalized CDs among the three groups were well fit by a single Gaussian function in each group (Fig.3.2), as opposed to the multiple Gaussian distributions reported in bovine chromaffin cells (Nofal, Becherer et al. 2007). The mean of CDs was 82.74 nm, 74.32 nm, 76.11 nm in control, null, null+syb 2 cells, respectively.

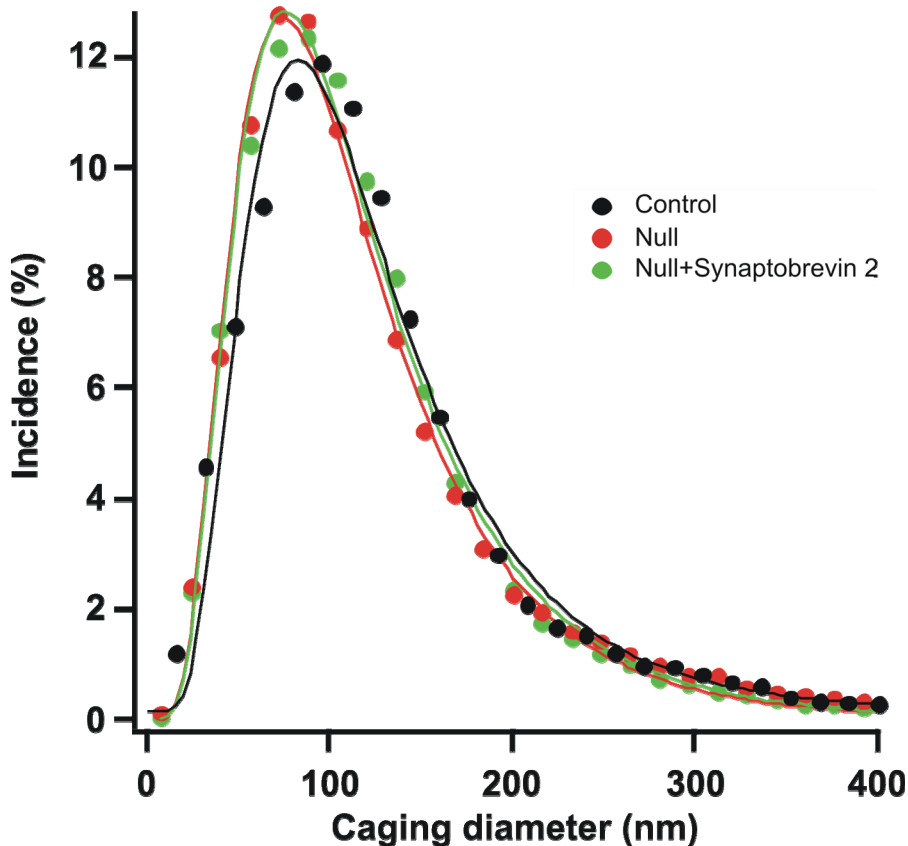


Fig.3.2 the Gaussian fit and normalized distribution of caged diameter (time window is 1s). The measured values are shown as solid dots and the solid lines represent as the Gaussian fit.

A plausible explanation for the presence of only one Gaussian component in our experiment is that the extracellular solution contains high magnesium and low calcium (4 mM MgCl₂, 1 mM CaCl₂) resulting in little induction of secretion in these chromaffin cells. Thus, most of the cells were in resting state with little priming of LDCVs. Within the 160 nm layer illuminated by the evanescent field, secretory vesicles which were detected were defined as docked vesicles. Thus, lack of syb2 does not change docking phenotype in TIRF. This finding was in agreement with an analysis of morphological docking observed in electron micrographs (Borisovska, Zhao et al. 2005).

Priming pools with depolarizing stimuli in null and control cells

To test whether syb2 mediates priming in Ca²⁺-evoked secretion, we patch clamped the cells in the whole cell configuration and depolarized them, a maneuver which rises intracellular calcium to around 500 nM and will drive more vesicles into the primed state. This allowed us to simultaneously measure capacitance changes during the TIRF experiments. Cells were bathed in an extracellular solution containing 2.5 mM CaCl₂ and 1.2 mM MgCl₂. Release-competent vesicles were subsequently depleted by a train of ten 100 ms depolarizations. As described above, such long depolarizations release RRP. In flash photolysis experiments, secretion from syb 2/ cellubrevin null cells was nearly abolished (Borisovska, Zhao et al. 2005). Thus, a very small response to depolarization in null cells (7.22 ± 4.53 fF, n=18) was expected (Fig.3.3). Surprisingly, the estimated RRP size from control cells (22.82 ± 8.28 fF, n=17) was also small and there is no statistical significance between these

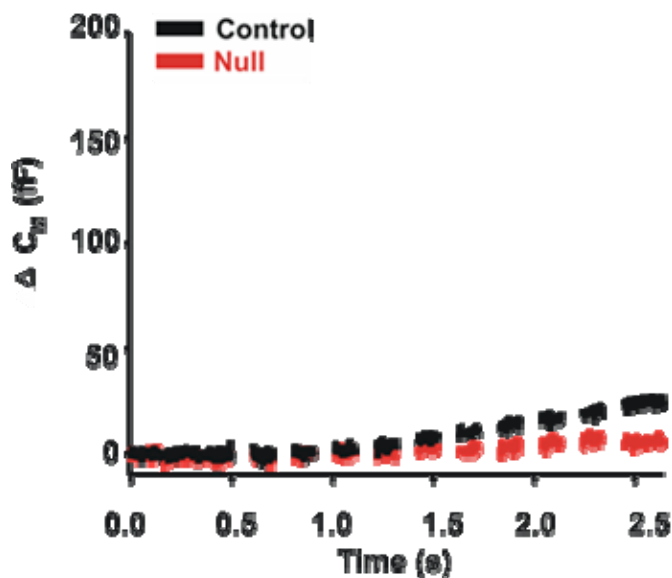


Fig.3.3 Average C_M responses with 502 nM free Ca²⁺ from virus-infected syb2 / cellubrevin null cells and its littermate control labeled by NPY-mCherry .

two group (unpaired Student's test, $p = 0.11$). The lack of a significant enhancement of pool size in the control cells may indicate that the 502 nM free $[Ca^{2+}]_i$ in the intracellular solution induced release prior to the depolarizing stimulus. Support for this proposal came from the observation of spontaneous secretion 128.49 ± 35.14 fF/min in the control cells before depolarizations. And the amplitude of the spontaneous release in null cells was only 33.88 ± 11.74 fF/min.

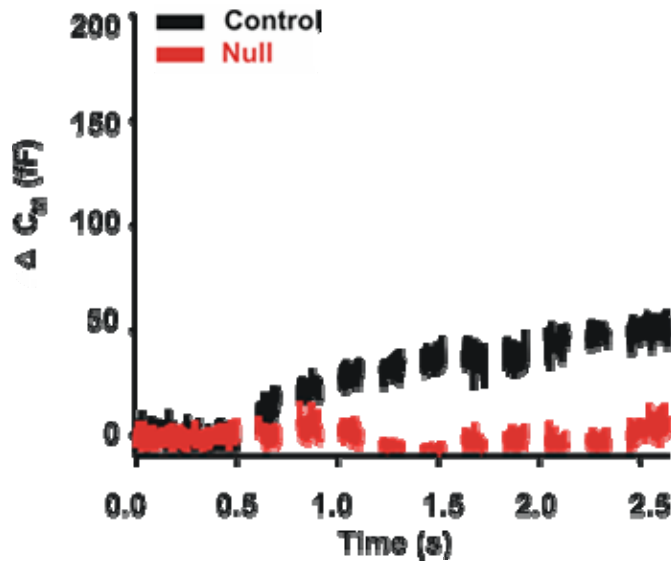


Fig3.4 Average C_M responses with 404 nM free Ca^{2+} from virus-infected syb 2/ cellubrevin null cells and cells from littermate controls labeled with NPY-mCherry .

To test this idea, we used a new intracellular solution with a lower $[Ca^{2+}]_i$. We prepared a pipette solution in which the free intracellular calcium was ~ 404 nM. In experiments in which this intracellular solution was used to patch mouse chromaffin cells, the size of the RRP in infected control cells (46.39 ± 35.60 fF, $n=4$) as depicted in Fig.3.4 was and the response amplitude of the infected syb 2/ cellubrevin null cells

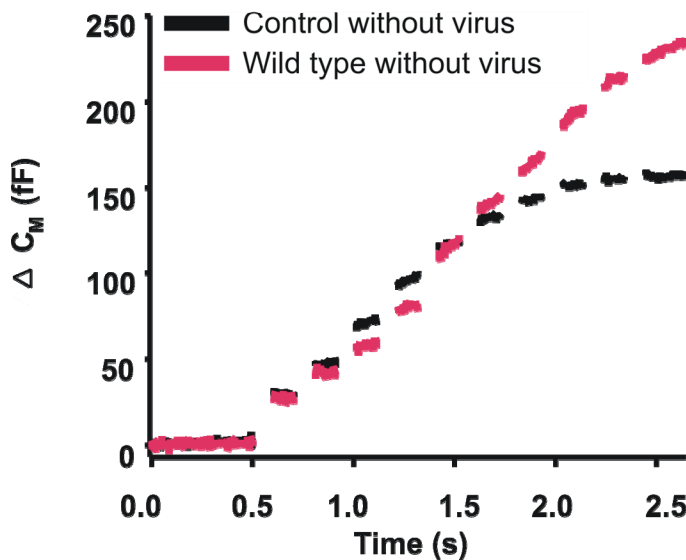


Fig.3.5 Capacitance response (ΔC_m) to a train of 100 ms depolarizations delivered at 5 Hz. Cellubrevin knock-out and wild type cells were measured with 502 nM $[Ca^{2+}]_i$ without virus infection.

was 8.53 ± 7.33 fF (n=3). In addition, in control cells we observed spontaneous release 80.09 ± 73.68 fF/ min and null cell had no spontaneous release. To exclude the possibility that the free intracellular calcium in these two solutions were higher than predicted, we tested the solutions on naïve wild type (WT) cells. In these experiments the 502 nM $[Ca^{2+}]_i$ was able to elicit the expected Ca^{2+} -dependent exocytosis in WT cells (232.10 ± 42.33 fF, n=8, Fig.3.5) with 63.54 ± 15.02 fF/min spontaneous release observed prior to depolarization. Unlike embryonic control cells, WT cells were from new born babies. To rule out that the RRP size was affected by the age of these cells, we performed experiments on cellubrevin knock-out cells without virus as well, with the same solutions (intra- and extracellular) and the same depolarizing pulse. The response from cellubrevin knock-out free of virus infection in Fig.3.5 was 159.15 ± 30.58 fF (n=20) with little spontaneous release (-3.19 ± 19.23 fF/ min).

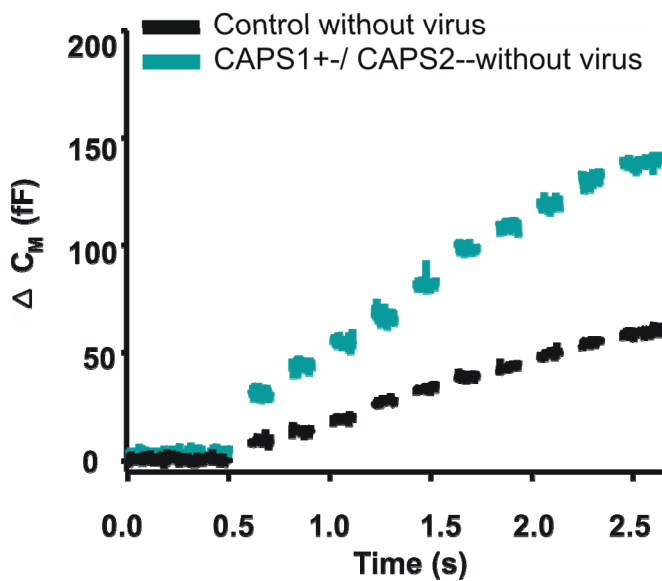


Fig 3.6 Depolarization-induced exocytosis under 404 nM $[Ca^{2+}]_i$ in embryonic hom-ozygous CAPS1 KO cells and cellubrevin knock-out adrenal chromaffin cells.

The 404 nM $[Ca^{2+}]_i$ was tested on cellubrevin knock-out cells and CAPS1 (Ca^{2+} -dependent activator protein for secretion 1) homozygous cells (Fig3.6 shown as CAPS1+/- CAPS2--). Major advantages of CAPS1 homozygous cells are they have the same age (E19) as embryonic cellubrevin and CAPS1 homozygous cells even lack of CAPS2 protein, the RRP size remains unchanged compared to wild type (88.0 ± 20.0 fF) (Speidel, Bruederle et al. 2005). In Fig.3.6 depolarization with CAPS1 homozygous and cellubrevin knock-out, the response were 143.42 ± 22.32 fF (n=10, pre-release -2.17 ± 58.45) and 61.36 ± 28.17 fF (n=9, pre-release 75.55 ± 13.29 fF/min), respectively. The results from Fig.3.5 and 3.6 summarized that both of the

two solutions were able to elicit depolarization-induced exocytosis in WT, WT like cells, cellubrevin knock-out without virus infection. Therefore, cellubrevin knock-out with NPY-mCherry infection had small depolarization-induced response due to long time infection, thus, we shorted the infection time. As exhibited in Fig3.7, infection time was tried between 3 hours when mCherry fluorescence could start to be detected under CCD and 4 hours, and interval time was 10 min, however, under 404 nM (15.17 ± 10.77 fF, n=10) and 502 nM (12.87 ± 12.40 fF, n=5) $[Ca^{2+}]_i$, infected cellubrevin knock-out still had problem to release RRP. This indicated that NPY tagged fluorescent protein lead to cell dying in SFV system since expression started with less than 1% low infection efficiency.

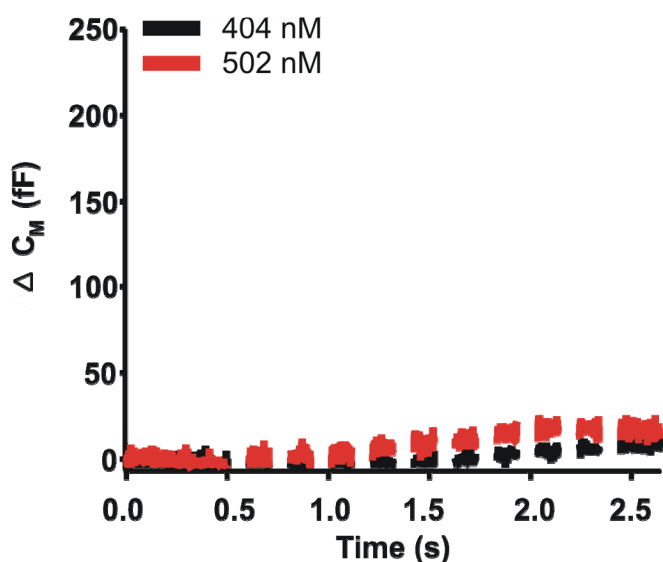


Fig.3.7 Average response of cellubrevin knock-out within various infection time under 404 nM and 502 nM $[Ca^{2+}]_i$ solution.

3.2 Discussion

In the present study, we found that mouse chromaffin cells expressing the NPY-mCherry after SFV viral infection exhibited very small primed pools and secreted very little catecholamine. The cells retain their morphology; however their ability to release LDCVs in response to depolarization was severely reduced. In addition, when compared to cells free from virus, virus- infected cells exhibited larger spontaneous release before depolarization.

1. The SFV construct containing neuropeptide Y is toxic to mouse chromaffin cells

Adrenal chromaffin cells are a popular model cell for study LDCV. Chromaffin cells are small, spherical cells which are well suited to patch clamp experiments. The available evidence supports the idea that the core machinery of LDCV release in

chromaffin cells is similar to that of neurotransmitter release machinery and modulation of secretion in neurons is in many ways similar to that in chromaffin cells. These factors, combined with the morphological simplicity of the adrenal medulla are reasons why catecholamine secretion from chromaffin cells has been intensively studied as a model system for exocytosis.

In 1999, bovine chromaffin cells were first successfully transfected by SFV. Infection with SFV ultimately leads to cell death since the virus takes over the expression machinery of the cell, with viral expression producing up to 20 fold protein expression in infected cells (DiCiommo and Bremner 1998). However, within a reasonable time window, between 12 hours and 36 hours, depending on infection efficiency, the infected cells are still viable and maintain normal resting intracellular calcium, RRP size and refilling kinetics as measured electrophysiologically. After longer infection times, the cells change shape and are difficult to patch (Ashery, Betz et al. 1999).

Secretion can be restored from syb2/cellubrevin double knock-out within 4-6 hours after start of SFV-driven syb2-IRES-GFP protein expression (Borisovska, Zhao et al. 2005). TIRF measurements have been carried out on catecholamine containing granules in bovine chromaffin cells (Rohrbach 2000) and in rat PC12 cells (Lang, Wacker et al. 1997), which were originally isolated from a pheochromocytoma in the adrenal medulla of a rat in 1976 (Greene and Tischler 1976)). TIRF microscopy has rarely been performed on mouse chromaffin cells. My experiments were the first to combine TIRF microscopy with electrophysiological measurements in mouse chromaffin cells. NPY-mCherry had substantial effects on secretion capabilities of chromaffin cells, and in addition, the signal to noise was around 1.1:1. mCherry exhibits potential photobleaching, a serious liability in prolonged TIRF measurements where vesicles should be tracked over time that was observed in monomeric red fluorescent protein (mRFP).

To avoid photobleaching we generated a construct in which NPY cDNA was followed by the cDNA of teal fluorescent protein (TFP). TFP is a very photostable protein, which overcomes the liability of bleaching observed with mRFP. TFP expression was examined under different incubation temperatures (31° and 37° C). Unfortunately, TFP was also inefficient as a marker due to low expression. Ruud has reported TIRM measurement on embryonic mouse chromaffin cell using NPY-Venus introduced by SFV with recordings being carried out between 4 and 8 hours after

infection (Toonen, Kochubey et al. 2006). For this reason, we tested NPY-Venus at a 4 hour transfection time. However, when using 502 nmol free $[Ca^{2+}]_i$ condition, control cells had similar responses (data not shown). Expression of NPY tagged-fluorescent protein leads to early cell death in our cells. In immunostaining assays, syb2 is often used as the vesicle marker. Since syb2 is bound to the vesicle its fluorescence is not rapidly lost upon exocytosis, making it a poor marker for secretion. To address this issue, syb2-IRES-EGFP from Prof. Dieter Bruns was tested as a TIRF marker as well. However the syb2-IRES-EGFP expression resulted in cytosolic fluorescence and is also not suitable for TIRF since individual secretory vesicles were not visible in the evanescent field (data not shown). Thus, for effective TIRF, only marker sequestered in the vesicles as releasable content were useful.

2. Can TIRF detect priming in mouse chromaffin cells?

In bovine chromaffin cells, it was reported that primed vesicles can be distinguished from docked vesicles by a reduced mobility, reflected by a mean of caging diameter of 101 nm, as opposed to that proposed for docked vesicles, which was reported to exhibit a mobility with a mean caging diameter of 220nm (Nofal, Becherer et al. 2007). The typical size of an LDCV in an embryonic mouse chromaffin cells in our video images is 3X3 pixels, and one pixel represents 160 nm with the ratio of signal to noise around 1100: 1000. Under resting conditions, the mean caging diameter was about 80 nm (Fig.3.2), which was interpreted as the caging diameter of the docked state.

If the caging diameter in the primed state in mouse chromaffin cells is about half that of the docking caging diameter, as is the case in bovine cells, it will approach 40 nm, which is one fourth the length of a pixel. Under optimal recording conditions this will be too small to resolve in video and must be calculated. Since the TIRF setup itself was not completely drift- or vibration free, imaging distortions due to temperature-related microscope stage drift or lateral drift correlating to time may have an impact on the measurements of priming caging diameter. Moreover, the accurate detection of caging diameter is dependent on the accurate determination of the centroid position of a single fluorescence source. The precision of the determination of the location of a single emitter can be quite high but this requires that a sufficient number of photons are collected (Rust, Bates et al. 2006). In our system, in contrast to a background 1000, the signal on average was around 1100. Such low signal to noise ratio does not allow accurate determination of the centroid of large dense core

vesicle. Thus, we cannot accurately detect the small changes in XY position associated with such a small caging diameter. The situation could be overcome by a zero-drift system such as the like Olympus IX81 that calibrates the focal plane by internal laser and automatically compensates drift, combined with a CCD with smaller pixel size, provided that photon sensitivity is high enough. In spite of such improvements, it is not clear if the smaller caging diameter is the sine qua non of the primed state. Immobilization is an early and necessary step in the priming process but may be insufficient, as further molecular processes are needed to acquire complete fusion competence. The changes may not translate into changes in vesicle mobility (Yizhar and Ashery 2008). This is likely the major challenge the usage of TIRF to observe priming.

The concept of priming derives from experiments comparing docked and releasable pools. In particular, flash photolysis experiments in which global, stepwise increases in free intracellular calcium, indicate multiple kinetic components of release. Since differences in concentration and rate of rise of calcium are obviated by flash photolysis, these kinetic components appear to arise from differences in the primed pools. Identification of releasable pools demonstrate that most docked vesicles are not fusion competent, which led to the idea that a priming step (achievement of fusion competence) is required.

Unlike docking observed in EM, the primed state is not recognizable until fusion occurs. In spite of significant advances we cannot identify primed vesicles with certainty. Docking and priming appear to be linked at the molecular level with players such as SNARE complex components and munc-18, with the latter being integrally part of both processes, making it difficult to experimentally dissect the process. It is also possible that the differences in mobility will fall outside of the currently available resolution limits, in particular for microscopy of living cells.

4. Introduction

4.1 Lytic granules in Lymphocytes

Lymphocytes occupy a key position in the immune response for humans and most mammals. Lymphocytes differentiate from stem cells in the fetal liver, thymus, and bone marrow, generating two functional categories of cells: peripheral blood lymphocytes (PBL) and lymphocytes of lymphoid tissues such as spleen, thymus, and lymph nodes. In contrast to lymphoid organs, PBLs circulate in the blood throughout the body. Blood contains two large populations of cells: the red cells, which carry oxygen to tissues, and the white cells, which are involved in the elimination of potentially undesirable elements. Among the white blood cells, lymphocyte populations with specific receptors can recognize antigen-presenting cells (APCs) and after being activated, differentiate and produce a clonal population of antigen-specific effector lymphocytes which mediate destruction of harmful organisms or compounds. Depending the receptor population present, lymphocytes divide into five classes: B lymphocytes, T lymphocytes, APCs, Phagocytic cells and Natural killer cells (NK). Following lysis of the erythrocytes with ammonium chloride PBL are extracted from blood by centrifugation (Schwarz, Kummerow et al. 2007). I have studied the lytic granules of cytotoxic T lymphocytes (CTLs, a.k.a CD8⁺ T-cells) a subpopulation of T lymphocytes which includes Helper T lymphocytes and immunoregulatory T lymphocytes. CD8⁺T cells were isolated from PBLs by removing all the other cell types of cell in PBL with the aid of a CD8⁺ Negative Isolation Kit.

4.2 CD8⁺ T-cells

CD8⁺ T-cells (CD8⁺) express T-cell receptors (TCRs) that can recognize specific APCs by the presence of the major histocompatibility complex (MHC)

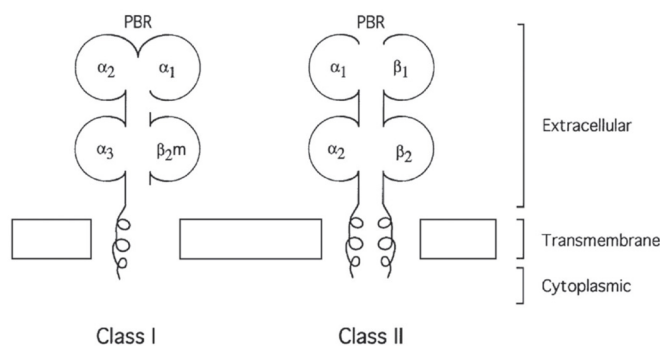


Fig.4.1. Schematic structures of MHC class I and class II molecules. PBR: peptide binding region. (Dukkipati, Blair et al. 2006)

proteins on their surface. In mammalian species MHCs are present on the surface of APCs, and MHC proteins consist of two classes: MHC Class I molecules and MHC class II molecules (shown in Fig.4.1). CD8+ T-cells only recognize antigens presented by a MHC class I-molecule while Helper T lymphocytes (CD4+) bind to MHC class II-presented antigens.

The interface between an APC and a CTL form a tightly sealed junction called an immunological synapse (IS, a.k.a immune synapse). As shown in Fig.4.2, TCR-CD3 complex consists of heterodimeric TCR α and β chains in combination with six CD3 subunits denoted γ , δ , ϵ . The formation of the IS is initiated by TCRs recognition of MHC proteins. Subsequently, surface molecules are redistributed and the cytoskeleton is rearranged. A central supermolecular activation cluster (cSMAC) is formed which is composed of CD4 or CD8, CD3, CD2, CD2-associated protein (CD2AP), CD28, lymphocyte-specific protein tyrosine kinase (LCK), and the θ isoform of protein kinase C (PKC θ), in addition to the TCRs and the MHC proteins. At this time, lymphocyte function-associated antigen-1 (LFA-1) ligated with ICAM-1 and talin forms a ring around the cSMAC, referred to as the peripheral SMAC (pSMAC). Lytic granule docking and fusion takes place in a region adjacent to the cSMAC.

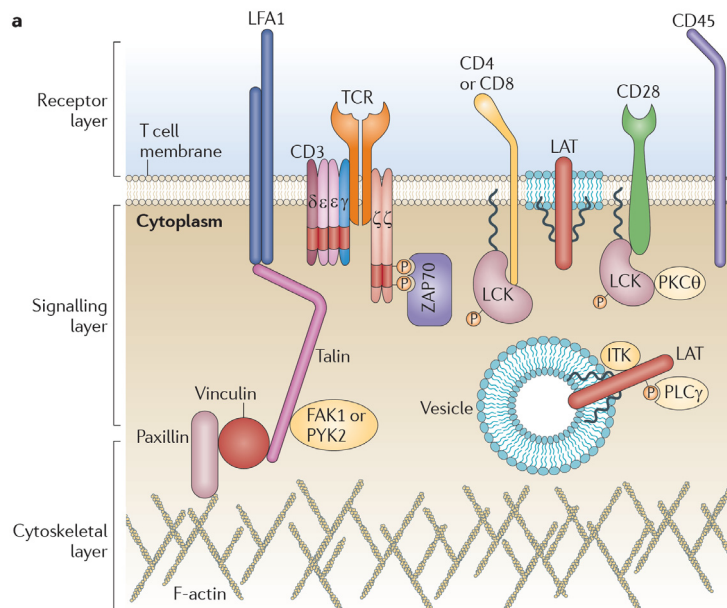


Fig.4.2 The structure of the IS. The receptor layer, the signaling layer and the cytoskeletal layers are shown with their components. The receptor layer components mediate recognition allow stable contact with the target cell, leading to activation and IS generation (Dustin and DePoiil).

T cell contains three layers: outer receptor layer, middle signaling layer, and inner cytoskeletal layer. The receptor layer includes the TCR-CD3 complex, CD4 or CD8, CD28 and LFA1. The signaling layer contains LCK, ζ -chain-associated protein kinase of 70 kDa (ZAP70), IL-2-inducible T cell kinase (ITK), phospholipase C γ (PLC γ) and

PKC θ . The cytoskeletal layer possesses filamentous actin (F-actin), talin, paxillin, vinculin and focal adhesion kinase 1 (FAK1) or proline-rich tyrosine kinase 2 (PYK2). The adaptor protein linker for activation of T cells (LAT) is attached to the plasma membrane and anchored to sub-synaptic vesicles as well. (Dustin and Depoil)

4.3 T-Cell mediated killing

Two independent mechanisms account for lymphocyte-mediated killing: the perforin / granzyme-mediated pathway and the ligand Fas-mediated pathway (Kagi, Ledermann et al. 1996). Both pathways exist in mouse CD4⁺ and CD8⁺ T cells (Ju, Cui et al. 1994; Williams and Engelhard 1996) as well as in human CD4⁺ T cells (Yasukawa, Ohminami et al. 1999). However, it was suggested that the perforin / granzyme pathway dominates the MHC class I elimination pathway (Schulz, Schuurman et al. 1995) and plays only a minor role in the MHC class II elimination pathway (Graubert, DiPersio et al. 1997). CTLs contain lytic granules that secrete their contents during the interaction with APC. During this process, the granule contents, including the lethal pore-forming protein, perforin, which is a single polypeptide of approximately 66 kDa (Masson and Tschopp 1985), as well as granzymes, a family of serine esterases, are delivered to the IS and mediate target cell killing (Peters, Borst et al. 1991). Granzymes are a family of highly conserved serine proteases found in both humans and rodents, located in three clusters on separate chromosomes (Grossman, Revell et al. 2003). Five granzymes A, B, H, K, M are found on humans and granzymes A, B, H, K are present on CTLs. Among these five genes, the most extensively studied is granzyme B. It was reported that approximately half of CTLs coexpressed both granzymes A and B (Grossman, Verbsky et al. 2004), although granzymes A and B are both found extracellularly in human plasma, granzyme A levels are generally higher than those of granzyme B (Buzza and Bird 2006).

Within the lytic granule, at the ambient pH of 5.2, granzyme and perforin form complexes with chondroitin sulfate A which prevents lytic protein-mediated damage to host cells (Masson, Peters et al. 1990). Based on sequence alignment, the central portion of perforin shares some similarity with components of the complement membrane attack complex C9 (Shinkai, Takio et al. 1988) and the C terminus of perforin may form a calcium-dependent membrane-binding C2 domain (Voskoboinik, Thia et al. 2005). Perforin binds to target membrane in the presence of Ca²⁺, and polymerizes to form transmembrane channels (Young, Cohn et al. 1986). It has been

suggested that granzymes pass into the target cell cytoplasm by traversing plasma membrane channels formed by perforin. However these channels, are too small (16 nm diameter) to function as an entry portal for granzymes (Browne, Blink et al. 1999). An alternative explanation is that perforin induces a transient Ca^{2+} flux in the target cell, which triggers a process to repair the damaged cell membrane. As a consequence, both perforin and granzymes enter enlarged endosomes called 'gigantosomes' via merging of smaller lysosomes and are endocytosed (Thiery, Keefe et al.). In addition, perforin itself was not capable of causing target cell apoptosis (Duke, Persechini et al. 1989) unless granzymes were also present (Shi, Kraut et al. 1992). It appears that granzyme B can enter the cytoplasm of cells autonomously but cannot enter the nucleus. Thus, perforin may initiate the apoptotic process allowing the entry of granzyme B into the nucleus (Shi, Mai et al. 1997). Murine Granzyme B cleaves substrate proteins C-terminal to an aspartic acid residue (Otake, Kam et al. 1991) and granzyme B can activate procaspase 3 as well (Metkar, Wang et al. 2003). It is widely believed that granzyme B kills target cells by activating caspases, which then cause the cleavage of additional apoptotic substrates that lead to DNA fragmentation and apoptosis.

Two fusion modes were observed by natural killer cells: complete fusion, characterized by loss of granule content and rapid diffusion at the plasma membrane; and incomplete fusion, characterized by transient fusion pore opening and retention at the fusion site (Liu, Martina et al.).

In order to observe lytic granule exocytosis in my project, the granule content must be labeled by a fluorescent tag. The high concentration of granule content makes these molecules logical targets as granule markers and release of granzymes or perforin allow confirmation of fusion. Both granzymes A or B and perforin were good candidates but overexpression of perforin is more toxic to the CTLs than is granzyme in our measuring system. We used granzyme B as a lytic granule marker in our experiments since it is more prevalent than granzyme A in human CTLs.

4.4 Ca^{2+} and CRAC channels

Calcium ions function as a universal second messenger in virtually all eukaryotic cells, including cells of the immune system which participate in the regulation of cell differentiation, gene transcription and effector functions (Feske 2007). The only Ca^{2+} -selective ion channels present in T cells are ORAI/ORAI combination channels (Kummerow, Junker et al. 2009) termed Ca^{2+} release-activated

Ca²⁺ channel(CRAC). Two STIM proteins and three ORAI channels have been found in humans and mice and different STIM/ORAI combinations form CRAC channels when expressed heterologously, however the major combination is STIM1/ ORAI 1(Qu, Al-Ansary et al.). CRACM1(also known as Orai1) is located in the plasma membrane and STIM1 resides in the endoplasmic reticulum (ER) (Lis, Peinelt et al. 2007), with an EF hand motif near the amino terminus located in the lumen of the ER or outside the cell(Zhang, Yu et al. 2005). As shown in Fig.4.3, the Ca²⁺ influx in T cells proceeds as follows: upon TCR activation, the Src kinases Fyn and Lck phosphorylate tyrosine residues of the ζ-chain-associated protein of 70 kDa (ZAP-70). Once so activated, ZAP-70 phosphorylates the adapter protein linker for activation of T cells (LAT) and Src homology 2 domain-containing leukocyte phosphoprotein of 76 kDa (SLP76), which activate phospholipase Cγ (PLCγ) through the Src-like tyrosine kinase Tec. PLCγ cleaves phosphatidylinositol-4,5-bisphosphate (PtdIns(4,5)P₂) and produces the second messengers inositol-1,4,5-trisphosphate (IP₃ or InsP₃) and

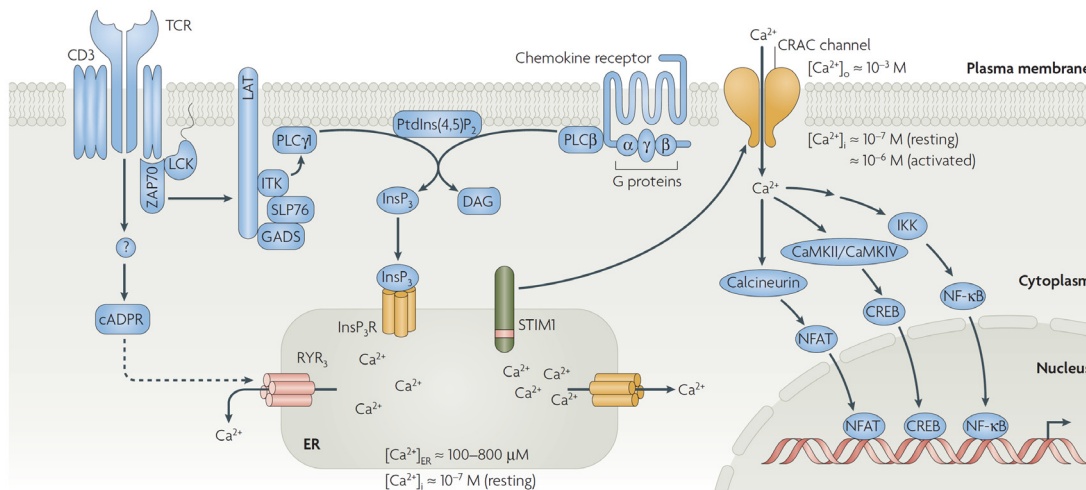


Fig.4.3 Store-operated calcium entry in T cells. At resting state, a Ca²⁺ concentration gradient exists between the cytoplasm and the extracellular space, as well as between the cytoplasm and the lumen of the ER in T cells. The intracellular Ca²⁺ concentrations in resting T cell is kept ~100 nM and after TCR stimulation calcium elevates to ~1 μM via CRAC channel. CRAC channel opening follows procedure described as: antigen binding to the TCR leads to the activation of LCK and ZAP70, which initiate phosphorylation of SLP76 and LAT. This results in the recruitment and activation of ITK (interleukin 2-inducible T cell kinase) and PLCγ1. Similarly, recognition of G protein-coupled chemokine receptors results in the activation of PLCβ. PLCβ and PLCγ1 catalyse the hydrolysis of PtdIns(4,5)P₂ to IP₃(a.k.a InsP₃) and DAG. IP₃ recognizes IP₃ receptors (InsP₃Rs) which resides in the ER membrane, resulting in Ca²⁺ release from intracellular Ca²⁺ stores. The depletion of ER Ca²⁺ store is sensed by STIM1, which forms CRAC channels in the plasma membrane. After Ca²⁺ influx transcription factors NFAT (nuclear factor of activated T cells), CREB (cyclic-AMP responsive-element-binding protein) and NF-κB (nuclear factor-κB) were activated by calcineurin, calmodulin-dependent kinase (CaMK), inhibitor of NF-κB kinase (IKK), respectively. (Figure from (Feske 2007))

diacylglycerol (DAG). IP3 binds to the IP3 receptor in the membrane of ER and initiates release of its stored Ca^{2+} (Kummerow, Junker et al. 2009). Following ER Ca^{2+} store depletion, Ca^{2+} unbinds from the EF hand STIM1. This triggers STIM1 to oligomerize and then to translocate to the plasma membrane where it activates Orai1 to oligomerize and to form CRAC channels (Cahalan and Chandy 2009).

Calcium plays a crucial role in CTLs. However, it is still controversial whether lytic granule release per se, is Ca^{2+} -dependent. Adam Zweifach and coworkers reported that the Ca^{2+} -dependence of target cell lysis is not necessarily due to Ca^{2+} -dependence of lytic granule release. A number of reasons for the apparent calcium dependence of killing are known. First, the formation of IS requires divalent cations but not Ca^{2+} specifically. Second, the granule/ microtubule-organizing center (MTOC) polarization towards the synapse requires Ca^{2+} influx. Finally, the assembly of functional perforin pores also requires extracellular Ca^{2+} . Therefore, a reduction in target cell killing in the absence of Ca^{2+} influx cannot automatically be attributed to effects on lytic granule release (Pores-Fernando and Zweifach 2009)

4.5 The aim of my work

Lytic granules play an important role in mechanism of CTL killing. A variety of other granule-like organelles are present and a variety of granule types have been observed in electron micrographs of T-cells, some of which may be maturing lytic granules. There are also many more granules such as lysosomes and endosomes present than lytic granules. Thus it is not clear which of these granules represent the actual releasable lytic granule form. Thus it would be very helpful to identify the mature form of the lytic granule. We set out to identify lytic granules fusion events in TIRF and to measure the capacitance increases associated with their fusion, which will allow us to estimate the size of these granules.

Much is known about the process of activation of T cells and source and role of increases in intracellular calcium in the process of killing. More than two decades of intensive research focused on the ion channels in immune cells have clearly demonstrated that activation of T cells is associated with release of intracellular stores and is followed by activation of store operated "capacitative" calcium entry leading to sustained increases in intracellular calcium which are required for successful activation of T cells. We will use artificially activated T cells maintained in a medium with low extracellular calcium, which blocks the final steps of activation and

prevents lytic granule release. These cells will be patch clamped in the whole cell configuration with pipettes containing $\sim 2 \mu\text{M}$ free calcium.

The introduction of calcium following breakin and establishment of the whole cell configuration will trigger the final steps in the killing process. As soon as the whole cell configuration is established we will begin TIRF recording and whole cell capacitance recording to correlate the capacitance jumps associated with granule secretion with lytic granule release observed in TIRF.

In order to achieve this goal, we first established the methods that allow us to patch human CTL and simultaneously observe labeled lytic granules under TIRF microscopy. From this combined approach, we can estimate the sizes of identified lytic granule release events. In addition, ion concentration in the intracellular solution could be manipulated via patch pipette into cell. These results will allow us to predict the diameter of lytic granules observed in EM and to compare the size distributions of lytic granule and other types of granules in T cells.

5. Materials and Methods

5.1 Materials

5.1.1 Reagents

Name of product	Catalog number	Company provider
Albumin, from Bovine serum	A9418-100G	Sigma
AIM-V® Medium	12055-091	gibco®
Amaxa™ Human T Cell Nucleofector™ Kit	VPA-1002	Lonza
BioSource™ Recombinant Human Interleukin-2 (IL-2)	PHC0021	Invitrogen
DPBS Dulbecco's Phosphate Buffer Saline 1X	14190-094	gibco®
Dynabeads® Untouched™ Human CD8 T Cells	113.48D	Invitrogen
Dynabeads® Human T-Activator CD3/CD28	11132D	Invitrogen
DynaMag™-15 Magnetic Particle Concentrator	123.01D	Invitrogen
FCS		Invitrogen
HPLC		Merck
Mouse Anti-Human CD3, Clone B-B11, monoclonal antibody	854.010.000	cellsciences
Poly-L-ornithine hydrobromide	P3655-50MG	Sigma
Purified NA/LE Mouse Anti-Human CD28	555725	BD Bioscience
Recombinant Human IL-2 Lyophilized	PHC0021	Invitrogen
Sigmacote		Sigma

Tetraspeck™ microspheres	38784A	Molecular Probes®
0.2 µm diameter		
Tpypan blue solution 0.4%	T8154	Sigma

5.1.2 Solution

Buffer 1:

Mix 500ml DPBS Dulbecco's Phosphate Buffer Saline 1X with 2.5g Albumin, from Bovine serum, sterile, and then store at 4°C.

Solution 2:

Add 50ml FCS to 500ml AIM-V® Medium, then filter under sterile bench. Store at 4°C.

Solution 3:

To regain full activity, lyophilized human IL-2 should be reconstituted in 100 mM acetic acid to 0.5 µg/µl. Stock solutions are filtered and apportioned into 6 µl aliquots. Stored at -20°C.

Solution4:

6µl Human IL-2 dilute with 54µl solution 2. Store at 4°C for one week.

Solution5:

Put Poly-L-ornithine hydrobromide powder in HPLC water, make sure the final concentration is 1mg/ml. Store at 4°C.

Solution6:

1mg/ml Poly-L-ornithine dilute with distilled water to 0.1mg/ml.

Solution7:

Human CD3 and CD28 antibody was dissolved into HPBS, the final concentration was 30 µg/ml and 90 µg/ml, respectively.

Normail zero Ca²⁺ Extracellular solution

5 mM	HEPES
4.5 mM	KCl
3 mM	MgCl ₂
155 mM	NaCl
pH 7.4	

Intracellular solution

5.9 mM	CsEGTA
40 mM	HEPES
120 mM	Glutamic-acid
5.4 mM	CaCl ₂
0.3 mM	Na ₂ GTP
2 mM	MgATP
pH 7.3, ~307 mOsm	
Free Ca ²⁺ 2μM	

5.1.3 Human GranzymeB-mCherry cDNA construct

GranzymeB was amplified from human cDNA with primers: 5'-TAT ACT CGA GCC ACC ATG CAA CCA ATC CTG CTT CTG-3' and 5'-ATA TAT CCG CGG GTA GCG TTT CAT GGT TTT CTT T-3' to add XhoI and SacII restriction sites at each end. The mCherry construct was a gift from Prof. Roger Tsien. After digestion with XhoI and SacII, GranzymeB was ligated to vectors containing fluorescent tags, TFP-N1 and mCherry-N1 at the C terminal end of GranzymeB and then purified.

5.1.4 Isolation human CD8+ from PBL

PBL cells are kindly provided by Prof. Markus Hoth. We use the Dynabeads® Untouched™ Human CD8 T Cell kit to isolate the CD8+ cells. This is a negative isolation in which B cells, NK cells, monocytes, dendritic cells, CD4+ T cells and granulocytes are removed from PBLs. The kit contains an Antibody Mix, and Depletion MyOne SA Dynabeads. The procedure is described below:

1. Thaw heat inactivated FCS at RT.
2. Prepare ice box, and put Buffer 1 on ice.
3. Centrifuge PBLs at 200 x g for 8 min at 4°C or RT without brake.
4. Discard the supernatant, and resuspend 100 Mi PBL in 1ml Buffer 1, then add 200μl FCS and 200 μl and mix.
5. Add 200μl Antibody Mix.
6. Rotated by ReaX2 Heidolph at 20 rpm for 20 min at 4°C.
7. Wash the cells by adding 20ml cold Buffer 1. Mix gently by tilting the tube several times and centrifuge at 350 x g for 8 min at 4°C.

During the waiting time, wash the Depletion MyOne SA Dynabeads. First, beads are resuspended and then 1ml of the beads is added to a 15ml falcon and mixed

well with the same volume of Buffer 1. The falcon is placed in the DynaMag™-15 Magnetic Particle Concentrator for 6 min. The fluid is removed using a pipette and then 1ml of Buffer 1 is added.

Remove the falcon tube from the magnet, triturate and store on ice.

8. Discard the supernatant, and resuspend the cells in 1ml Buffer 1.

9. Add 1ml prewashed beads.

10. Rotate on the ReaX2 Heidolph at 20 rpm for 18 min at RT.

11. Using a 1000 µl pipette, triturate the beads and bound cells gently 10 times.

Add 10ml Buffer 1, and place in magnet for 6 min.

12. Transfer the supernatant containing the untouched human CD8+ T cells, to a new 15 ml falcon.

The falcon with beads, resuspend with 10 ml Buffer 1. Put in magnet for 6 min.

13. Repeat step 12.

14. In order to remove residual beads, put the two new falcons in the magnet for 10 min.

15. Transfer the supernatant to fresh tube, and combine the two supernatants and mix thoroughly.

16. Take 20 µl cell suspension, mix with 20 µl Trypan blue solution 0.4% in 1.5 ml tube. Count the cell number. The rest of cells centrifuge at 200 x g for 8 min at 4°C.

17. Warm Solution 2 to 37°C in a water bath.

18. Calculate the required Dynabeads® Human T-Activator CD3/CD28 beads and the Solution volume needed. The ratio of cell to activator bead is 0.7 and the cell density is 1.5Mi /ml.

19. Wash the beads with 1ml Solution 2, place in the magnet for 2 min. Remove the supernatant, and mix with some Solution 2 and then add the Dynabeads® Human T-Activator.

20. Discard the supernatant. Resuspend cells in Solution 2 .

21. Add the prewashed activator beads to cell suspension. Mix completely.

22. Place the cells in a six-well plate.

23. Incubate at 37°C, 5% CO₂ for 2 days.

5.1.5 Electroporate bead-stimulated human CD8+ cells.

Amata™ Human T Cell Nucleofector™ Kits is provided by Lonza. Each kit holds

Human T Cell Nucleofector™ Solution, Certified cuvettes, and Plastic pipettes. The protocol follows as:

1. Add 2ml Solution 2 to 24-well plate. And preincubate in the incubator before transfection to equilibrate CO₂.
2. Take Human T Cell Nucleofector™ Solution out of 4°C. Place at RT.
3. Warm Buffer 1 at 37°C water bath.
4. Collect the cells from six-well plate into 15ml falcon.
5. Place the tube in DynaMag™-15 Magnetic Particle Concentrator for 6 min.
6. Transfer the supernatant into new falcon.
7. Centrifuge at low speed 100 x g for 8 min at RT.
8. Throw away the supernatant.
9. Resuspend 5 million human CD8+ cells in 5ml prewarm Buffer 1.
10. To deplete the residual beads, place the cell suspend in magnet for 6 min.
11. Repeat step 6 and 7.
12. Discard the supernatant.
13. Resuspend 5 million human CD8+ cells by 101 µl prewarm Human T Cell Nucleofector™ Solution.
14. Add 1µg GranzymeB-mCherry. Mix.
15. Open Plastic pipettes, and absorb some prewarm Solution 2.
16. Transfer cell suspension to certified cuvettes. Check no air bubble.
17. Put in Amaxa Nucleofacter™ II and choose program T-023.
18. After transfection, take the cells out with Plastic pipettes. Avoid traturation and air bubble. Cells are very vulnerable after eletroporation. Be careful!
19. Add the cells to the well with preincubated Solution 2.
20. 6 hours later, gather the cells into tube.
21. The dead cells will be removed by centrifuge 100 x g for 8 min at RT.
22. Warm Solution 2 at 37°C water bath.
23. Prepare solution 4.
24. Discard the supernatant. Gently resuspend in 1ml fresh warm Solution 2.
25. Transfer to 24-well plate. Add 1ml more warm Solution 2.
26. Add 2 µl solution 4 to 2 ml cell suspension.
27. After 12 hours, cells are ready for measurements.

5.2 Methods

5.2.1 TIRF images

The TIRF setup has been described previously in detail in chapter 2 (2.2.3 Setup and protocols) with the following modifications: the acquisition speed is set to 10 Hz and the exposure time is 75 ms. All stacks are acquired for 8 min at RT.

5.2.2 Membrane Capacitance Recordings

The patch clamp setup is as described above. For patch clamping T-Cells, traditional whole-cell recordings are carried out using pipettes whose tips were dipped in SIGMACOTE (GB150F-8P glass was used, Science products, Germany) with an input resistance of 2.5–3.5 MOhm. SIGMACOTE is a clear, colorless solution of a chlorinated organopolysiloxane in heptane, which produces a neutral, hydrophobic, thin film on glass (Sigma). The film repels water, retards the clotting of blood or plasma and prevents adsorption of many basic proteins and helps gigaohm sealing.

Positive pressure is applied to the patch pipette prior to bath entry and this pressure is held constant until the pipette tip contact the cell. Then the pressure is released and sealing begins. Sealing is achieved in the whole cell mode with a negative voltage, which facilitates sealing. For high-resolution capacitance measurements, a 1 kHz sine wave was used with an amplitude of 50 mV r.m.s. (root mean square) to improve the signal-to-noise ratio (Hartmann, Scepek et al. 1995). After attainment of whole-cell configuration, a holding potential of -70 mV is applied. Data were acquired at 10 kHz in PULSE software. When the phase of the lock-in is set to the correct phase angle where changes in membrane capacitance (C_m) and access resistance (R_s) are well separated, one of the lock-in channels directly indicates the capacitance changes (Hartmann, Scepek et al. 1995).

In order to synchronize TIRF and voltage-clamp measurements in time, the Andor camera trigger signal was recorded by the EPC9. Capacitance data and triggers were acquired as a single continuous segment to avoid gaps in the sweep which would generate timing errors. The data was temporarily stored in a continuous buffer before being written to hard disk.

5.2.3 The description of the combination experiments

A clean 25mm coverslip was coated at the center with 100 μ l 0.1mg/ml polyornithine at RT for 30 min. Excess polyornithine was removed with the aid of suction, and

antibodies against human CD3 and CD28 were applied. The coverslip was then incubated at 37 °C for 2 hours. 60 μ l cell suspensions were added to the center of the dish. The cells are set aside for 5 min to allow artificial IS formation on the coverslip at RT. In this step, the dish should be free of movement or vibration. Treated cells on the coverslips are then placed in a recording chamber and placed on the microscope stage and slowly perfused with nominal zero Ca^{2+} extracellular solution.

The foot print of a cell in TIRF is located and the cells are patched. After a gigaohm sealing is formed, a TIRF stack acquisition is started and immediately thereafter, breakin to attain whole-cell is carried out. If successful, the capacitance record acquisition is started. In parallel to capacitance recording, CCD recording is carried out at 10 Hz (100 ms): during 75ms exposure time, voltage increases to 5mV, in contrast to the remaining time in the 100 ms loop, when the voltage drops to 0 mV (shown in Fig.5.1C).

5.2.4 Capacitance increment analysis

A single lytic granule was selected as a region of interest (ROI) in Image J. The average fluorescent intensities of ROI was calculated by the Time Series Analyzer plugin in Image J. Average fluorescent intensities versus TIRF time which was shown in frame number of the time lapse TIRF movie was plotted in Igor Pro 6 (Wavemetrics, Lake Oswego, OR). A rapid decrease in fluorescence intensity indicates a fusion event (Fig.5.1B).

The obtained patch clamp data were analyzed using IGOR Pro. The TIRF movie acquisition was continuous and began prior to the capacitance record. The last frame of the stack was located as the last trigger mark in the pulse record voltage trace recorded simultaneously to the capacitance trace. This allowed accurate correlation of time between the imaging and capacitance traces. Fig.5.1C shows the trigger output of the CCD camera recorded in pulse. The time trace in the TIRF movie is calculated from the last trigger mark. In order to improve accuracy of measurement of capacitance steps, the traces were filtered to suppress high frequency noise. The signal can be detected as small as 1.5 fF in whole-cell configuration. The capacitance increment (ΔC_m) were visible in the traces but their amplitude was determined by averaging the 60 points immediately before and after the capacitance step and taking the difference of the averages as the step amplitude. However, the ratio of ΔC_m to whole-cell membrane capacitance (C_m) was less than 1:1500. The step size was determined by the differences of these two average values.

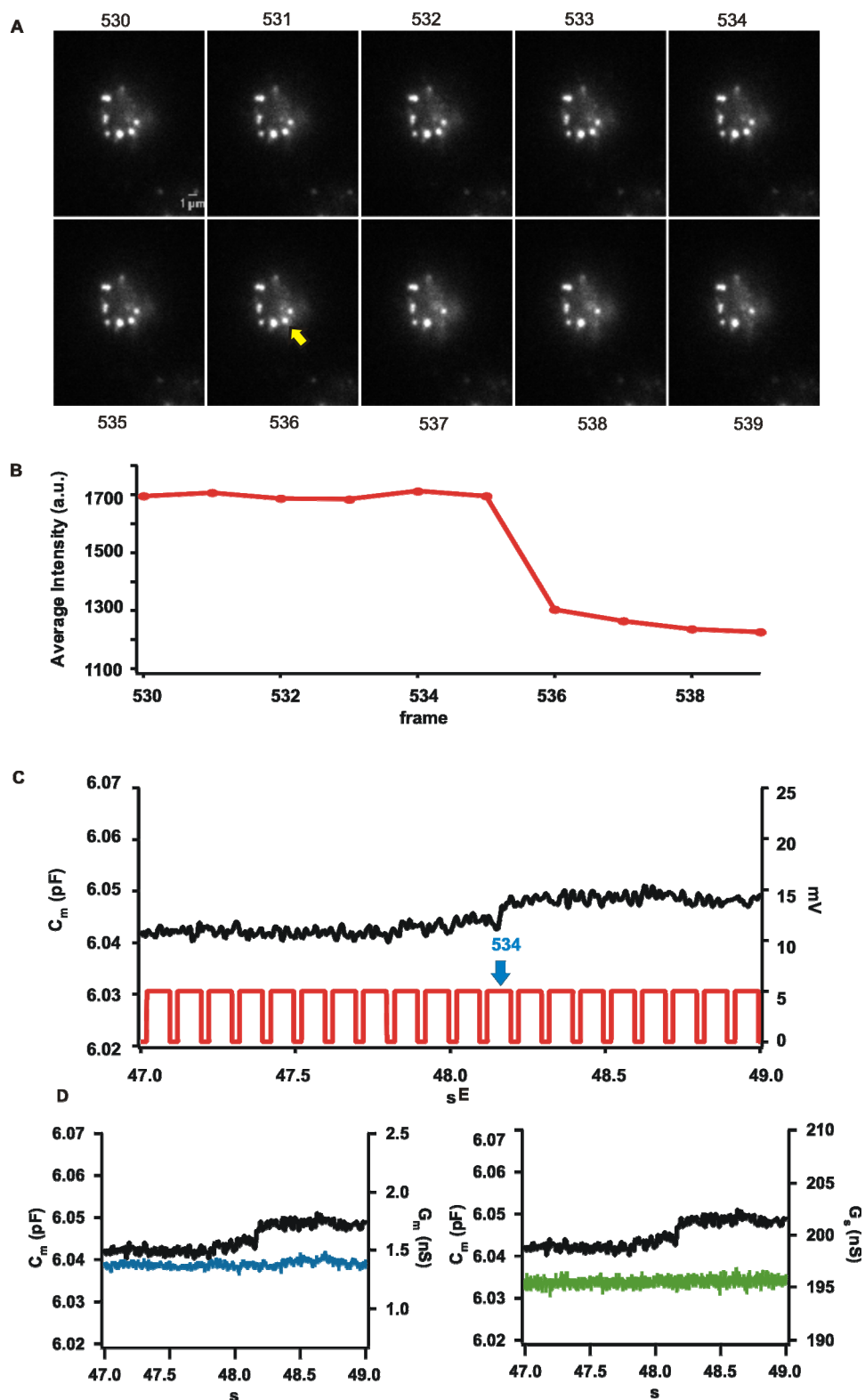


Fig.5.1 Fusion of a granzyme B-mCherry lytic granule with the plasma membrane. (A) Selected frames from a time-lapsed live TIRF imaging are shown. Sequential frame number are marked above or below the images are. The yellow arrow indicates a fusing lytic granule. (B) The fluorescent intensity of ROI where the arrow-indicated granule fused was plotted over time. (arbitrary units) (C) Left axial: whole-cell membrane capacitance (C_m), and C_m plotted in black trace. Right axial: TIRF voltage. TIRF voltage trace was represented in red

trace. As CCD was in 75 ms expose state, voltage increases sharply to 5 mV, in contrast, the voltage drops to 0 mV during non-exposure time. Bottom: recording time in patching. The yellow arrow shows the 536th frame from (A) in patch time axial. (D)(E) C_m (black) was plotted with G_m (blue) and G_s (green), the reciprocal of the cell input resistance and of the access resistance, respectively.

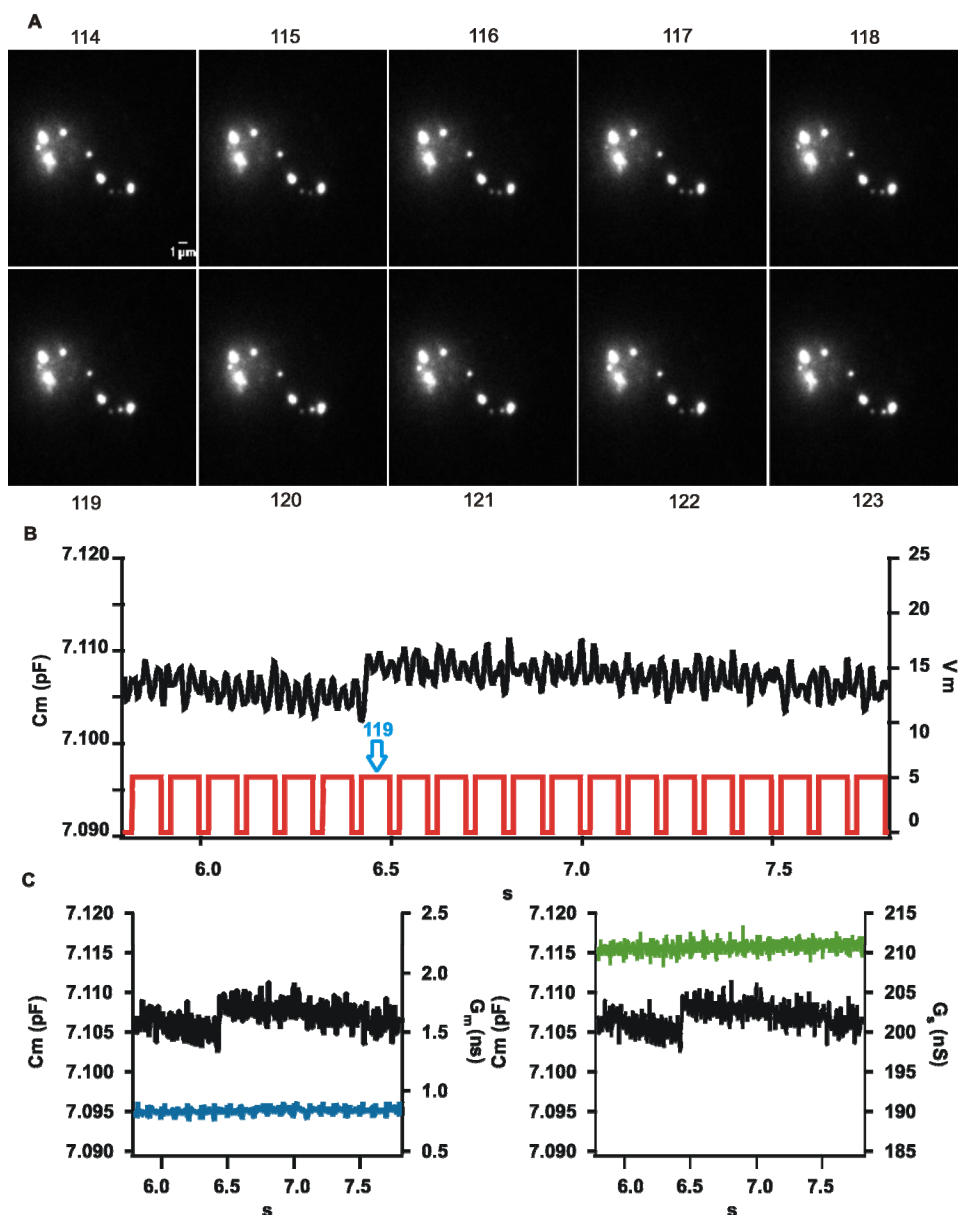


Fig.5.2 Capacitance increment which are not caused by lytic granule release. (A) Parts of TIRF stack are shown with frame number marked above or below the continuous images. (B) Left axial: whole-cell membrane capacitance (C_m), which is plotted in black trace. Right axial: TIRF voltage trace, present in red. The blue arrow shows the 119th frame from (A) in patch time axial. (C) Black trace of C_m as plotted in function of time with G_m in blue and G_s shown in green, the reciprocal of the cell input resistance and of the access resistance, respectively.

To rule out an artifactual ΔC_m which can be caused by instabilities of cell membrane conductance (G_m) and/or access conductance (G_s), potential granule exocytotic

events in C_m were verified by confirming that they were not associated with simultaneous changes in either G_m or G_s or both. Such a comparison is shown in Fig.5.1 in which C_m is shown plotted with G_m and G_s (Fig.5.1D, E). This confirms that the increase in C_m is the result of a fusion event while the TIRF record confirms that fusion of a lytic granule took place.

The distribution of ΔC_m and of the latency of the fusion times after the beginning of Ca^{2+} perfusion into the CTLs via pipette (after establishment of the whole cell mode) were analyzed. The frequency of capacitance event amplitudes and fusion latency are shown in Fig 6.1 and Fig 6.5. The frequency histograms of ΔC_m were best fit with a three Gaussian fit: $f(x) = y_0 + A_1 \cdot \exp(-((x-x_01)/w_1)^2) + A_2 \cdot \exp(-((x-x_02)/w_2)^2) + A_3 \cdot \exp(-((x-x_03)/w_3)^2)$. x_01 , x_02 , x_03 was mean of three different Gaussian distribution. Data were shown as Mean \pm SEM.

In CTL/NK cells, lytic granules are release at the IS (Schwarz, Qu et al.). With TIRF microscopy, the release of lytic granules can always be observed in our system, however, in all successfully patched CTLs there were also other capacitance increments which are not caused by lytic granules (shown in Fig 5.2) and these increments later were checked manually. As mentioned above, G_m and G_s were also verified simultaneously. The amplitude of C_m was calculated by averaging the 60 points immediately before and after the capacitance step and taking the difference of the two average values as ΔC_m . The distribution of capacitance steps was plotted in Igor Pro.

5.2.5 Single lytic granule trajectory analysis

The process of single lytic granule tracking was similar to chapter 2.2.4.2, "single granule trajectory analysis". The details of lytic granule trajectories analysis were as follows:

- 1 Download Lipschitz filter and install in Image J 1.46r.
- 2 Open TIRF stack in Image J.
- 3 Adjust the options of Minimum and Maximum in Brightness/Contrast.
- 4 Choose Lipschitz filter and click Tophat and enter Slope: 15.
- 5 Save filtered stack and open with EasyTrack.
- 6 Select Discrete Particles in objects. Normally the fluorescent intensity threshold was set to 30.
- 7 Check every identified granule in each frame. If two granules come close and the intensities of the boundary between these two objects were above threshold, two

vesicles were regarded as one granule. In this situation, separate the two objects manually.

- 8 Repeat step 7 until all the mistakes were corrected.
- 9 Click Find in Trajectories. After both of the parameters Lmin and Dmax were set to 3 click continue.
- 10 Automerge the trajectories. Max distance [pixel] was set to 3 and max gap was started with 3, then increase the max gap gradually to 5, 7, 10, 15, 25, 30.
- 11 Store the trajectories.
- 12 Load the raw TIRF stack into EasyTrack again.
- 13 Load the save trajectories to the raw data and overlay to raw image stack.
- 14 Refine trajectories. SearchRadius was set to 2.
- 15 Store the refined trajectories.
- 16 Trajectories of fusion lytic granules were chosen manually.
- 17 Load the trajectories from previous step into Igor Pro 6.
- 18 Click macro Full Analysis (written by Dr.Detlef Hof). Set appropriate parameters of time window to get caging diameter.
- 19 Store caging diameter as Igor Binary.

Repeat the same procedures to next CTL. Comparison of caging diameter was done in Igor Pro 6. Data were shown as Mean \pm SEM (Standard Error of Mean).

5.2.6 Mean squared displacement detection by TIRF setup

In two dimensions by fluorescent microscopy, the spatial precision of localization, δ_x , of single fluorescent is determined by the equation shown below:

$$\delta_x^2 = \frac{r_0^2 + q^2 / 12}{N} + \frac{8\pi r_0^4 b^2}{q^2 N^2} \text{ (Hess, Girirajan et al. 2006)}$$

where r_0 represents the standard deviation of the point spread function, N is the total number of photons collected, q is the size of an image pixel and b is the background noise per pixel whereas in our setup q is 160 nm, and b is about 1000. Obviously when a sufficient number N of photons is collected, δ_x is almost arbitrarily high accuracy. To obtain the localization accuracy, 0.2 μm in diameter of Tetraspeck™ microspheres were used which could be excited by four lasers 360/430 nm (blue), 505/515 nm (green), 560/580 nm (orange) and 660/680 nm (dark red) lasers. Under 561 nm laser illuminations, fluorescent intensity of 0.2 μm Tetraspeck™ microspheres were around 1800, similar to the intensity of labeled lytic granule when

applied with the same imaging recording setting. The details of this recording were shown in following steps:

1. Suspend TetraSpeck™ beads with 100 µl pipette tip under sterile bench.
2. 5 µl TetraSpeck™ microspheres were taken out and diluted with the same amount of distilled water. The beads were mixed to ensure that they were uniformly suspended in the solution.
3. A 5 µl drop of this mixture was placed at the center of the chamber on a clean glass coverslip.
4. The beads are 0.2 µm so that it is crucial to guarantee the beads dried out completely on the coverslip and stick tightly to the coverslip.
5. According to Snell's law described in Chapter 1.6, the samples exposure directly in the air will make it difficult to form an evanescent field; therefore a small amount of water is required. Apply 5 µl distilled water to place where the beads adhere on the coverslip.
6. The newly added water will cause the beads flow on the coverslip. Break another new clean coverslip, and take a small piece to cover the samples.
7. Samples were placed on the TIRF setups and illuminated with 561 nm laser. Frames were acquired at 10 Hz with 75 ms exposure time.
8. Follow step 2 to 15 from chapter 5.2.5 Single lytic granule trajectory analysis.

A distinct advantage of TIRF setup is the high fluorescent sensitivity which allowed accurate detection of small changes in position. To demonstrate this capability in the setup, immobile beads were used to analyze target acquisition. The caging diameter is used to measure the maximum distance moved within a time window. Once the time window was settled to 1 frame, the caging diameter actually is the square root of the mean squared displacement (MSD): $MSD = (x_{n+1} - x_n)^2 + (y_{n+1} - y_n)^2$, where (x_n, y_n) is the centroid position of bead in frame n. Continuous 9 seconds of trajectories from 10 beads were chosen for MSD histogram analysis. Here in Fig 5.3, it was illustrated that, for Tetraspeck™ microspheres which were 0.2 µm in diameter and had been allowed to dry to adherence on a coverslip, the probability that the centroid position changed within a distance of 16 nm of the XY plane was 96.66% ± 0.94%. The chance of movements in the range of 16 to 32 nm, during the 9 second recording time, in

the lateral direction and $3.34\% \pm 0.94\%$. TIRF microscopy had a high resolution in z-direction due to the fact that fluorescence excited was by the evanescent wave. Accordingly, we observed a relationship between z and intensity change, in which the entire movement of the bead was dominated by jitter within 10 nm ($98.18\% \pm 0.31\%$) with a probability of $1.82\% \pm 0.31\%$ of movements in the range of 10 nm to 20nm. In the nearly immobile state lateral variability of less than 16 nm and vertical jitter of less than 10 nm was tolerated, which corresponds to composition of forces from water molecular hitting bead, bead adhesive to coverslip and

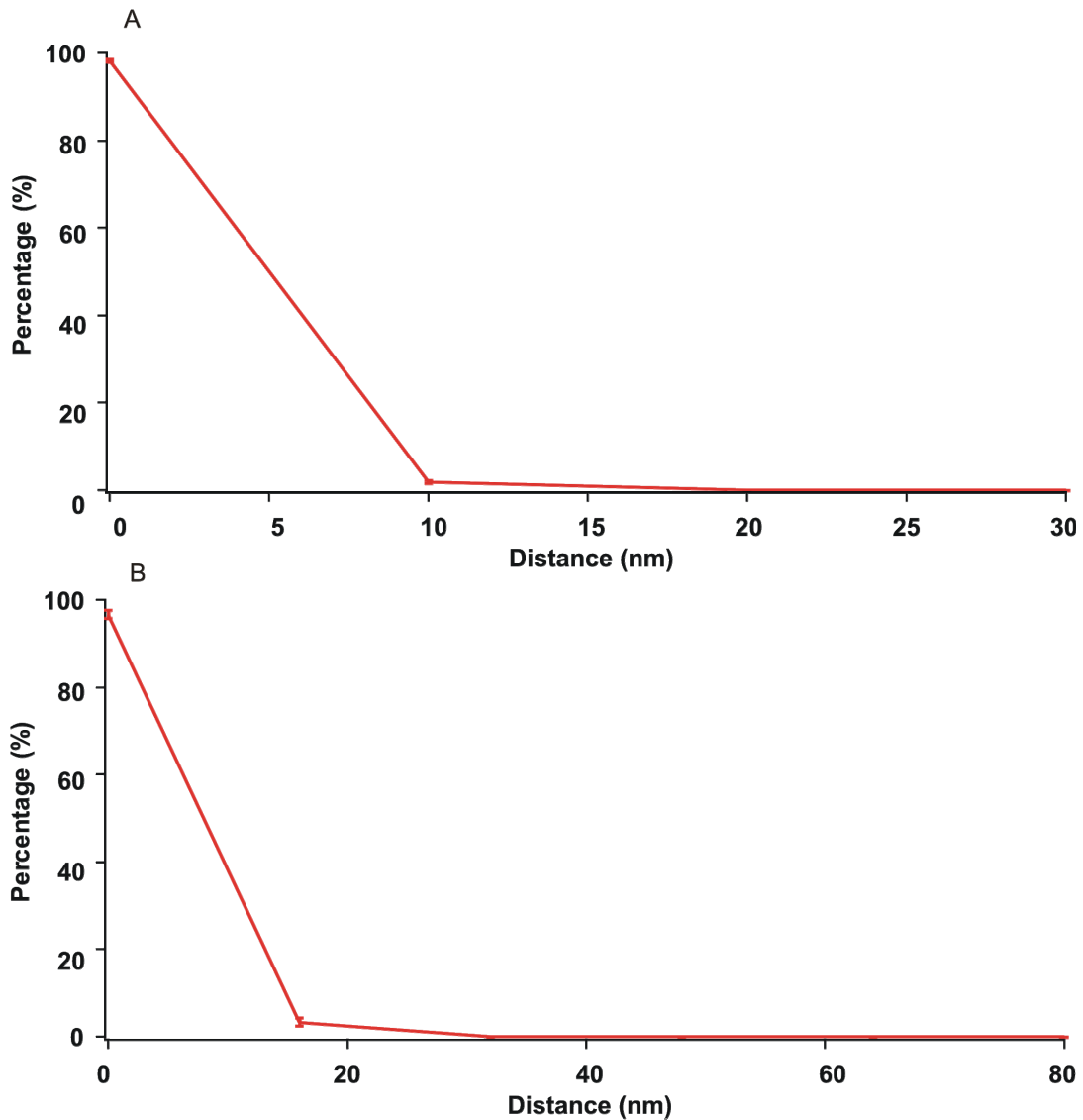


Fig 5.3 Spatial precision of localization δ_x of single fluorescent bead. 10 beads were selected for square root of MSD analysis. histograms of square root of MSD in x-y dimension (A) and z direction (B).

bead covered by glass rather than by the mechanical drift during such short time as 9 seconds recording. The covered glass reduced vertical movement of beads. Hence, using this type of analysis, we could monitor the centroid position change of fluorophore adequately.

6. Results and discussion

6.1 Results

Intracellular perfusion of $2 \mu\text{M Ca}^{2+}$ via the patch pipette was used to stimulate granzyme B-mCherry secretion in human CTLs isolated from PBLs. Whole-cell capacitance and TIRF images were simultaneously recorded. Only release events detected by both methods and tightly coupled in time were considered as lytic granule release events. A typical example of a fusion event was shown in previous graph. 81 fusion events were recorded from 22 CTLs. The smallest lytic granule was 1.14 fF and the largest one was 10.44 fF. The mean capacitance of these granules was 4.38 ± 0.22 fF. The distribution of the ΔC_m of all detected events is shown in Fig 6.1. As depicted in Fig.6.1, the histogram of ΔC_m could be fit using a triple Gaussian equation. This indicates that the granules we observed in human CTLs are not

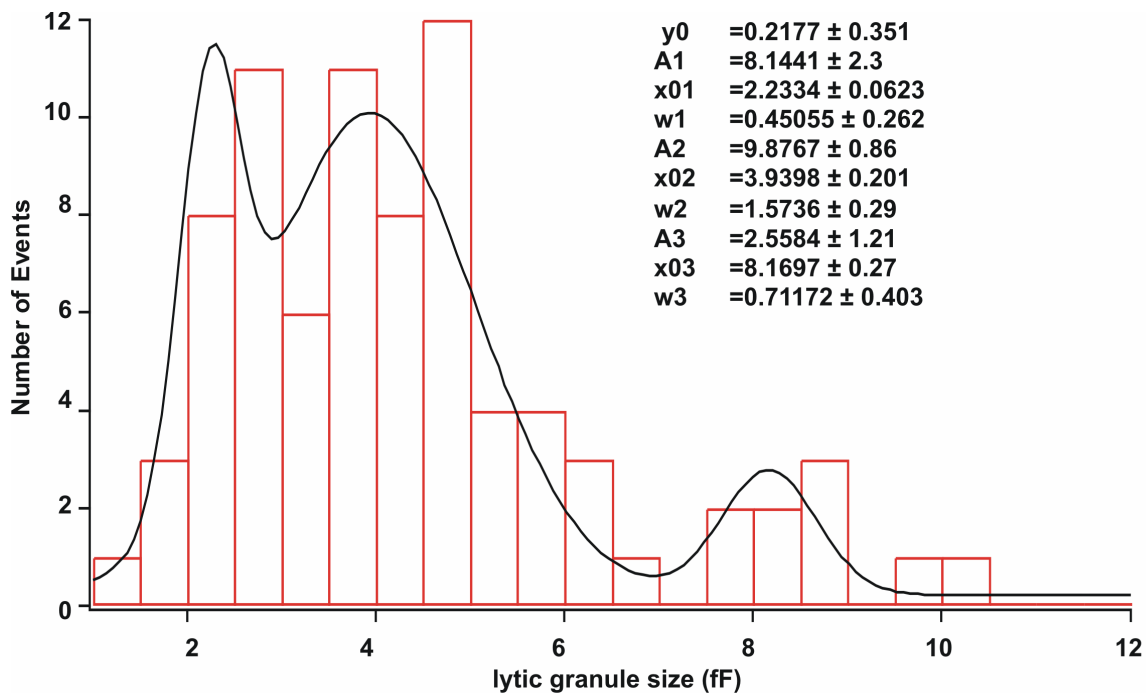


Fig.6.1 Size distributions of lytic granule in human CTLs with $2 \mu\text{M Ca}^{2+}$. Bin size, 0.5 fF. First bar was started at 1.5 fF. The red curve was the three Gauss fitting. The numbers inset were the fitting values. In total 82 lytic granule fusion events were detected in 22 CTLs.

monotonic but rather occur in two or three different populations based on size of the lytic granules. The mean sizes of three groups were 2.23 ± 0.06 fF, 3.94 ± 0.20 fF and 8.17 ± 0.27 fF. If we assume that the lytic granule is approximately spherical, the lipid newly added to plasma membrane is calculated as $\Delta C_m = C^* 4\pi (D/2)^2$ where D

represents the diameter of lytic granule, and assuming C , assumes as $1 \mu\text{F}/\text{cm}^2$ (Gustafsson and Pinter 1984) for membrane capacitance, which varies from 0.7 to 1 (Janshoff and Steinem 2006), these step sizes correlate to granules with diameter range from 190-576 nm and with the peaks at 266 nm, 354 nm, and 509 nm in diameter.

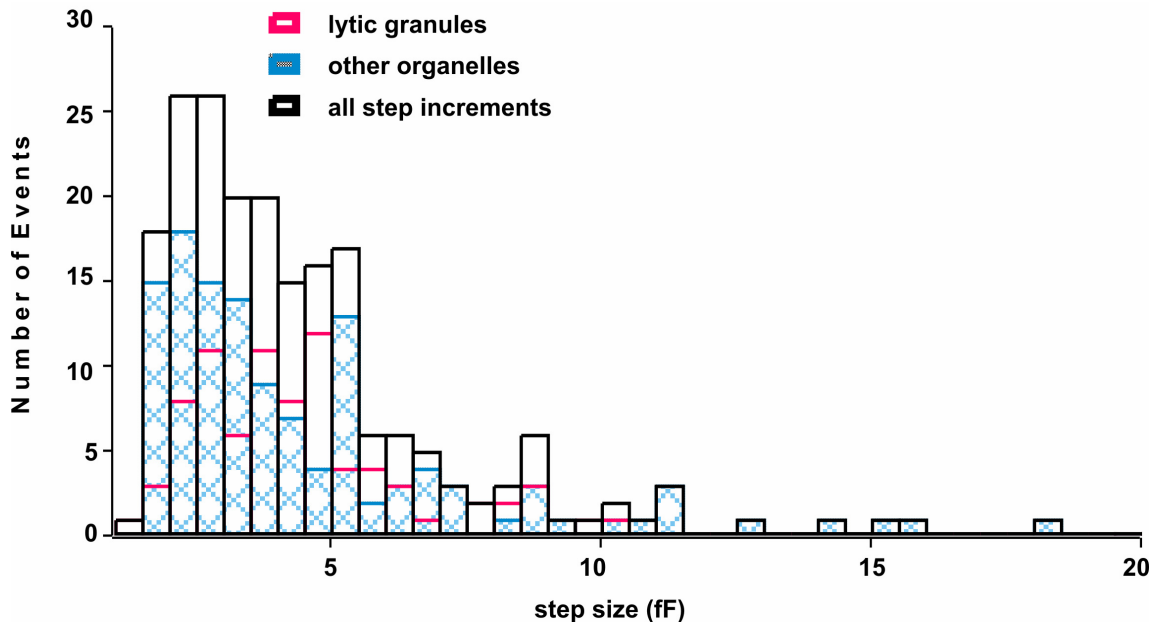


Fig 6.2 Histogram of step sizes. Bin size, 0.5 fF. First bar was started at 1 fF. Pink represents capacitance increment caused by lytic granule secretion (81 events), blue with fill in pattern (122 events) shows step-like increment contributed from other organelles rather than lytic granules. Black (203 events) is the sum up of the first two groups (pink and blue).

After target cell recognition, CTLs gradually become flat and the T cell polarizes and reorganizes its microtubules so that molecules required for the IS can be transported to the conjugating area. The formation of IS is very dynamic, with transport of lytic granules to the IS occurring on demand as target cells are acquired. The major characteristic of CTLs is that lytic granules are released at the IS (Schwarz, Qu et al.). Since in our TIRF experiments, the binding of the T cell is to antibodies on the cover slip, it is here where the IS is generated. Both perforin and granzymes are contained in lytic granules (Peters, Borst et al. 1991), furthermore, granzyme B, a member of granzyme family, and perforin completely colocalized with each other in human CTLs (Stepp, Dufourcq-Lagelouse et al. 1999). Thus all fusion events contributed from lytic granules are expected to occur at the TIRF field and be visible for acquisition. Upon TCR stimulation, the mediators for lytic granule exocytosis including Rab27a (Stinchcombe, Barral et al. 2001) and Munc13-4 move towards IS as well (Purbhoo). These mediators were localized on

endosome-derived exocytic vesicles, specifically distinct from lysosome-derived lytic granule (Menager, Menasche et al. 2007). Additional small intracellular granules which contain chemokines such as RANTES were also verified to be present in human CTLs, and will likely also be secreted rapidly after TCR stimulation (Catalfamo, Karpova et al. 2004). Moreover, recycling endosomes encapsulating p56lck are likely to be directed to release at the periphery of the IS (Ehrlich, Ebert et al. 2002). Since various types of intracellular organelles were competent to fuse with plasma membrane after activation, we expect more capacitance jumps than those contributed by lytic granules. Of the total step-like capacitance events observed in these 22 CTLs, 40.2% were associated with lytic granule exocytosis based on the associated TiRF release signal. The other 121 capacitance events (shown in Fig.5.2) were not associated with an identified lytic granule release event and are likely due to exocytosis of other types of organelles. These capacitance jumps exhibited a similar range of step sizes. There were some large events with step sizes as large as 18.45 fF. These large fusion events in CTLs appeared late in the recordings, after lytic granule release (Fig.6.6).

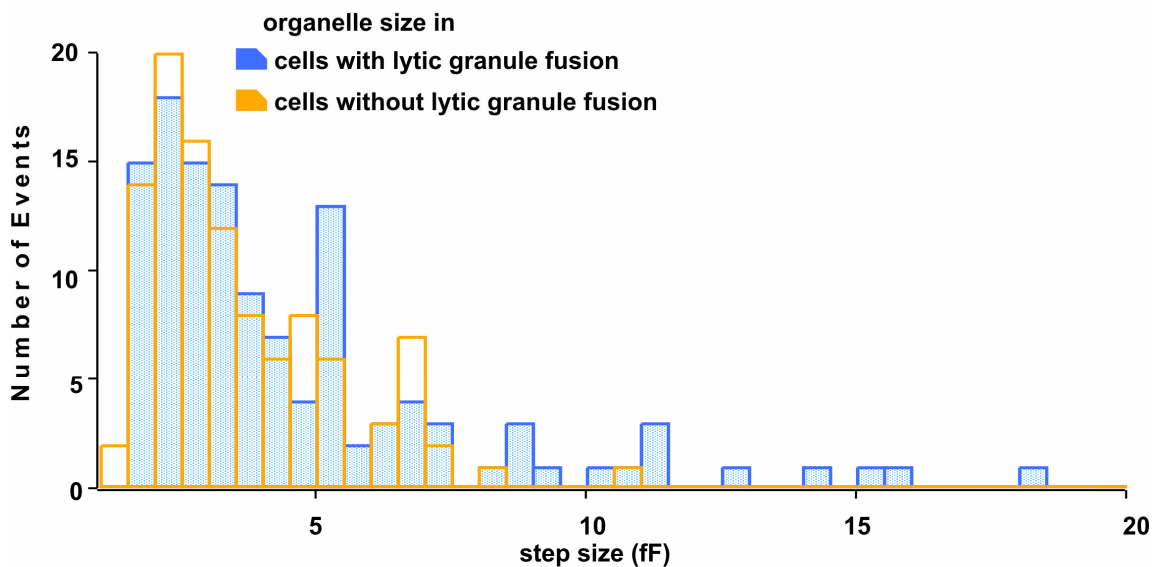


Fig 6.3 Histograms of organelle size in CTLs with lytic granule fusion and without lytic granule detection. The first bar was started at 1 fF and bin size was adjusted to 0.5 fF. Blue with color filling in represent secretory organelles (122 events) from CTL with lytic granule fusion and secretory organelles (106 events) from CTL without lytic granule fusion were painted in naturals.

As clearly illustrated in Fig 6.2, prominent peaks of capacitance steps from other intracellular organelles accumulate around 2 fF and 5.5 fF. It is likely that there are also some smaller events which not resolvable under our recording conditions, but

these are probably not lytic granules, based on the size distribution of identified lytic granules and our ability to correlate all TIRF-based granules release events with capacitance steps. We compared the capacitance steps of known lytic granules with the remaining capacitance steps observed in the same cell population. There was no significant difference in the sizes of these two sets of events (Mann-whitney u test, $p = 0.2$).

A similar pattern of capacitance events also was observed in 19 CTLs recorded with gigaohm seals and stable access conductance during capacitance recording, in which no lytic granule fusion events were observed in TIRF. In these cells we acquired 106 capacitance steps. I analyzed the distribution of these events as well and the results of this analysis were shown in Fig 6.3. Though the distributions of the event amplitudes were not statistically different in these two groups, those CTLs with lytic granule fusion exhibited more fusion events with amplitudes greater than 5fF. Though large fusion events (greater than 10fF) occurred more often in cells in which lytic granule secretion was observed, such events were rare in both groups of cells (Fig.6.4). The Mann-whitney u test p value from was applied to all capacitance jumps generated from CTLs with and without lytic granule fusion. The p value equals to 0.01, hence, there was statistical difference between these two groups. Thus, it is possible that one could distinguish the two cell populations based on the presence of larger secretion events.

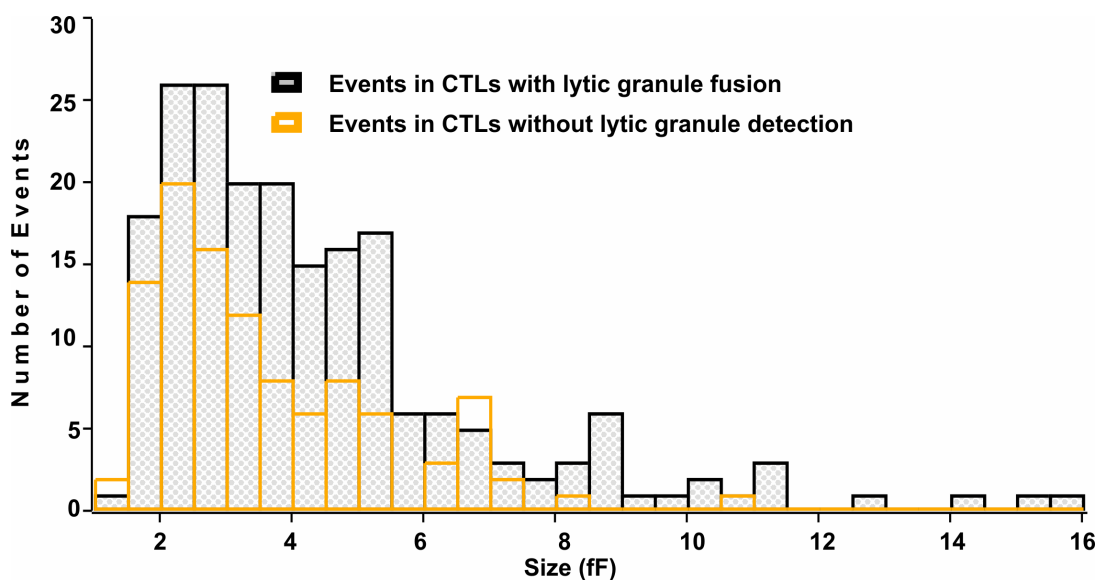


Fig 6.4 Histograms of all capacitance jumps in CTLs. Those cells with lytic granule fusion (black with gray fill in, 203 events) and those without lytic granule detection (khaki, 106 events). The bin size was 0.5 fF. The first bar was at 1 fF. Bin size was adapted to 0.5 fF.

I also examined the distribution of latencies for fusion events. To do this, granule fusion events were plotted as a function of time after breaking to the whole cell configuration. It is notable that most of lytic granule fusion events were detected within the first 80s after the start of exchange of the 2 μM free Ca^{2+} of the pipette with the cytosol of the CTL. The earliest fusion event occurred with a latency of 1.08 s.

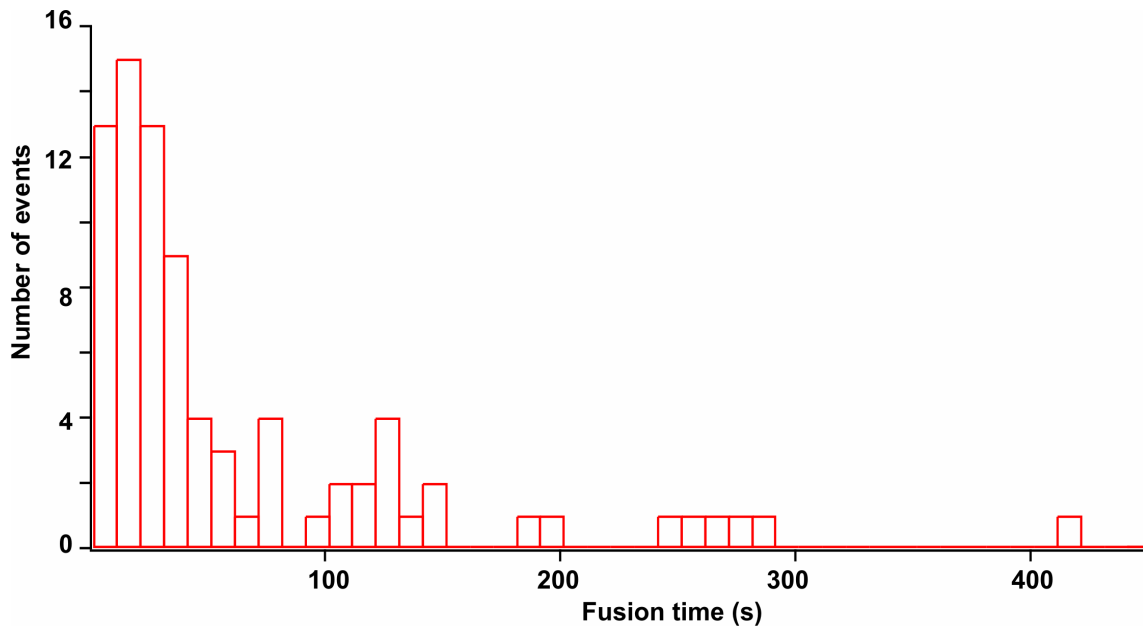


Fig.6.5 Frequency distribution of the fusion latency with bin size of 10s. Contains 81 lytic granule fusion events from 22 CTLs.

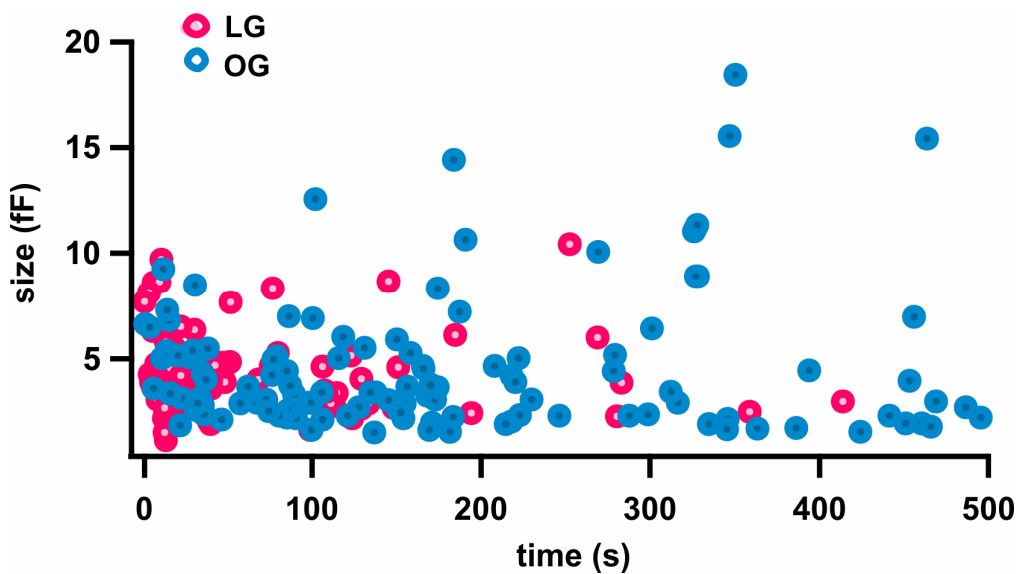


Fig6.6 Capacitance amplitude versus latency time. LG: lytic granules (81 events), OG: other events not associated with lytic granule fusion events (122 events). LG and OG are from the same cell population.

Fig.6.5 shows that a distinct peak of the latency time histogram was present near 20s. To determine whether the latency time was related with amplitude of capacitance, I plotted capacitance jumps versus latency time from CTLs which showed lytic granule secretion in Fig.6.6. It reveals that in both groups fusion events less than 10fF preferentially occurred at early time and there was no release priority based on event size. We conclude that in activated CTLs, secretion was not exclusively due to lytic granules, but that other organelles also fused with the membrane. These populations could not be distinguished based on their sizes, and latency of fusion times were also not correlated with organelle size, at early times.

We observed that during under application of 2 μM free Ca^{2+} , which was reported to be the physiological intracellular concentration during activation of T cells (Feske, Skolnik et al.; Cahalan, Wulff et al. 2001), though a number of lytic granules (9.71 ± 0.45 from 81 lytic granule events) were transported to the IS and accumulated in the evanescent field, only one secretion event was observed (Fig 5.1). This indicates that in CTLs not all lytic granules achieve fusion competence. This is not unexpected as it is known that CTLs do not release all of the available granules during killing of a single

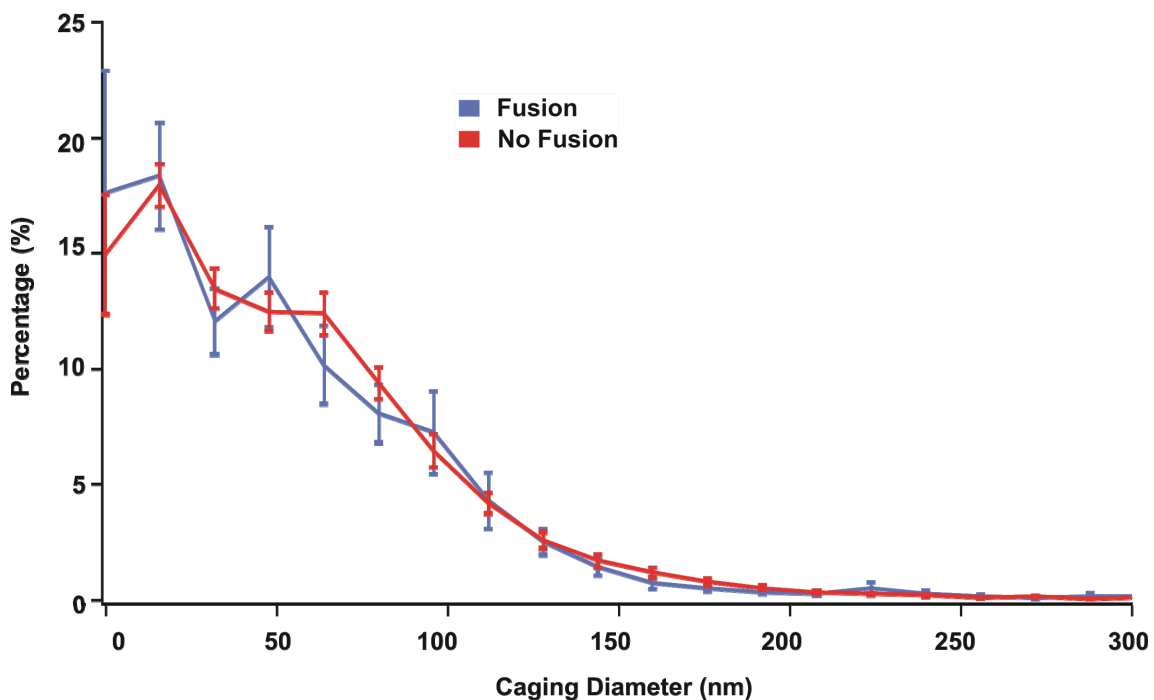


Fig 6.7 Comparison of caging diameters of trajectories of granules which fused and those granules which failed to fuse. These trajectories are all from CTLs in which fusion of lytic granules occurred. Caging diameters were calculated using a sliding time window of 1 s. In 19 CTLs, 58 trajectories of fusing granules and 812 trajectories of granules which did not fuse were analyzed.

target cell, but rather break contact and seek new targets. After a new contact has been established, the immune synapse is established and release of lytic granules occurs at the new target cell. This release can consist of granules in stock, and /or newly synthesized granules (Griffiths 1995; Isaaz, Baetz et al. 1995).

This means that granules which reside at the plasma membrane do not necessarily achieve fusion competence. We have attempted to distinguish between fusion competent primed and unprimed granules based on their motility in the TIRF field. We have

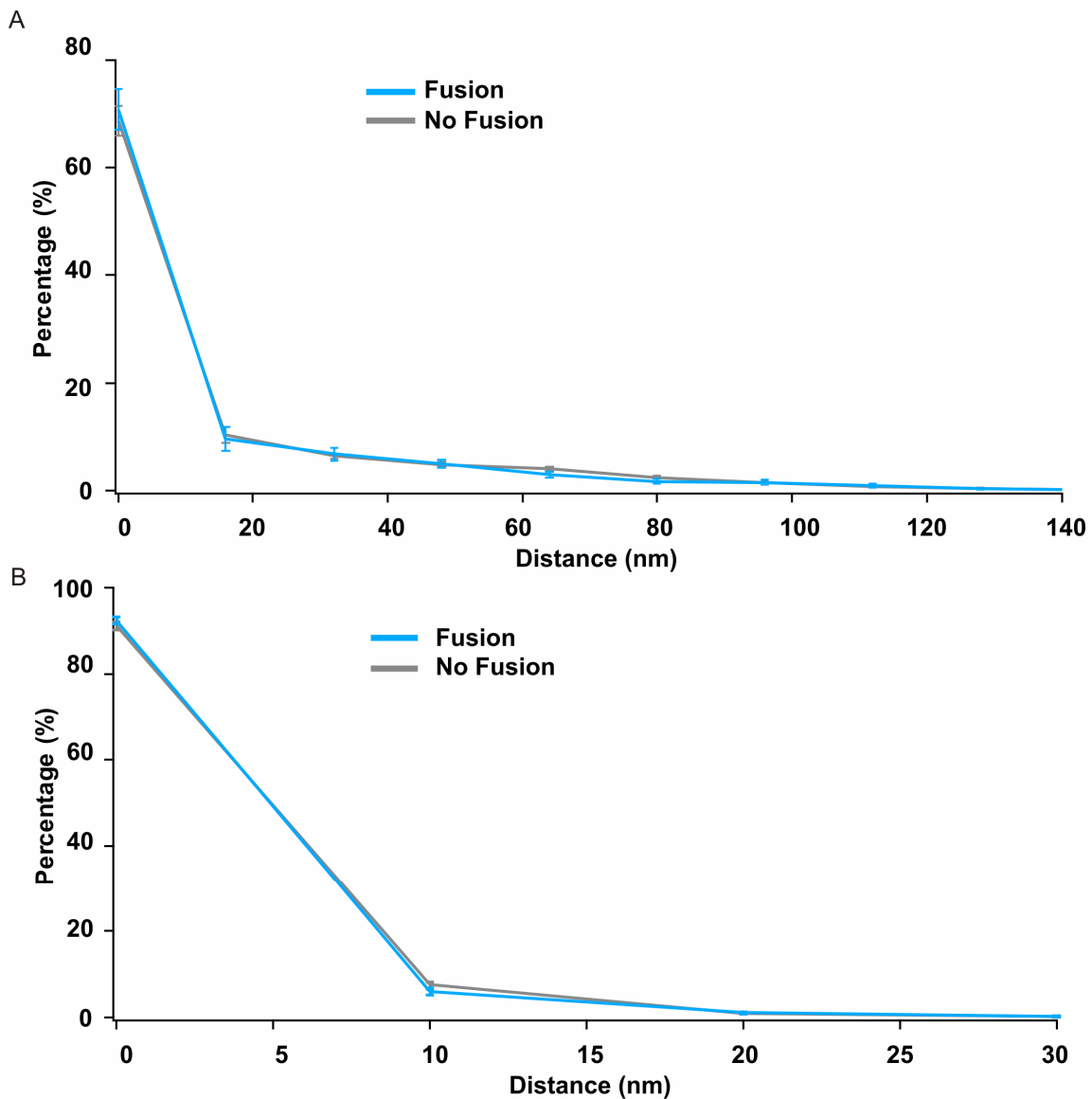


Fig 6.8 Histogram of MSD showing those granules which fused and granules in which fusion did not occur. Panel A: Values in the in x-y planes (interval: 16 nm). Panel B: Data in the in z orientation (interval: 10 nm).

compared the movement of those lytic granules which were secreted with that of those which were not release. To quantify granule movements, an analysis of the granules trajectory was carried out. The caging diameter was then calculated as the maximum distance a granule traveled within a given time period. In bovine chromaffin cells, the movements of fusion competent granules were restricted to a more narrow area

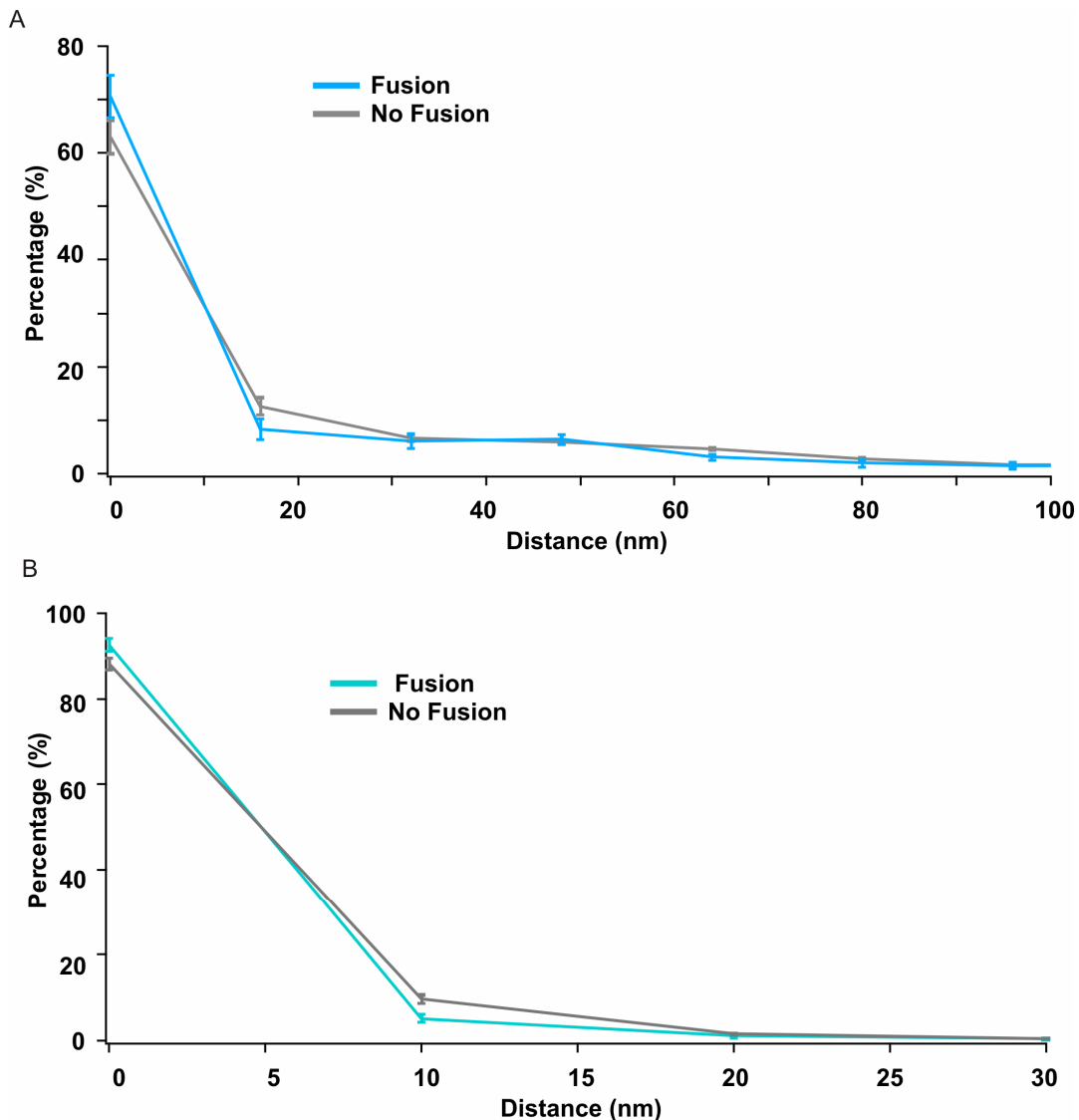


Fig 6.9 Comparison between fusion competent granules and fusion incompetent granules. The distance shown is that which a granule travels within one frame. The trajectories of the last five seconds prior to fusion were compared with continuous five seconds of non-fusion trajectories. A: in x-y direction (interval: 16 nm), B: in z orientation (interval: 10 nm).

(Nofal, Becherer et al. 2007) in contrast to unprimed granules. We therefore examined caging diameters of the lytic granules of the 19 CTLs in which secretion occurred. The caging diameter comparison (Fig.6.7) revealed no significant

differences between fusing granules (58 trajectories) and those which failed to fuse (812 trajectories). Thus there was no difference in velocity or caging diameter of fusion-competent and non fusion-competent granules.

We then examined the mean-squared-displacement of these granules Fig.5.3. The histogram of the square root of the MSD (Fig.6.8) from entire trajectories showed that in the x-y position or z direction the trajectories of granules which eventually fused (58 trajectories) were similar to those of granules which did not undergo fusion (812 trajectories). To test the possibility that the maturation of fusion competent granules was transient and that the long time trajectories were masking this effect, since the primed state may be observed only at the end of the track, we analyzed the last five seconds of the granule trajectories of fusing granules, and compared this result with the results for non-fusing granules and with five second segments of tracks of non-fusing granules.

We found that those granules which eventually fused had a slightly higher probability exhibiting an MSD whose square root was 16 nm or less (Fig 6.9, $70.7\% \pm 4.01\%$), which is similar to the mobility of fixed beads in our TIRF setup, than did those granules that did not fuse ($62.98\% \pm 3.13\%$) though this difference was not statistically significant. The granules which did not fuse spent $12.61\% \pm 1.66\%$ of the time in a pattern in which the mobility was restricted to 16 to 32 nm and $4.58\% \pm 0.28\%$ with mobility restricted within 48 to 64 nm. Those granules which fused had trajectories with $8.36\% \pm 1.99\%$ of the time spent within 16-32 nm and $3.08\% \pm 0.64\%$, of the time spent in the 48-64 nm range. In the Z axis, the group of fusing vesicles stay in the jittering state (within 10 nm) with a higher probability $92.69\% \pm 1.48\%$ than did the non-fusing group $88.17\% \pm 1.34\%$; within distance 10 nm to 20 nm, the time of no fusion group is $9.65\% \pm 0.99\%$ and $5.16\% \pm 0.93\%$ of fusion group respectively. Importantly, even the fusion competent granules exhibited bursts of mobility which was never in fixed beads (X-Y: > 32 nm, z: > 20 nm, Fig.5.3). Thus, based on our observations the mobility and velocity of those granules which eventually fused were no significant different from that of the granules which did not fuse.

6.2 Discussion

We have identified the membrane capacitance changes associated with the fusion of lytic granules of cytotoxic T-lymphocytes. Cytotoxic T lymphocytes are “serial killers” (Morimoto, Letvin et al. 1985). Through the release of cytotoxic substances perforin and granzymes from lytic granules, they kill tumor cells or virus-infected cells. Previous reports based on electron micrographs have suggested that granules vary from 250-300 nm (Krzewski and Coligan), 450-500 nm (Burkhardt, McIlvain et al. 1993) or 700 nm (Peters, Borst et al. 1991). The differences may reflect true variability in granules, or may result from granules in varying stages of biogenesis. It is also likely that not all granules identified in these studies are true lytic granules or that their observed size may be affected by processing techniques such as chemical fixation.

In this study, I have established a method to identify fusion events of single lytic granules in human CTLs using live TIRF microscopy. I have simultaneously recorded membrane capacitance and utilized granzyme B expression to positively identify lytic granule fusion events. This allowed me to unambiguously correlate the membrane capacitance jumps resulting from fusion with the fusion of granzyme B containing lytic granules observed in TIRF illumination. The capacitance jumps of granzyme B containing lytic granules ranged from 1.14 to ~10.44 fF. Frequency histograms of capacitance change indicate one or two main populations. These graphs could be fit with two Gaussian components with peaks as 2.23 fF and 3.94 fF. There were a small number of larger events which may represent a special form of granule or perhaps merged granules. This combination of methods indicates that lytic granules release accounts for only about 26% of secreted organelles in this size range in these activated T-lymphocytes. It is likely that a number of secretory events were missed due to the sensitivity limits of our capacitance measurements. However, based on the size distribution we observed it is unlikely that we missed lytic granule fusion events. The size distribution of capacitance jumps which were not associated with granzyme B positive TIRF events were similar to those of lytic granules though on average slightly smaller (Fig.6.2).

The signaling by calcium in T cells has been intensively studied (Hoth and Niemeyer; Niemeyer and Hoth; Shaw, Qu et al.; Gray, Gnarr et al. 1987; Lyubchenko, Wurth et al. 2001; Wurth and Zweifach 2002; Fierro, Wurth et al. 2004; Wu, Buchanan et al. 2006; Luik, Wang et al. 2008; Quintana, Pasche et al. 2011). Calcium plays an important role in IS formation and stabilization (Negulescu, Krasieva et al. 1996), and in

granule/MTOC reorientation (Kupfer, Swain et al. 1987; Kuhne, Lin et al. 2003). Typically the elevation of intracellular calcium involves CRAC channel activation following endoplasmic reticulum calcium store depletion (Wu, Buchanan et al. 2006; Luik, Wang et al. 2008). We have measured the latency of lytic granule release in T-cells following their activation under conditions of low extracellular calcium. Under these conditions, activation occurs and IS formation proceeds but lytic granules release does not occur (Takayama and Sitkovsky 1987; Trenn, Takayama et al. 1987; Pattu, Qu et al. 2011). After activation at low extracellular calcium, raising intracellular calcium via patch pipette leads to lytic granule release with a delay of 70.14 s (70.1383 ± 9.36 s) on average although the shortest observed latency was 1.08 s. Typically the diffusion of buffered calcium in the cytosol of most cells are rapid and within one CTL calcium would be expected to equilibrate everywhere in $\sim 0.3 - 3$ s (Lyubchenko, Wurth et al. 2001). This raised the question what occurs during the latency time besides calcium elevation.

Calcium signal in CTLs is not a binary signal and the oscillations in calcium concentration are critical for T cell functions (Lewis 2001). Granules are transported to the IS, tether, dock and await priming. As soon as they are primed, they fuse with the membrane and release their contents. It is thus unlikely that granules prime and then await an increase in intracellular free calcium as is the case in neurons and neuroendocrine cells. It may be that under conditions of low extracellular calcium the free intracellular calcium remains too low to support all phases of granules preparation and though the IS is present delivery and /or docking depend on higher calcium levels which are reached after raising extracellular calcium. Another possibility is the release of lytic granule also requires activation of kinases (Grybko, Pores-Fernando et al. 2007; Ma, Haydar et al. 2008) or ERK activation (Trotta, Puorro et al. 1998), or CD3-containing endosome pairing (Qu, Pattu et al. 2011), or mediators colocalizing with lytic granules (Topham and Hewitt 2009).

Lytic granules move along the MTOC microtubules before switch to filamentous actin network at IS where is close proximity to membrane and then granules were tethered by protein such as members from munc family, SNARE components, etc (Bertrand, Muller et al.; Krzewski and Coligan; Lyubchenko, Wurth et al. 2003). Our trajectory analysis supports this scenario that fusion competent granules in the last five seconds had a high chance to stay in a jittering state where is the suitable distance for molecular interaction. It has been suggested that the process of docking and priming sequentially decrease the freedom of movement of granules (Pasche, Matti et al.). We have not observed a decrease in mobility prior to fusion, an observation that is also consistent with the idea that

granules do not dwell in the primed state but rather fuse quickly following priming (refer as jittering) in a long time or with a mechanism that provides an opportunity with high percentage to reverse into state with trivial mobility (refer as jittering state) in transient time.

In summary, we show that lytic granules exhibit a distribution with possibly two peaks, at 266 nm and 354 nm in diameter. Most of fusion occurred within 80 seconds and up to four granules in one CTL are released. Secretion was not exclusively due to lytic granules in activated CTLs, and other organelles also fused with the membrane. These two groups of secreted organelles could not be distinguished based on their sizes, or on the latency of fusion times were also not correlated with organelle size. When localized at the IS, lytic granules preferentially exhibit a state of low mobility which likely is associated with the docked state. However, those lytic granules which eventually fused with the plasma membrane spent much of their time in an immobile state but also show increases in mobility indicating that they may undock without priming. There is no obvious change in mobility prior to fusion.

Reference

- Allen, J. M., T. E. Adrian, et al. (1983). "Neuropeptide Y (NPY) in the adrenal gland." J Auton Nerv Syst **9**(2-3): 559-63.
- Ashery, U., A. Betz, et al. (1999). "An efficient method for infection of adrenal chromaffin cells using the Semliki Forest virus gene expression system." Eur J Cell Biol **78**(8): 525-32.
- Ashery, U., F. Varoqueaux, et al. (2000). "Munc13-1 acts as a priming factor for large dense-core vesicles in bovine chromaffin cells." Embo J **19**(14): 3586-96.
- Aunis, D. and K. Langley (1999). "Physiological aspects of exocytosis in chromaffin cells of the adrenal medulla." Acta Physiol Scand **167**(2): 89-97.
- Baumert, M., P. R. Maycox, et al. (1989). "Synaptobrevin: an integral membrane protein of 18,000 daltons present in small synaptic vesicles of rat brain." Embo J **8**(2): 379-84.
- Berglund, P., M. Sjöberg, et al. (1993). "Semliki Forest virus expression system: production of conditionally infectious recombinant particles." Biotechnology (N Y) **11**(8): 916-20.
- Bertrand, F., S. Müller, et al. "An initial and rapid step of lytic granule secretion precedes microtubule organizing center polarization at the cytotoxic T lymphocyte/target cell synapse." Proc Natl Acad Sci U S A **110**(15): 6073-8.
- Borisovska, M., Y. Zhao, et al. (2005). "v-SNAREs control exocytosis of vesicles from priming to fusion." Embo J **24**(12): 2114-26.
- Bowen, M. and A. T. Brunger (2006). "Conformation of the synaptobrevin transmembrane domain." Proc Natl Acad Sci U S A **103**(22): 8378-83.
- Browne, K. A., E. Blink, et al. (1999). "Cytosolic delivery of granzyme B by bacterial toxins: evidence that endosomal disruption, in addition to transmembrane pore formation, is an important function of perforin." Mol Cell Biol **19**(12): 8604-15.
- Burkhardt, J. K., J. M. McIlvain, Jr., et al. (1993). "Lytic granules from cytotoxic T cells exhibit kinesin-dependent motility on microtubules in vitro." J Cell Sci **104** (Pt 1): 151-62.
- Buzza, M. S. and P. I. Bird (2006). "Extracellular granzymes: current perspectives." Biol Chem **387**(7): 827-37.
- Cahalan, M. D. and K. G. Chandy (2009). "The functional network of ion channels in T lymphocytes." Immunol Rev **231**(1): 59-87.
- Cahalan, M. D., H. Wulff, et al. (2001). "Molecular properties and physiological roles of ion channels in the immune system." J Clin Immunol **21**(4): 235-52.

- Catalfamo, M., T. Karpova, et al. (2004). "Human CD8+ T cells store RANTES in a unique secretory compartment and release it rapidly after TcR stimulation." Immunity **20**(2): 219-30.
- Chapman, E. R. (2008). "How does synaptotagmin trigger neurotransmitter release?" Annual Review of Biochemistry **77**: 615-641.
- Chen, X., D. R. Tomchick, et al. (2002). "Three-dimensional structure of the complexin/SNARE complex." Neuron **33**(3): 397-409.
- Chen, Y. A. and R. H. Scheller (2001). "SNARE-mediated membrane fusion." Nat Rev Mol Cell Biol **2**(2): 98-106.
- Deak, F., Y. Xu, et al. (2009). "Munc18-1 binding to the neuronal SNARE complex controls synaptic vesicle priming." J Cell Biol **184**(5): 751-64.
- DiCiommo, D. P. and R. Bremner (1998). "Rapid, high level protein production using DNA-based Semliki Forest virus vectors." J Biol Chem **273**(29): 18060-6.
- Duke, R. C., P. M. Persechini, et al. (1989). "Purified perforin induces target cell lysis but not DNA fragmentation." J Exp Med **170**(4): 1451-6.
- Dukkipati, V. S., H. T. Blair, et al. (2006). "'Ovar-Mhc' - ovine major histocompatibility complex: structure and gene polymorphisms." Genet Mol Res **5**(4): 581-608.
- Dustin, M. L. and D. Depoil "New insights into the T cell synapse from single molecule techniques." Nat Rev Immunol **11**(10): 672-84.
- Ehrlich, L. I., P. J. Ebert, et al. (2002). "Dynamics of p56lck translocation to the T cell immunological synapse following agonist and antagonist stimulation." Immunity **17**(6): 809-22.
- Elferink, L. A., W. S. Trimble, et al. (1989). "Two vesicle-associated membrane protein genes are differentially expressed in the rat central nervous system." J Biol Chem **264**(19): 11061-4.
- Fasshauer, D., H. Otto, et al. (1997). "Structural changes are associated with soluble N-ethylmaleimide-sensitive fusion protein attachment protein receptor complex formation." J Biol Chem **272**(44): 28036-41.
- Fasshauer, D., R. B. Sutton, et al. (1998). "Conserved structural features of the synaptic fusion complex: SNARE proteins reclassified as Q- and R-SNAREs." Proc Natl Acad Sci U S A **95**(26): 15781-6.
- Fdez, E., M. Martinez-Salvador, et al. "Transmembrane-domain determinants for SNARE-mediated membrane fusion." J Cell Sci **123**(Pt 14): 2473-80.
- Fernandez-Chacon, R., A. Konigstorfer, et al. (2001). "Synaptotagmin I functions as a calcium regulator of release probability." Nature **410**(6824): 41-49.
- Fernandez, I., J. Ubach, et al. (1998). "Three-dimensional structure of an evolutionarily conserved N-terminal domain of syntaxin 1A." Cell **94**(6): 841-9.

- Feske, S. (2007). "Calcium signalling in lymphocyte activation and disease." Nat Rev Immunol **7**(9): 690-702.
- Feske, S., E. Y. Skolnik, et al. "Ion channels and transporters in lymphocyte function and immunity." Nat Rev Immunol **12**(7): 532-47.
- Fierro, A. F., G. A. Wurth, et al. (2004). "Cross-talk with Ca(2+) influx does not underlie the role of extracellular signal-regulated kinases in cytotoxic T lymphocyte lytic granule exocytosis." J Biol Chem **279**(24): 25646-52.
- Giraudou, C. G., W. S. Eng, et al. (2006). "A clamping mechanism involved in SNARE-dependent exocytosis." Science **313**(5787): 676-80.
- Graham, M. E., P. Washbourne, et al. (2001). "SNAP-25 with mutations in the zero layer supports normal membrane fusion kinetics." J Cell Sci **114**(Pt 24): 4397-405.
- Graubert, T. A., J. F. DiPersio, et al. (1997). "Perforin/granzyme-dependent and independent mechanisms are both important for the development of graft-versus-host disease after murine bone marrow transplantation." J Clin Invest **100**(4): 904-11.
- Gray, L. S., J. R. Gnarra, et al. (1987). "Demonstration of a calcium influx in cytolytic T lymphocytes in response to target cell binding." J Immunol **138**(1): 63-9.
- Greene, L. A. and A. S. Tischler (1976). "Establishment of a noradrenergic clonal line of rat adrenal pheochromocytoma cells which respond to nerve growth factor." Proc Natl Acad Sci U S A **73**(7): 2424-8.
- Griffiths, G. M. (1995). "The cell biology of CTL killing." Curr Opin Immunol **7**(3): 343-8.
- Grossman, W. J., P. A. Revell, et al. (2003). "The orphan granzymes of humans and mice." Curr Opin Immunol **15**(5): 544-52.
- Grossman, W. J., J. W. Verbsky, et al. (2004). "Differential expression of granzymes A and B in human cytotoxic lymphocyte subsets and T regulatory cells." Blood **104**(9): 2840-8.
- Grote, E., J. C. Hao, et al. (1995). "A targeting signal in VAMP regulating transport to synaptic vesicles." Cell **81**(4): 581-9.
- Grybko, M. J., A. T. Pores-Fernando, et al. (2007). "Protein kinase C activity is required for cytotoxic T cell lytic granule exocytosis, but the theta isoform does not play a preferential role." J Leukoc Biol **81**(2): 509-19.
- Gustafsson, B. and M. J. Pinter (1984). "Relations among passive electrical properties of lumbar alpha-motoneurons of the cat." J Physiol **356**: 401-31.
- Hamill, O. P., A. Marty, et al. (1981). "Improved patch-clamp techniques for high-resolution current recording from cells and cell-free membrane patches." Pflugers Arch **391**(2): 85-100.

Hammarlund, M., S. Watanabe, et al. (2008). "CAPS and syntaxin dock dense core vesicles to the plasma membrane in neurons." Journal of Cell Biology **180**(3): 483-491.

Hanson, P. I., J. E. Heuser, et al. (1997). "Neurotransmitter release - four years of SNARE complexes." Curr Opin Neurobiol **7**(3): 310-5.

Hartmann, J., S. Sceppek, et al. (1995). "Regulation of granule size in human and horse eosinophils by number of fusion events among unit granules." J Physiol **483** (Pt 1): 201-9.

Hess, S. T., T. P. Girirajan, et al. (2006). "Ultra-high resolution imaging by fluorescence photoactivation localization microscopy." Biophys J **91**(11): 4258-72.

Hoth, M. and B. A. Niemeyer "The Neglected CRAC Proteins: Orai2, Orai3, and STIM2." Curr Top Membr **71**: 237-71.

Isaaz, S., K. Baetz, et al. (1995). "Serial killing by cytotoxic T lymphocytes: T cell receptor triggers degranulation, re-filling of the lytic granules and secretion of lytic proteins via a non-granule pathway." Eur J Immunol **25**(4): 1071-9.

Jahn, R. and D. Fasshauer "Molecular machines governing exocytosis of synaptic vesicles." Nature **490**(7419): 201-7.

Jahn, R. and R. H. Scheller (2006). "SNAREs--engines for membrane fusion." Nat Rev Mol Cell Biol **7**(9): 631-43.

Janshoff, A. and C. Steinem (2006). "Transport across artificial membranes-an analytical perspective." Anal Bioanal Chem **385**(3): 433-51.

Ju, S. T., H. Cui, et al. (1994). "Participation of target Fas protein in apoptosis pathway induced by CD4+ Th1 and CD8+ cytotoxic T cells." Proc Natl Acad Sci U S A **91**(10): 4185-9.

Kagi, D., B. Ledermann, et al. (1996). "Molecular mechanisms of lymphocyte-mediated cytotoxicity and their role in immunological protection and pathogenesis in vivo." Annu Rev Immunol **14**: 207-32.

Kasai, H. (1999). "Comparative biology of Ca²⁺-dependent exocytosis: implications of kinetic diversity for secretory function." Trends in Neurosciences **22**(2): 88-93.

Krzewski, K. and J. E. Coligan "Human NK cell lytic granules and regulation of their exocytosis." Front Immunol **3**: 335.

Kuhne, M. R., J. Lin, et al. (2003). "Linker for activation of T cells, zeta-associated protein-70, and Src homology 2 domain-containing leukocyte protein-76 are required for TCR-induced microtubule-organizing center polarization." J Immunol **171**(2): 860-6.

Kummerow, C., C. Junker, et al. (2009). "The immunological synapse controls local and global calcium signals in T lymphocytes." Immunol Rev **231**(1): 132-47.

- Kupfer, A., S. L. Swain, et al. (1987). "The specific direct interaction of helper T cells and antigen-presenting B cells. II. Reorientation of the microtubule organizing center and reorganization of the membrane-associated cytoskeleton inside the bound helper T cells." J Exp Med **165**(6): 1565-80.
- Lang, T., I. Wacker, et al. (1997). "Ca²⁺-triggered peptide secretion in single cells imaged with green fluorescent protein and evanescent-wave microscopy." Neuron **18**(6): 857-63.
- Langosch, D., J. M. Crane, et al. (2001). "Peptide mimics of SNARE transmembrane segments drive membrane fusion depending on their conformational plasticity." J Mol Biol **311**(4): 709-21.
- Lewis, R. S. (2001). "Calcium signaling mechanisms in T lymphocytes." Annu Rev Immunol **19**: 497-521.
- Liljestrom, P. and H. Garoff (1991). "A new generation of animal cell expression vectors based on the Semliki Forest virus replicon." Biotechnology (N Y) **9**(12): 1356-61.
- Lin, X. G., M. Ming, et al. "UNC-31/CAPS docks and primes dense core vesicles in *C. elegans* neurons." Biochem Biophys Res Commun **397**(3): 526-31.
- Lis, A., C. Peinelt, et al. (2007). "CRACM1, CRACM2, and CRACM3 are store-operated Ca²⁺ channels with distinct functional properties." Curr Biol **17**(9): 794-800.
- Liu, D., J. A. Martina, et al. "Two modes of lytic granule fusion during degranulation by natural killer cells." Immunol Cell Biol **89**(6): 728-38.
- Liu, Y., C. Schirra, et al. (2008). "CAPS facilitates filling of the rapidly releasable pool of large dense-core vesicles." J Neurosci **28**(21): 5594-601.
- Lollike, K. and M. Lindau (1999). "Membrane capacitance techniques to monitor granule exocytosis in neutrophils." J Immunol Methods **232**(1-2): 111-20.
- Luik, R. M., B. Wang, et al. (2008). "Oligomerization of STIM1 couples ER calcium depletion to CRAC channel activation." Nature **454**(7203): 538-42.
- Lyubchenko, T. A., G. A. Wurth, et al. (2001). "Role of calcium influx in cytotoxic T lymphocyte lytic granule exocytosis during target cell killing." Immunity **15**(5): 847-59.
- Lyubchenko, T. A., G. A. Wurth, et al. (2003). "The actin cytoskeleton and cytotoxic T lymphocytes: evidence for multiple roles that could affect granule exocytosis-dependent target cell killing." J Physiol **547**(Pt 3): 835-47.
- Ma, C., W. Li, et al. "Munc13 mediates the transition from the closed syntaxin-Munc18 complex to the SNARE complex." Nat Struct Mol Biol **18**(5): 542-9.
- Ma, J. S., T. F. Haydar, et al. (2008). "Protein kinase C delta localizes to secretory lysosomes in CD8⁺ CTL and directly mediates TCR signals leading to granule exocytosis-mediated cytotoxicity." J Immunol **181**(7): 4716-22.

- Mashanov, G. I., D. Tacon, et al. (2003). "Visualizing single molecules inside living cells using total internal reflection fluorescence microscopy." Methods **29**(2): 142-52.
- Masson, D., P. J. Peters, et al. (1990). "Interaction of chondroitin sulfate with perforin and granzymes of cytolytic T-cells is dependent on pH." Biochemistry **29**(51): 11229-35.
- Masson, D. and J. Tschopp (1985). "Isolation of a lytic, pore-forming protein (perforin) from cytolytic T-lymphocytes." J Biol Chem **260**(16): 9069-72.
- McMahon, H. T., Y. A. Ushkaryov, et al. (1993). "Cellubrevin is a ubiquitous tetanus-toxin substrate homologous to a putative synaptic vesicle fusion protein." Nature **364**(6435): 346-9.
- Menager, M. M., G. Menasche, et al. (2007). "Secretory cytotoxic granule maturation and exocytosis require the effector protein hMunc13-4." Nat Immunol **8**(3): 257-67.
- Metkar, S. S., B. Wang, et al. (2003). "Granzyme B activates procaspase-3 which signals a mitochondrial amplification loop for maximal apoptosis." J Cell Biol **160**(6): 875-85.
- Morimoto, C., N. L. Letvin, et al. (1985). "The isolation and characterization of the human suppressor inducer T cell subset." J Immunol **134**(3): 1508-15.
- Moser, T. and E. Neher (1997). "Rapid exocytosis in single chromaffin cells recorded from mouse adrenal slices." Journal of Neuroscience **17**(7): 2314-2323.
- Nagy, G., I. Milosevic, et al. (2008). "The SNAP-25 linker as an adaptation toward fast exocytosis." Mol Biol Cell **19**(9): 3769-81.
- Negulescu, P. A., T. B. Krasieva, et al. (1996). "Polarity of T cell shape, motility, and sensitivity to antigen." Immunity **4**(5): 421-30.
- Niemeyer, B. A. and M. Hoth "Excitable T cells: Ca(v)1.4 channel contributions and controversies." Immunity **35**(3): 315-7.
- Nofal, S., U. Becherer, et al. (2007). "Primed vesicles can be distinguished from docked vesicles by analyzing their mobility." Journal of Neuroscience **27**(6): 1386-1395.
- Odake, S., C. M. Kam, et al. (1991). "Human and murine cytotoxic T lymphocyte serine proteases: subsite mapping with peptide thioester substrates and inhibition of enzyme activity and cytolysis by isocoumarins." Biochemistry **30**(8): 2217-27.
- Oheim, M. (2001). "Imaging transmitter release. I. Peeking at the steps preceding membrane fusion." Lasers Med Sci **16**(3): 149-58.
- Palade, G. (1975). "Intracellular Aspects of Process of Protein-Synthesis." Science **189**(4200): 347-358.
- Pasche, M., U. Matti, et al. "Docking of LDCVs is modulated by lower intracellular [Ca²⁺] than priming." PLoS One **7**(5): e36416.

Pattu, V., B. Qu, et al. (2011). "Syntaxin7 Is Required for Lytic Granule Release from Cytotoxic T Lymphocytes." Traffic **12**(7): 890-901.

Peters, P. J., J. Borst, et al. (1991). "Cytotoxic T lymphocyte granules are secretory lysosomes, containing both perforin and granzymes." J Exp Med **173**(5): 1099-109.

Plattner, H., A. R. Artalejo, et al. (1997). "Ultrastructural organization of bovine chromaffin cell cortex-analysis by cryofixation and morphometry of aspects pertinent to exocytosis." J Cell Biol **139**(7): 1709-17.

Pores-Fernando, A. T. and A. Zweifach (2009). "Calcium influx and signaling in cytotoxic T-lymphocyte lytic granule exocytosis." Immunol Rev **231**(1): 160-73.

Purbhoo, M. A. "The function of sub-synaptic vesicles during T-cell activation." Immunol Rev **251**(1): 36-48.

Qu, B., D. Al-Ansary, et al. "ORAI-mediated calcium influx in T cell proliferation, apoptosis and tolerance." Cell Calcium **50**(3): 261-9.

Qu, B., V. Pattu, et al. (2011). "Docking of Lytic Granules at the Immunological Synapse in Human CTL Requires Vti1b-Dependent Pairing with CD3 Endosomes." Journal of Immunology **186**(12): 6894-6904.

Quintana, A., M. Pasche, et al. (2011). "Calcium microdomains at the immunological synapse: how ORAI channels, mitochondria and calcium pumps generate local calcium signals for efficient T-cell activation." Embo Journal **30**(19): 3895-3912.

Rettig, J. and E. Neher (2002). "Emerging roles of presynaptic proteins in Ca⁺⁺-triggered exocytosis." Science **298**(5594): 781-5.

Robertson, M. E., R. A. Seamons, et al. (1999). "A selection system for functional internal ribosome entry site (IRES) elements: analysis of the requirement for a conserved GNRA tetraloop in the encephalomyocarditis virus IRES." Rna **5**(9): 1167-79.

Rohrbach, A. (2000). "Observing secretory granules with a multiangle evanescent wave microscope." Biophys J **78**(5): 2641-54.

Rust, M. J., M. Bates, et al. (2006). "Sub-diffraction-limit imaging by stochastic optical reconstruction microscopy (STORM)." Nat Methods **3**(10): 793-5.

Sabatini, B. L. and W. G. Regehr (1996). "Timing of neurotransmission at fast synapses in the mammalian brain." Nature **384**(6605): 170-172.

Schiavo, G., G. Stenbeck, et al. (1997). "Binding of the synaptic vesicle v-SNARE, synaptotagmin, to the plasma membrane t-SNARE, SNAP-25, can explain docked vesicles at neurotoxin-treated synapses." Proceedings of the National Academy of Sciences of the United States of America **94**(3): 997-1001.

Schulz, M., H. J. Schuurman, et al. (1995). "Acute rejection of vascular heart allografts by perforin-deficient mice." Eur J Immunol **25**(2): 474-80.

- Schwarz, E. C., C. Kummerow, et al. (2007). "Calcium dependence of T cell proliferation following focal stimulation." Eur J Immunol **37**(10): 2723-33.
- Schwarz, E. C., B. Qu, et al. "Calcium, cancer and killing: The role of calcium in killing cancer cells by cytotoxic T lymphocytes and natural killer cells." Biochim Biophys Acta **1833**(7): 1603-11.
- Shaner, N. C., P. A. Steinbach, et al. (2005). "A guide to choosing fluorescent proteins." Nat Methods **2**(12): 905-9.
- Shaw, P. J., B. Qu, et al. "Molecular regulation of CRAC channels and their role in lymphocyte function." Cell Mol Life Sci **70**(15): 2637-56.
- Shen, J., D. C. Tareste, et al. (2007). "Selective activation of cognate SNAREpins by Sec1/Munc18 proteins." Cell **128**(1): 183-95.
- Shi, L., R. P. Kraut, et al. (1992). "A natural killer cell granule protein that induces DNA fragmentation and apoptosis." J Exp Med **175**(2): 553-66.
- Shi, L., S. Mai, et al. (1997). "Granzyme B (GraB) autonomously crosses the cell membrane and perforin initiates apoptosis and GraB nuclear localization." J Exp Med **185**(5): 855-66.
- Shinkai, Y., K. Takio, et al. (1988). "Homology of perforin to the ninth component of complement (C9)." Nature **334**(6182): 525-7.
- Sorensen, J. B., K. Wiederhold, et al. (2006). "Sequential N- to C-terminal SNARE complex assembly drives priming and fusion of secretory vesicles." Embo J **25**(5): 955-66.
- Speidel, D., C. E. Bruederle, et al. (2005). "CAPS1 regulates catecholamine loading of large dense-core vesicles." Neuron **46**(1): 75-88.
- Stepp, S. E., R. Dufourcq-Lagelouse, et al. (1999). "Perforin gene defects in familial hemophagocytic lymphohistiocytosis." Science **286**(5446): 1957-9.
- Stevens, D. R., C. Schirra, et al. "Vesicle pools: lessons from adrenal chromaffin cells." Front Synaptic Neurosci **3**: 2.
- Stinchcombe, J. C., D. C. Barral, et al. (2001). "Rab27a is required for regulated secretion in cytotoxic T lymphocytes." J Cell Biol **152**(4): 825-34.
- Sudhof, T. C. (2012). "Calcium Control of Neurotransmitter Release." Cold Spring Harbor Perspectives in Biology **4**(1).
- Sudhof, T. C. and J. E. Rothman (2009). "Membrane fusion: grappling with SNARE and SM proteins." Science **323**(5913): 474-7.
- Sutton, R. B., D. Fasshauer, et al. (1998). "Crystal structure of a SNARE complex involved in synaptic exocytosis at 2.4 Å resolution." Nature **395**(6700): 347-53.
- Takayama, H. and M. V. Sitkovsky (1987). "Antigen receptor-regulated exocytosis in cytotoxic T lymphocytes." J Exp Med **166**(3): 725-43.

- Tatemoto, K. (1982). "Neuropeptide Y: complete amino acid sequence of the brain peptide." Proc Natl Acad Sci U S A **79**(18): 5485-9.
- Thiery, J., D. Keefe, et al. "Perforin pores in the endosomal membrane trigger the release of endocytosed granzyme B into the cytosol of target cells." Nat Immunol **12**(8): 770-7.
- Toonen, R. F., O. Kochubey, et al. (2006). "Dissecting docking and tethering of secretory vesicles at the target membrane." Embo J **25**(16): 3725-37.
- Topham, N. J. and E. W. Hewitt (2009). "Natural killer cell cytotoxicity: how do they pull the trigger?" Immunology **128**(1): 7-15.
- Torri-Tarelli, F., F. Grohovaz, et al. (1985). "Temporal coincidence between synaptic vesicle fusion and quantal secretion of acetylcholine." J Cell Biol **101**(4): 1386-99.
- Trenn, G., H. Takayama, et al. (1987). "Exocytosis of cytolytic granules may not be required for target cell lysis by cytotoxic T-lymphocytes." Nature **330**(6143): 72-4.
- Trotta, R., K. A. Puorro, et al. (1998). "Dependence of both spontaneous and antibody-dependent, granule exocytosis-mediated NK cell cytotoxicity on extracellular signal-regulated kinases." J Immunol **161**(12): 6648-56.
- Voets, T. (2000). "Dissection of three Ca²⁺-dependent steps leading to secretion in chromaffin cells from mouse adrenal slices." Neuron **28**(2): 537-45.
- Voets, T., E. Neher, et al. (1999). "Mechanisms underlying phasic and sustained secretion in chromaffin cells from mouse adrenal slices." Neuron **23**(3): 607-15.
- Voskoboinik, I., M. C. Thia, et al. (2005). "Calcium-dependent plasma membrane binding and cell lysis by perforin are mediated through its C2 domain: A critical role for aspartate residues 429, 435, 483, and 485 but not 491." J Biol Chem **280**(9): 8426-34.
- Walter, A. M., K. Wiederhold, et al. "Synaptobrevin N-terminally bound to syntaxin-SNAP-25 defines the primed vesicle state in regulated exocytosis." J Cell Biol **188**(3): 401-13.
- Weber, J. P., K. Reim, et al. "Opposing functions of two sub-domains of the SNARE-complex in neurotransmission." Embo J **29**(15): 2477-90.
- Whitley, P., E. Grahn, et al. (1996). "A 12-residue-long polyleucine tail is sufficient to anchor synaptobrevin to the endoplasmic reticulum membrane." J Biol Chem **271**(13): 7583-6.
- Wiederhold, K., T. H. Kloepper, et al. "A coiled coil trigger site is essential for rapid binding of synaptobrevin to the SNARE acceptor complex." J Biol Chem **285**(28): 21549-59.
- Williams, N. S. and V. H. Engelhard (1996). "Identification of a population of CD4+ CTL that utilizes a perforin- rather than a Fas ligand-dependent cytotoxic mechanism." J Immunol **156**(1): 153-9.

- Winkler, H. (1993). "The adrenal chromaffin granule: a model for large dense core vesicles of endocrine and nervous tissue." J Anat **183 (Pt 2)**: 237-52.
- Wu, M. M., J. Buchanan, et al. (2006). "Ca²⁺ store depletion causes STIM1 to accumulate in ER regions closely associated with the plasma membrane." J Cell Biol **174(6)**: 803-13.
- Wurth, G. A. and A. Zweifach (2002). "Evidence that cytosolic calcium increases are not sufficient to stimulate phospholipid scrambling in human T-lymphocytes." Biochem J **362(Pt 3)**: 701-8.
- Yassine, W., N. Taib, et al. (2009). "Reversible transition between alpha-helix and beta-sheet conformation of a transmembrane domain." Biochim Biophys Acta **1788(9)**: 1722-30.
- Yasukawa, M., H. Ohminami, et al. (1999). "Fas-independent cytotoxicity mediated by human CD4⁺ CTL directed against herpes simplex virus-infected cells." J Immunol **162(10)**: 6100-6.
- Yizhar, O. and U. Ashery (2008). "Modulating vesicle priming reveals that vesicle immobilization is necessary but not sufficient for fusion-competence." PLoS One **3(7)**: e2694.
- Young, J. D., Z. A. Cohn, et al. (1986). "The ninth component of complement and the pore-forming protein (perforin 1) from cytotoxic T cells: structural, immunological, and functional similarities." Science **233(4760)**: 184-90.
- Zhang, S. L., Y. Yu, et al. (2005). "STIM1 is a Ca²⁺ sensor that activates CRAC channels and migrates from the Ca²⁺ store to the plasma membrane." Nature **437(7060)**: 902-5.

Curriculum Vitae

Personal Information

Name: Min Ming
Date of birth: 20th May 1984
Place of birth: Wuhan
Nationality: China
Email: MinMING-UKS@gmx.de

Education

2010-present

Ph.D candidate

in Saarland University, Homburg/Saar, Germany
Supervisor: Prof. Dr. Jens Rettig

2007-2009

Master degree

in Biophysics from the Institute of Biophysics and
Biochemistry, Huazhong University of Science and
Technology (**HUST**), Wuhan, P. R. China
Supervisor: Prof. Dr. Wu Zheng-Xing

2007-2003

Bachelor degree

in Biomedical Engineering from **HUST**, Wuhan, P. R.
China